Electronic properties of two-dimensional Dirac fermions in superlattice structures

Inaugural-Dissertation

zur Erlangung des Doktorgrades der
Mathematisch-Naturwissenschaftlichen Fakultät der
Heinrich-Heine-Universität Düsseldorf

vorgelegt von:

Lukas Handt

aus Bückeburg

Düsseldorf, März 2024

aus dem Institut für Theoretische Physik, Lehrstuhl IV der
Heinrich-Heine-Universität Düsseldorf

Gedruckt mit der Genehmigung der
Mathematisch-Naturwissenschaftlichen Fakultät der
Heinrich-Heine-Universität Düsseldorf

Berichterstatter:

1. Prof. Dr. Reinhold Egger

2. PD Dr. Hermann Kampermann

Tag der mündlichen Prüfung: 13.05.2024

Abstract

Solid state physics has made striking progress in the recent decades. This led to a great interest for experimental physicists and theoreticians in research of different applications and materials.
Within this work, different superlattice structures are presented and the influence of two-dimensional Dirac fermions on electronic properties is discussed.
We introduce the model of twisted bilayer graphene, which includes the moiré superlattice, flat bands and magic angles. The moiré superlattice causes completely flat bands for discrete rotation angles between the two graphene layers. These angles are called magic angles. Graphene is a widely studied material and the group around Y. Cao actually managed to observe some superlattice effects experimentally in 2019, which was an important breakthrough. Here we show that the magic angles can be shifted by tuning the ratio of nearest neighbor coupling and next-nearest neighbor coupling. Such angles where the bandstructure is flat are sensitive to a variation of the different coupling strengths.
Next, we discuss the influence of two-dimensional Dirac fermions in a mass superlattice. This mass superlattice periodically alternates between positive and negative values along one direction and can be realized for monolayer graphene. We show that the low-energy calculation is controlled by the Jackiw-Rebbi mechanism. With help of the transfer matrix approach, we obtain exact results for a piece-wise constant mass superlattice. Apart from the resulting anisotropic Dirac cone dispersion, we find different nontrivial boundary modes as well as interface modes near potential steps. We compute the dispersion relation for existing types of boundary and interface modes. We show that the interface modes, the Bloch wave functions, the transmission and the electrical conductance exhibit an explicit dependency on the step position relative to the superlattice.

Zusammenfassung

Die Festkörperphysik hat in den letzten Jahrzehnten beeindruckende Fortschritte gemacht. Dies führte zu großem Interesse bei experimentellen Physikern und Theoretikern in der Forschung an unterschiedlichen Anwendungen und Materialien.
In dieser Arbeit werden verschiedene Übergitter-Strukturen vorgestellt und der Einfluss zweidimensionaler Dirac-Fermionen auf die elektronischen Eigenschaften diskutiert.
Wir führen das Modell des verdrehten zweilagigen Graphens ein, welches auch das Moiré-Übergitter, flache Bänder und magische Winkel umfasst. Für diskrete Rotationswinkel zwischen den beiden Graphenschichten führt das Moiré-Übergitter zu vollständig flachen Bändern. Diese Rotationswinkel werden magische Winkel (engl.: magic angles) genannt. Graphen ist ein viel untersuchtes Material, und die Gruppe um Y. Cao hat tatsächlich 2019 einige Übergitter-Effekte experimentell beobachten können. Dies stellte einen wichtigen Durchbruch dar. Hier zeigen wir, dass die magischen Winkel durch Einstellen des Verhältnisses von nächsten Nachbar- und übernächsten Nachbarkopplungen verschoben werden können. Die Winkel, bei denen die Bandstruktur abflacht, reagieren empfindlich auf eine Variation der verschiedenen Kopplungsstärken.
Als nächstes diskutieren wir den Einfluss zweidimensionaler Dirac-Fermionen in einem Übergitter, dass durch einen effektiven Masseterm definiert wird, der periodisch zwischen positiven und negativen Werten entlang einer konstanten Richtung wechselt und für monolagiges Graphen realisiert werden kann. Wir zeigen, dass das Regime niedriger Energien durch den Jackiw-Rebbi-Mechanismus kontrolliert wird. Mit Hilfe des Ansatzes für Übertragungsmatrizen erhalten wir genaue Ergebnisse für ein stückweise konstante Massenübergitter. Neben der resultierenden anisotropen, kegelförmigen Dispersionsrelation finden wir auch verschiedene nichttriviale Moden in der Nähe von Potenzialschritten sowie den Ränder des Systems. Wir berechnen die Dispersionsrelation für die vorhandene Arten von Grenzmoden. Wir zeigen, dass die Moden nahe eines Potentialschrittes, die Bloch-Wellenfunktionen, die Transmission und die elektrische Leitfähigkeit eine explizite Abhängigkeit von der Position des Potentialschrittes relativ zur Überstruktur aufweisen.

Contents

Chapter 1

Introduction

In this work we are going to discuss various electronic properties of two-dimensional Dirac fermions in superlattice structures. To this end we will mainly focus on two different superlattices. In the last decades major progress in solid state physics dealing with superlattice structures was achieved and the topic became more and more interesting for theoreticans and also experimental physicists. Interestingly superlattices can cause properties that were not present before in the underlying sublattice structures. These effects do not only restrict to materials like graphene, they also can be seen generally in layered van der Waals materials [1] and topological insulators [2]. Furthermore, it is well known how to tune band structures in solid state physics with the help of superlattice potentials.
First, we are going to introduce some important fundamental principles and methods for later calculations. We start with a short overview of 2D materials. Furthermore, we explain the basic concepts of the tight binding method as well as the Kronig-Penney model and the Landauer-Büttiker formula. We also introduce the topic of Dirac fermions and basic properties of such particles will be declared for the graphene case. Graphene is a material formed by a single layer of graphite and exhibits exceptional properties. In 1947 P.R. Wallace calculated the band structure of graphite for the first time [3]. In general, there was a huge interest in the two-dimensional material graphene, especially by theoreticians. However, L.D. Landau and R. Peierls predicted in the 1930s that a two-dimensional crystal cannot be stable. This insight was based on thermal fluctuations with a divergent contribution for lower dimensional systems. Such a displacement caused by the fluctuations give rise to interatomic distances and forces a change of state [4, 5]. Nevertheless, the group headed by K.S. Novoselov and A.K. Geim showed in the mid 2000s with their work that they were able to find strictly two-dimensional free-standing atomic crystals and exfoliated monolayer graphene from a graphite block [6, 7]. For their work they were awarded with the Noble Prize in 2010 [8]. Their work marks the starting point for a variety of theoretical and experi-

mental groups dealing with graphene structures. The interest is also motivated by the low-energy limit of graphene. In the low-energy regime graphene can be described by a Dirac Hamiltonian. Therefore, the behavior can be linked to two-dimensional massless Dirac fermions that obey the Dirac equation.
In chapter 3 we consider the single-electron theory for a perfect twisted bilayer graphene structure with twist angle between both layers and without disorder effects. Here, the low-energy continuum theory developed by R. Bistritzer and A.H. MacDonald [9] holds for $\theta \lesssim 10°$. Otherwise, the restriction to a single valley per layer would not be allowed. For more details of continuum calculations see also references [10–14]. Here, we successively build up the system starting with decoupled layers in section 3.1. The continuum theory is valid for incommensurate and commensurate bilayers, which allows to employ Bloch theory in a quasiperiodic system without true crystal periodicity. In section 3.2 we introduce tunneling between the two decoupled layers which causes a moiré superlattice, see section 3.3. Such superlattice effects can be monitored. Flat bands locked to zero energy can be found near certain so-called magic angles like illustrated in section 3.6. Furthermore, we show limitations of the model in 3.5 and finally we are able to show how the nearest neighbor coupling and next-nearest neighbor coupling influence the magic angles. Especially, we show in section 3.7 that the magic angles will not be robust for a variation of the coupling ratio.
A big breakthrough in experiments was the work of Y. Cao *et al.* [15]. They were able to detect some of the exceptional properties such as the superconductivity of bilayer graphene systems for the first time.
The structure we will focus on in chapter 4 is a one-dimensional mass superlattice. A detailed discussion of the electronic spectrum of periodic mass problems was also done before in references [16] and [17]. In their case, regions of zero and positive mass alternate. The key point in the study shown in chapter 4 is the more general periodic mass superlattice. Here, we use a one-dimensional mass superlattice $M(x)$, which periodically alternates between positive and negative mass. For graphene this could be realised due to a sublattice dependent potential. These potentials can arise due to substrates like hexagonal boron nitride (hBN).
The model is introduced in section 4.1, where we also review in detail the electronic spectrum for a single mass kink and for a mass barrier. Like studied before, a single mass kink binds a Jackiw-Rebbi zero mode [18]. For the case of a periodic mass a gapless anisotropic Dirac cone exists, see section 4.2. In the presence of boundaries the periodicity condition allows imaginary and real solutions, leading to evanescent solutions and two different boundary modes that will be discussed in 4.3. Including a potential step, which characterizes an *np*-junction, also gives rise to quite similar two interface modes, see chapter 4.6. Interestingly these modes only appear in presence of the mass superlattice $M(x)$ and emerge near the center of the superlattice Brillouin zone while the other come from the Brillouin zone boundary. In section 4.7 we show

how to recover the low-energy spectrum of the periodic mass problem by projecting the Hamiltonian on the subspace of the chiral zero-energy modes localized at isolated kinks and anti-kinks of the mass potential.

Chapter 2

Background material

In this chapter we introduce some fundamental aspects and principles that will be necessary to understand the route and calculations in the following chapters. For this we briefly define 2D materials. The calculations in chapter 3 and 4 are based on this class of materials. Furthermore we introduce some models and formalisms such as the Landauer-Büttiker formula used in section 4.6.2.

2.1 2D materials

Two-dimensional materials can be characterized by crystalline structures with a thickness of just one or at most a few layers. They differ enormously from their three-dimensional counterparts and exhibit unusual properties. Since the discovery of the characteristics of e.g. graphene, there is a huge interest in these materials and the 2D family started growing quite fast.
The main feature, that makes 2D materials compelling for application, is the possibility to stack various monolayers onto each other such that one can design a special material for a specific purpose. In fact, there seems to be no limit for the stacking. As an illustrative point of view, shown in Figure 2.1, every material can be interpreted as Lego block, such that a high variety of layered systems can be designed. [19]
There are only two main interacting forces in layered systems. The strong covalent bond provides the in-plane stability and the van der Waals force, which prohibits mixing of the layers. These types of heterostructures open up a wide interest for technological use such as application in transistors, solar systems and a lot more gadgets.
Graphene, hexagonal boron nitride (hBN) as well as molybdenum disulfid (MoS_2) are the most studied structures. In this work, the focus is set on graphene structures and the description of similar structures. The role of hBN in laboratories is essential. Due to its band gap it is often used to protect other 2D materials from the environment [19, 20].

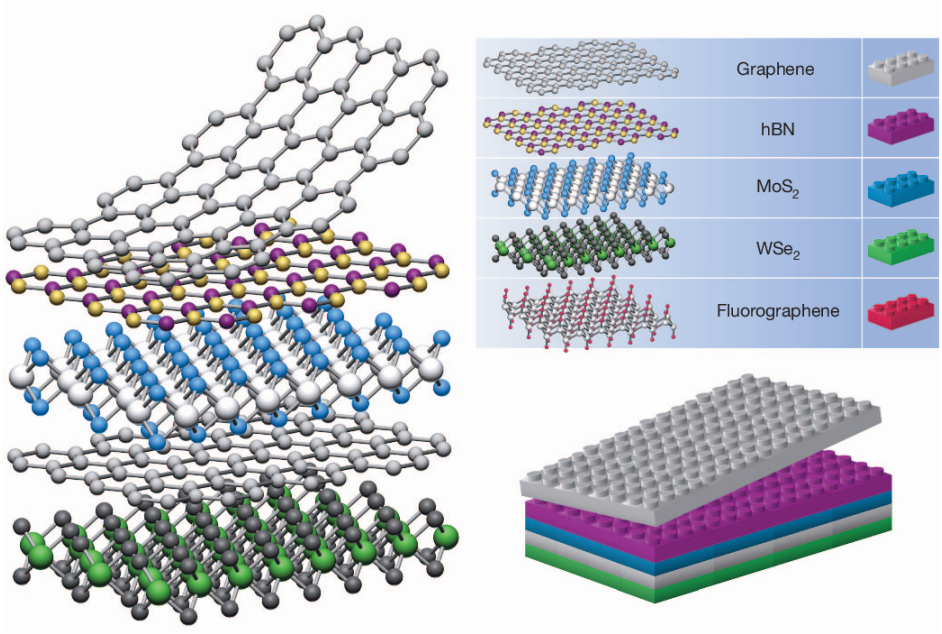

Figure 2.1: Illustration of Lego principle. Figure from [19].

2.2 Tight Binding Method

The tight binding approach is a useful method to deal with electronic structures of materials in condensed matter physics. One of the key points is to provide a description of the band structure by calculating the interaction forces between the crystalline layers, such that it is a convenient method for solids.
The concept is based on the assumption that a crystal lattice is typically composed of a periodic arrangement of atoms in space. To describe the electronic properties of a crystal, one can use wave functions $\psi_i(\mathbf{r})$ where i represents the site of an atom, and $\mathbf{r}$ is the position vector in the crystal. Each wave function $\psi_i(\mathbf{r})$ characterizes the electronic state associated with an atom at site i. The total wave function for the entire crystal can be expressed as a linear combination of these localized wave functions:

$$\Psi(\mathbf{r}) = \sum_i c_i \psi_i(\mathbf{r}), \tag{2.1}$$

where c_i is the coefficient determining the contribution of each atomic site to the overall electronic state. The tight binding Hamiltonian then describes the energy of the electrons in the crystal. The operator is written as

$$H = \sum_i \varepsilon_i c_i^\dagger c_i - \sum_{\langle i,j \rangle} t_{ij} \left(c_i^\dagger c_j + c_j^\dagger c_i \right). \tag{2.2}$$

Here $c_i^\dagger$ and c_i are creation and annihilation operators for an electron at site i and t_{ij} is the parametrization of hopping between sites i and j [21]. This hopping integral gives

rise to the probability amplitude of an electron to move from site i to site j and ε_i represents the on-site energy of an electron at site i.
By diagonalizing the matrix representation of (2.2) one can find information about energy eigenvalues and eigenvectors. With the help of these quantities one can discuss energy levels and energy bands to understand conductivity and other material parameters. [22–24]

2.3 Kronig-Penney model

The Kronig-Penney model is a theoretical framework in solid-state physics providing valuable insights into the electronic band structure of periodic crystal lattices. Originally formulated as a simple one-dimensional model [25], it has evolved over the years to encompass a broad spectrum of potential energy landscapes in periodic crystal lattices. Eldib, Hassan and Mohamed introduced a comprehensive extension of this model. Their formulation [26] includes complex periodic potentials.

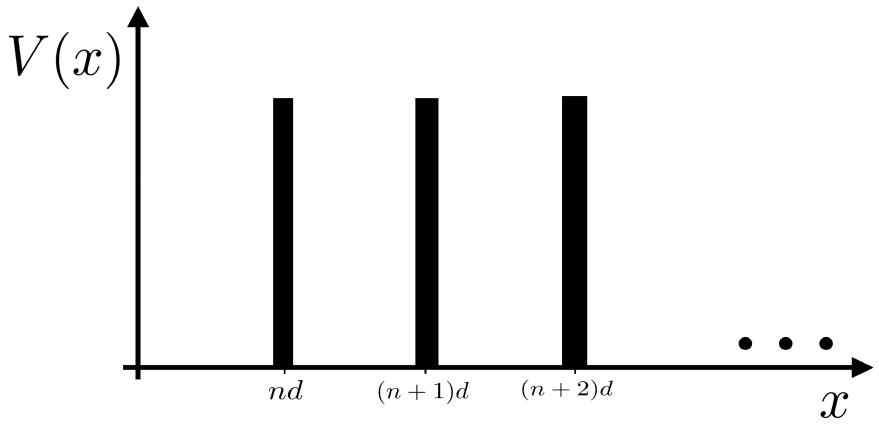

Figure 2.2: Scheme of Kronig-Penney potential.

The basic Kronig-Penney model considers a one-dimensional periodic potential consisting of a series of delta-function barriers. In this simplified model, the crystal lattice is represented as a string of delta-function potentials of the same spacial extent. The model can be represented via the Schrödinger equation and then written as

$$\left(-\frac{\hbar^2}{2m}\frac{d^2}{dx^2} + V(x)\right)\psi(x) = E\psi(x), \tag{2.3}$$

where the periodic potential $V(x)$, see Figure 2.2, can be described as a sum of delta functions

$$V(x) = \sum_n V_0\delta(x - nd). \tag{2.4}$$

2.4 Dirac fermions

Fermions, in general, are fundamental particles that form the building blocks of matter. They possess unique characteristics that distinguish them from other particles, such as bosons.
Key properties of fermions include their half-integer spin, which leads to the Pauli exclusion principle. Due to this it is impossible for two identical fermions to occupy the same quantum state simultaneously [27, 28].
Dirac fermions, a remarkable class of particles, play an important role in condensed matter physics. Initially introduced by Paul Dirac in the context of relativistic quantum mechanics [29], these particles exhibit a wide spectrum of relativistic and quantum behavior. Dirac fermions have gained substantial attention due to their unique properties and their relevance in various condensed matter systems, including graphene [6], topological insulators [30], and Weyl semimetals [31]. Based on Paul Diracs work the Dirac equation describes the behavior of spin-$\frac{1}{2}$ particles, such as electrons, in a relativistic framework. It is given by

$$(i\gamma^\mu \partial_\mu - m)\psi = 0, \tag{2.5}$$

where ∂_μ is the four-gradient, m is the mass of the particle, and ψ is the Dirac spinor. γ^μ are the Dirac matrices which can be defined as

$$\gamma^0 = \begin{pmatrix} \mathbb{1} & 0 \\ 0 & \mathbb{1} \end{pmatrix}, \quad \gamma^k = \begin{pmatrix} 0 & \sigma^k \\ -\sigma^k & 0 \end{pmatrix} \tag{2.6}$$

with the Pauli matrices σ^k for k = 1,2,3. For $i \neq j$, the Dirac matrices anticommute with each other $\{\gamma^i, \gamma^j\} = 0$ while γ^0 is Hermitian and γ^k are anti-Hermitian. Dirac fermions exhibit several distinctive characteristics that distinguish them from other particles in condensed matter systems:

- **Relativistic-like dispersion:** The energy-momentum relation of Dirac fermions near the Fermi level is linear, resembling the characteristics of relativistic particles [32].
- **Massless nature:** In some materials, Dirac fermions are effectively massless, which leads to exceptional electronic transport properties. This property is evident in graphene, where the Dirac fermions behave as if they have no rest mass [6, 7].
- **Chiral behavior:** Dirac fermions exhibit chiral behavior, with their spin and momentum locked in a specific way. This chirality gives rise to phenomena like the unconventional quantum Hall effect [6, 7].

- **Topological Protection:** In topological insulators, Dirac Fermions are topologically protected, making them robust against certain types of disorder and defects [30].

For the understanding of the above characteristics we will now consider a monolayer graphene structure and take a closer look at.

2.5 Graphene

Graphene monolayers are formed by carbon atoms, which are arranged in hexagonal structures. It turns out that the honeycomb lattice can be described as a combination of two triangular sublattices with diatomic basis A and B. The lattice vectors are

$$\mathbf{a}_1 = \frac{a}{2}\left(3,\sqrt{3}\right), \quad \mathbf{a}_2 = \frac{a}{2}\left(3,-\sqrt{3}\right) \tag{2.7}$$

where $a \approx 1.42\mathring{A}$ is the lattice constant.

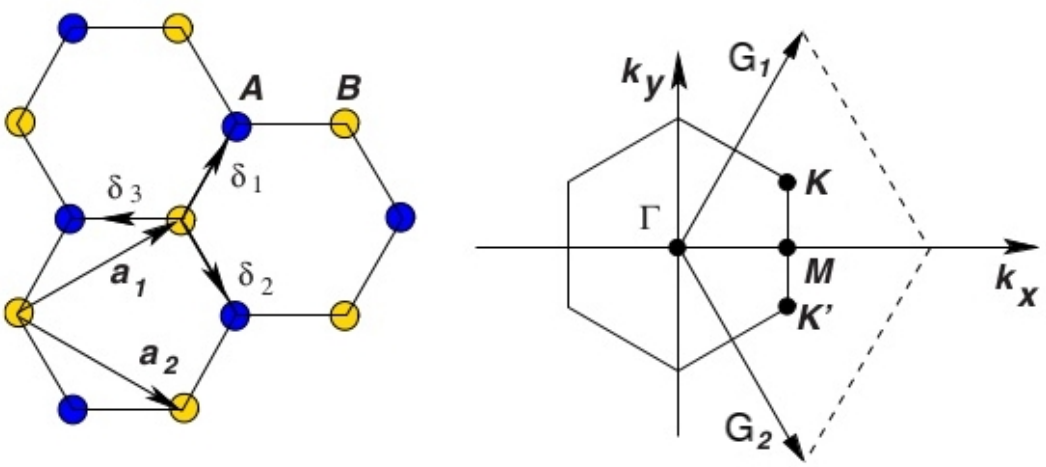

Figure 2.3: Graphene lattice. Adapted from [32].
left: Honeycomb lattice with color coded diatomic basis A and B, unit vectors a_i for $i = 1,2$ and nearest neighbor vectors $\boldsymbol{\delta}_1 = \frac{a}{2}\left(1,\sqrt{3}\right), \boldsymbol{\delta}_2 = \frac{a}{2}\left(1,-\sqrt{3}\right), \boldsymbol{\delta}_3 = -\frac{a}{2}\left(1,0\right)$.
right: Position of the Dirac points K and K' in the reciprocal lattice.

In real space one can define the nearest neighbor vectors of graphene monolayers as

$$\boldsymbol{\delta}_1 = \frac{a}{2}\left(1,\sqrt{3}\right), \quad \boldsymbol{\delta}_2 = \frac{a}{2}\left(1,-\sqrt{3}\right), \quad \boldsymbol{\delta}_3 = -\frac{a}{2}\left(1,0\right). \tag{2.8}$$

Moreover, the Wigner-Seitz cell of the reciprocal lattice is spanned by the vectors $\mathbf{G}_i = 2\pi \cdot \frac{\mathbf{a}_j \times (\mathbf{a}_i \times \mathbf{a}_j)}{|\mathbf{a}_i \times \mathbf{a}_j|^2}$ which then explicitly results in

$$\mathbf{G}_1 = \frac{2\pi}{3a}\left(1,\sqrt{3}\right), \quad \mathbf{G}_2 = \frac{2\pi}{3a}\left(1,-\sqrt{3}\right). \tag{2.9}$$

There are some further points which are of interest due to their symmetry like the center of the Brillouin zone $\Gamma = (0,0)^T$ and the M-point

$$\mathbf{M} = \left(\frac{2\pi}{3a}, 0\right). \tag{2.10}$$

The corners of the Brillouin zone, known as Dirac points or K points, are located at

$$\mathbf{K} = \left(\frac{2\pi}{3a}, \frac{2\pi}{3\sqrt{3}a}\right), \quad \mathbf{K}' = \left(\frac{2\pi}{3a}, -\frac{2\pi}{3\sqrt{3}a}\right). \tag{2.11}$$

Near these Dirac points the conductance and valence band of the π-electrons touch each other and the electrons can tunnel to their neighbors.
In 1998 R. Saito et. al. introduced in *Transport Properties of Carbon Nanotubes* [33] the tight binding model for graphene structures in terms of the Hamiltonian

$$H = -t \sum_{\langle i,j\rangle,s} \left(a^\dagger_{i,s} b_{s,j} + h.c.\right) - t' \sum_{\langle\langle i,j\rangle\rangle,s} \left(a^\dagger_{s,i} a_{s,j} + b^\dagger_{s,i} b_{s,j} + h.c.\right), \tag{2.12}$$

where the first term defines the nearest neighbor hopping. Next-nearest neighbor couplings are denoted by the second term. $a^\dagger_{s,i}$, $b^\dagger_{s,i}$ denote creation- and $a_{s,i}$, $b_{s,i}$ annihilation operator for electrons with spin $s =\uparrow$ and $s =\downarrow$. The nearest neighbor hopping can also be seen as a switch of the sublattice while an electron stays on the same sublattice during the next-nearest neighbor hopping. Interestingly, the energy 2.5 eV $\leq t \leq$ 3 eV for jumping to the nearest neighbor is much higher than t' with $0.02t \leq t' \leq 0.2t$.
Starting with Hamiltonian (2.12) one can find the dispersion relation of graphene by applying the tight binding approximation. The next-nearest neighbor coupling physically gives just an energy shift and such one can focus only on the first term of equation (2.12). The wave vector can be expressed in terms of the reciprocal lattice vectors G_i, see (2.9):

$$\mathbf{k} = b_1\mathbf{G}_1 + b_2\mathbf{G}_2 = \frac{a}{2\pi}\left(k_1\mathbf{G}_1 + k_2\mathbf{G}_2\right) \tag{2.13}$$

with $0 \leq b_i \leq 1$, $k_i \propto \frac{2\pi}{a} b_i$ and $b_i = \frac{n_i}{N_i}$. Here N is related to the size of the graphene sheet via $L_i = N_i a$ and $k_i \cdot L_i = 2\pi n_i$. The creation operators can be rewritten in the Fourier representation like:

$$a^\dagger_{i,s} = \frac{1}{\sqrt{N}} \sum_{\mathbf{k}} e^{-\mathbf{k}\cdot\mathbf{r}} a^\dagger_{\mathbf{k},i,s} = \frac{1}{\sqrt{N}} \sum_{k_1,k_2} \exp\left(-i\frac{a}{2\pi}\left(k_1\mathbf{G}_1 + k_2\mathbf{G}_2\right)\cdot\mathbf{r}\right) a^\dagger_{\mathbf{k},i,s}, \tag{2.14}$$

$$b^\dagger_{i,s} = \frac{1}{\sqrt{N}} \sum_{\mathbf{k}} e^{-\mathbf{k}\cdot\mathbf{r}} b^\dagger_{\mathbf{k},i,s} = \frac{1}{\sqrt{N}} \sum_{k_1,k_2} \exp\left(-i\frac{a}{2\pi}\left(k_1\mathbf{G}_1 + k_2\mathbf{G}_2\right)\cdot\mathbf{r}\right) b^\dagger_{\mathbf{k},i,s}. \tag{2.15}$$

This follows analogously for the annihilation operators and such the first term of Hamiltonian (2.9) can be written:

$$\begin{aligned}\gamma &= t\sum_{\langle i,j\rangle}\left(a_i^\dagger b_j + h.c.\right)\\ &= t\sum_{\mathbf{k}}\left[\left(e^{i\mathbf{k}\cdot\boldsymbol{\delta}_1}+e^{i\mathbf{k}\cdot\boldsymbol{\delta}_2}+e^{i\mathbf{k}\cdot\boldsymbol{\delta}_3}\right)a_{\mathbf{k}}^\dagger b_{\mathbf{k}} + \left(e^{i\mathbf{k}\cdot\boldsymbol{\delta}_1}+e^{i\mathbf{k}\cdot\boldsymbol{\delta}_2}+e^{i\mathbf{k}\cdot\boldsymbol{\delta}_3}\right)b_{\mathbf{k}}^\dagger a_{\mathbf{k}}\right].\end{aligned} \tag{2.16}$$

Here, the spin is kept implicit and the sum runs over every $\mathbf{k}$ in the first Brillouin zone. The vectors are defined as shown in Figure 2.3.
The second term of (2.12) represents the diagonal elements of the Hamiltonian and introduce the shift, that has been mentioned before. One can call this shift ϵ_0 with

$$\epsilon_0 = -2t'\sum_{l=1}^{3} e^{i\mathbf{k}\cdot\boldsymbol{\delta}_l}. \tag{2.17}$$

Finally, the Hamiltonian has the form

$$H = \sum_{\mathbf{k}}\begin{pmatrix}a_{\mathbf{k}}^\dagger & b_{\mathbf{k}}^\dagger\end{pmatrix}\begin{pmatrix}\epsilon_0 & \gamma\\ \gamma & \epsilon_0\end{pmatrix}\begin{pmatrix}a_{\mathbf{k}}\\ b_{\mathbf{k}}\end{pmatrix} \tag{2.18}$$

and due to its diagonalisation one finds the dispersion relation

$$\epsilon(\mathbf{k}) = \pm t\sqrt{3-F(\mathbf{k})} - t'F(\mathbf{k}) \tag{2.19}$$

with

$$F(\mathbf{k}) = 2\cos\left(\sqrt{3}k_y a\right) + 4\cos\left(\frac{\sqrt{3}}{2}k_y a\right)\cos\left(\frac{3}{2}k_x a\right). \tag{2.20}$$

Due to the π-band symmetry the valence band is fully occupied while the conduction band is empty. This is the reason for describing graphene as semiconductor with zero energy gap and one can expand (2.19) near the Dirac points for the wave vector $\mathbf{k} = \mathbf{K} + \mathbf{q}$.
Expanding near the Dirac points yields

$$\epsilon(\mathbf{q}) \approx 3t' \pm v_F|\mathbf{q}| - \left(\frac{9}{4}t' \pm \frac{3}{8}t\sin(3\theta)\right)|\mathbf{q}|^2 a^2 \tag{2.21}$$

with Fermi velocity

$$v_F = \frac{3}{2}ta \approx 10^6\ \frac{m}{s} \text{ for } t \approx 3\ eV \tag{2.22}$$

and angle $\theta = \arctan\left(\frac{q_y}{q_x}\right)$. For a small region around the Dirac points the expanded dispersion relation (2.21) is compatible to ultra-relativistic particles of the Dirac equation. Recalling section 2.4 this justifies the description of electrons near the K points as massless Dirac fermions

$$-iv_F\boldsymbol{\sigma}\cdot\nabla\Psi = E\Psi. \tag{2.23}$$

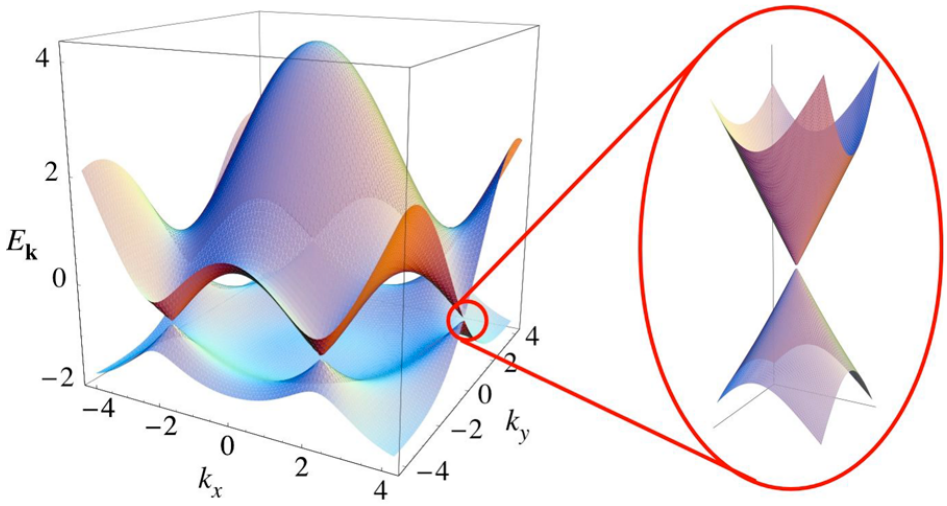

Figure 2.4: Dispersion relation of graphene monolayers. Figure from [32]. *left:* Energy dispersion (2.19) with honeycomb structure of Brillouin zone. *right:* Zoom to the Dirac points.

One can write the Dirac-like Hamiltonian as

$$H_D^K = v_F \begin{pmatrix} 0 & k_x + ik_y \\ k_x - ik_y & 0 \end{pmatrix} = v_F \boldsymbol{\sigma} \cdot \mathbf{k}. \tag{2.24}$$

Here $\boldsymbol{\sigma} = (\sigma_x, \sigma_y)$ is a two-dimensional Pauli vector which ensures that states can be written as two-component wave functions

$$\Psi_{\pm,\mathbf{K}}(\mathbf{q}) = \frac{1}{\sqrt{2}} \begin{pmatrix} \exp(-i\theta_{\mathbf{q}}/2) \\ \pm \exp(i\theta_{\mathbf{q}}/2) \end{pmatrix}. \tag{2.25}$$

$H_D^{K'} = -v_F \boldsymbol{\sigma}^* \cdot \mathbf{k}$ holds for the K' points with $\mathbf{k} = \mathbf{K}' + \mathbf{q}$ analogously.

2.6 Landauer-Büttiker formula

The Landauer-Büttiker formula provides a fundamental framework for understanding electron transport in low-dimensional systems. The work of Rolf Landauer in 1957 [34] can be seen as the origin of the Landauer-Büttiker formula

$$G = \frac{2e^2}{h} \mathcal{T}, \tag{2.26}$$

where G is the electrical conductance, e is the elementary charge, h is Planck's constant, and $\mathcal{T}$ is the transmission probability. Landauer's paper set a basis for understanding the relationship between electrical conductance and the transmission of electrons through a system. His approach treated the transport of electrons as a statistical process, influenced by the principles of thermodynamics and information theory.

In the late 1980s, Markus Büttiker expanded Landauer's work. Büttikers work is a significant extension of Landauer's original concept [35] and gives rise to the Landauer-Büttiker formula. The Landauer-Büttiker formula is particularly relevant in the field of quantum transport, addressing the behavior of electrons as both particles and waves. One of the remarkable predictions of the formula is the quantization of conductance in quantum point contacts and quantum wires. This phenomenon reveals the discrete nature of electron transport and has been experimentally verified in various systems [36].

Chapter 3

Twisted Bilayer Graphene

Twisted bilayer graphene is a two-dimensional material formed by two superimposed graphene monolayers with a relative twist θ between them. This twist results in a superlattice, the so called moiré pattern, which gives rise to unique electronic properties. The study of twisted bilayer graphene has gained significant attention in recent years due to its physical phenomena, e.g., superconductivity and flat bands as discussed in the following. Twisted bilayer graphene was first introduced by P. R. Wallace in 1947 [3] and was extensively explored. In 2018, Pablo Jarillo-Herrero's group at MIT published a paper [15] that revealed some of these properties in experimental results, such as the existence of superconductivity as a function of the twist angle.

In this chapter we successively build up a system of twisted bilayer graphene and show that the moiré pattern causes superlattice effects such as the flattening of bands near the magic angles. Interestingly, we were able to show how the magic angles depend on the coupling strength κ. Hence, the angle for which the energy bands flatten changes due to variation of the ratio of the coupling to nearest neighbors and the coupling to next-nearest neighbors.

3.1 Decoupled layers

Here first the case of decoupled layers is considered. For that one can neglect inter-layer tunneling in the geometry. Starting from the Bernal stacked bilayer, one rotates the first honeycomb layer clockwise by $\theta_1 = \theta/2$ and translates the second layer by a vector $\mathbf{v}_0$, followed by a rotation of the second layer with angle $\theta_2 = -\theta/2$ around the origin. The layers are separated by $d_\perp \hat{e}_z$. Then, the lattice translation operators in each layer with respect to a fixed frame are given by [14]

$$\mathbf{a}_{\ell,j} \equiv \mathbf{O}(\theta_\ell) \cdot \mathbf{a}_j, \quad \mathbf{a}_1 = a \begin{pmatrix} \frac{1}{2} \\ \frac{\sqrt{3}}{2} \end{pmatrix}, \quad \mathbf{a}_2 = a \begin{pmatrix} -\frac{1}{2} \\ \frac{\sqrt{3}}{2} \end{pmatrix}, \tag{3.1}$$

$$\mathbf{R}_{\ell=1,2} = n_1 \mathbf{a}_{\ell,1} + n_2 \mathbf{a}_{\ell,2}, \quad \mathbf{O}(\theta_\ell) = \begin{pmatrix} \cos\theta_\ell & \sin\theta_\ell \\ -\sin\theta_\ell & \cos\theta_\ell \end{pmatrix}, \tag{3.2}$$

with integers $n_{1,2}$ and $a = \sqrt{3}d$, see section 2.5. One finds the unit cell area $A_{uc} = |\mathbf{a}_1 \times \mathbf{a}_2| = \sqrt{3}a^2/2$. The basis is formed by two carbon atoms ($\alpha = A,B$) located at the positions $\mathbf{R}_\ell + \mathbf{v}_{\ell,\alpha}$ with

$$\mathbf{v}_{1,A} = (0,0), \quad \mathbf{v}_{1,B} = \mathbf{O}(\theta_1) \cdot (0,d), \tag{3.3}$$

$$\mathbf{v}_{2,A} = \mathbf{O}(\theta_2) \cdot [(0,-d) + \mathbf{v}_0], \quad \mathbf{v}_{2,B} = \mathbf{O}(\theta_2) \cdot \mathbf{v}_0. \tag{3.4}$$

One can recover the standard Bernal stacked case for $\mathbf{v}_0 = 0$. The reciprocal lattice obtained from Fourier transformation is spanned by $\mathbf{G}_\ell = m_1 \mathbf{b}_{\ell,1} + m_2 \mathbf{b}_{\ell,2}$ with integers $m_{1,2}$. The reciprocal lattice vectors, $\mathbf{b}_{\ell,j}$ with $\ell = 1,2$, must fulfill the property $\mathbf{b}_{\ell,j} \cdot \mathbf{a}_{\ell,k} = 2\pi\delta_{jk}$. Thus, the vectors are obtained in the form

$$\mathbf{b}_{\ell,j} = \mathbf{O}(\theta_\ell)\mathbf{b}_j, \quad \mathbf{b}_1 = \frac{4\pi}{\sqrt{3}a} \begin{pmatrix} \frac{\sqrt{3}}{2} \\ \frac{1}{2} \end{pmatrix}, \quad \mathbf{b}_2 = \frac{4\pi}{\sqrt{3}a} \begin{pmatrix} \frac{-\sqrt{3}}{2} \\ \frac{1}{2} \end{pmatrix}, \tag{3.5}$$

where the physical spin-1/2 degree of freedom is kept implicit. However, one can find coupling of different valleys in different layers via interlayer tunneling for $\theta > 10°$. This is why the Bistritzer-MacDonald model focuses on $\theta < 10°$ [9]. The uncoupled layers can be then described as massless 2D Dirac fermions. For each layer, one can focus on just a single K point, corresponding to momentum $\mathbf{K}_\ell$ in layer ℓ:

$$\mathbf{K}_\ell = \mathbf{O}(\theta_\ell) \cdot \mathbf{K}, \text{ with } \mathbf{K} = (k_D,0), \text{ and } k_D \equiv \frac{4\pi}{3a}, \tag{3.6}$$

which finally results in

$$\mathbf{K}_\ell = k_D \begin{pmatrix} \cos\theta_\ell \\ -\sin\theta_\ell \end{pmatrix}. \tag{3.7}$$

The shift of the Dirac points for different layers is given by [37]

$$\Delta\mathbf{K} \equiv \mathbf{K}_2 - \mathbf{K}_1 = (0, k_\theta), \quad k_\theta \equiv 2k_D \sin\frac{\theta}{2}. \tag{3.8}$$

The crystal momentum in layer $\ell = 1,2$ is written as $\mathbf{O}(\theta_{1,2})\mathbf{K} + \mathbf{q}$, and the low-energy Dirac Hamiltonian for $qa \ll 1$ for the respective layer is

$$\mathcal{H}_\ell(\mathbf{q}) = v\mathbf{q} \cdot \sigma^{\theta_\ell}, \quad \sigma^{\theta_\ell}_{a=x,y} = e^{-i(\theta_\ell/2)\sigma_z} \sigma_a e^{i(\theta_\ell/2)\sigma_z}. \tag{3.9}$$

Here the Pauli matrices $\sigma_{x,y,z}$ and the identity σ_0 act in sublattice space. The velocity is approximately $v \approx 10^6 m/s$, see (2.22). In the following, matrices acting in layer space are denoted with $\tau_{x,y,z}$ for Pauli matrices and τ_0 for the identity.

3.2 Tunneling

In the next step, interlayer tunneling is allowed and the calculation is done via a tight binding approach. The interlayer tunneling can be described by $H_{21} = H_{12}^\dagger$ with [14]

$$H_{12} = \sum_{\mathbf{R}_1,\alpha;\mathbf{R}_2,\beta} c_{1,\alpha}^\dagger(\mathbf{R}_1) t_{\alpha\beta}(\mathbf{R}_1,\mathbf{R}_2) c_{2,\beta}(\mathbf{R}_2). \tag{3.10}$$

Here $t_{\alpha\beta}(\mathbf{R}_1,\mathbf{R}_2)$, defines a tunnel matrix element and the operator $c_{\ell,\alpha=A,B}(\mathbf{R}_\ell)$ stands for an electron at $\mathbf{R}_\ell + \mathbf{v}_{\ell,\alpha}$. N_ℓ is introduced as the number of unit cells in layer ℓ and then expanded in intralayer Bloch waves

$$c_{\ell,\alpha}(\mathbf{R}_\ell) = \frac{1}{\sqrt{N_\ell}} \sum_{\mathbf{k}_\ell \in \mathrm{BZ}_\ell} e^{i\mathbf{k}_\ell\cdot(\mathbf{R}_\ell+\mathbf{v}_{\ell,\alpha})} c_{\ell,\alpha}(\mathbf{k}_\ell). \tag{3.11}$$

In the two-center approximation, the tunnel coupling depends only on the distance $\sqrt{d_\perp^2 + r^2}$ between the atomic orbital centers, where $r = |\mathbf{r}|$ with $\mathbf{r} = (x,y)$ is their in-plane distance:

$$t_{\alpha\beta}(\mathbf{R}_1,\mathbf{R}_2) = \int_{\mathbf{R}^2} \frac{d^2\mathbf{p}}{(2\pi)^2} e^{i\mathbf{p}\cdot(\mathbf{R}_1+\mathbf{v}_{1,\alpha}-\mathbf{R}_2-\mathbf{v}_{2,\beta})} t_\perp(\mathbf{p}), \quad t_\perp(\mathbf{p}) = \int_{\mathbf{R}^2} d^2\mathbf{r} e^{-i\mathbf{p}\cdot\mathbf{r}} \tilde{t}_\perp(r), \tag{3.12}$$

here, $\tilde{t}_\perp(r)$ is independent of the sublattice indices. The two-center approximation implies momentum conservation for inter-layer tunneling processes. One can parametrize $\tilde{t}_\perp(r)$ as [38]

$$\tilde{t}_\perp(r) = \frac{d_\perp^2}{d_\perp^2 + r^2} V_{pp\sigma}\left(\sqrt{r^2 + d_\perp^2}\right) + \frac{r^2}{d_\perp^2 + r^2} V_{pp\pi}\left(\sqrt{r^2 + d_\perp^2}\right). \tag{3.13}$$

with Slater-Koster potentials given by

$$V_{pp\sigma}(\rho) = t_\perp e^{q_\sigma(1-\rho/d_\perp)}, \quad V_{pp\pi}(\rho) = -t e^{q_\pi(1-\rho/d)}. \tag{3.14}$$

Note that $V_{pp\sigma}(d_\perp) = t_\perp$ and $V_{pp\pi}(d) = -t$, with $t \approx 2.97$ eV and $t_\perp \approx 0.33$ eV follow from ab initio calculations [14] in agreement with experimental values. Equation (3.14) thus correctly describes Bernal stacked bilayer graphene as well as the case of monolayer graphene. In order to determine the parameter q_π in equation (3.14), we note that the next-nearest neighbor coupling in monolayer graphene is given by $t' \approx 0.1t$ [32, 39]. Since $t/t' = V_{pp\pi}(d)/V_{pp\pi}(\sqrt{3}d)$, we obtain $q_\pi \approx \frac{\ln(10)}{\sqrt{3}-1} \approx 3.15$. Finally, both terms in equation (3.13) should have the same asymptotic ρ-dependence for $\rho \to \infty$. Here only the charge term in the multipole expansion matters due to the fact that the precise form of the orbital is asymptotically irrelevant. We then find $q_\sigma = \frac{d_\perp}{d} q_\pi \approx 7.42$. Thus all parameters in equation (3.13) are given by [14, 32, 39]

$$d_\perp \approx 3.35\ , \quad d \approx 1.42\ , \quad t \approx 2.97 \text{ eV}, \quad t_\perp \approx 0.33 \text{ eV}, \quad q_\pi \approx 3.15, \quad q_\sigma \approx 7.42. \tag{3.15}$$

By performing the angular integration in equation (3.12) and using the Bessel function J_0 one obtains $t_\perp(p)$ with $p = |\mathbf{p}|$ from (3.13):

$$t_\perp(\mathbf{p}) = t_\perp(p) = 2\pi \int_0^\infty dr\, r J_0(pr) \tilde{t}_\perp(r). \tag{3.16}$$

Inserting equation (3.12) into equation (3.10) and using $\sum_{\mathbf{R}_\ell} e^{i\mathbf{k}\cdot\mathbf{R}_\ell} = N_\ell \sum_{\mathbf{G}_\ell} \delta_{\mathbf{k},\mathbf{G}_\ell}$ as well as $\delta_{\mathbf{k},\mathbf{k}'} \to \frac{(2\pi)^2}{\sqrt{N_1 N_2} A_{\mathrm{gr}}} \delta(\mathbf{k} - \mathbf{k}')$, one gets

$$H_{12} = \sum_{\alpha,\beta} \sum_{\mathbf{k}_{1,2} \in \mathrm{BZ}_{1,2}} c^\dagger_{1,\alpha}(\mathbf{k}_1) t_\perp^{\alpha\beta}(\mathbf{k}_1,\mathbf{k}_2) c_{2,\beta}(\mathbf{k}_2) \tag{3.17}$$

with the momentum-space tunneling amplitudes

$$t_\perp^{\alpha\beta}(\mathbf{k}_1,\mathbf{k}_2) = \frac{1}{A_{\mathrm{gr}}} \sum_{\mathbf{G}_1,\mathbf{G_2}} \delta_{\mathbf{k}_1+\mathbf{G}_1,\mathbf{k}_2+\mathbf{G}_2}\, e^{i(\mathbf{G}_1\cdot\mathbf{v}_{1,\alpha} - \mathbf{G}_2\cdot\mathbf{v}_{2,\beta})} t_\perp(|\mathbf{k}_1 + \mathbf{G}_1|). \tag{3.18}$$

Here one recognizes the generalized Umklapp condition [12] $\mathbf{k}_1 + \mathbf{G}_1 = \mathbf{k}_2 + \mathbf{G}_2$.

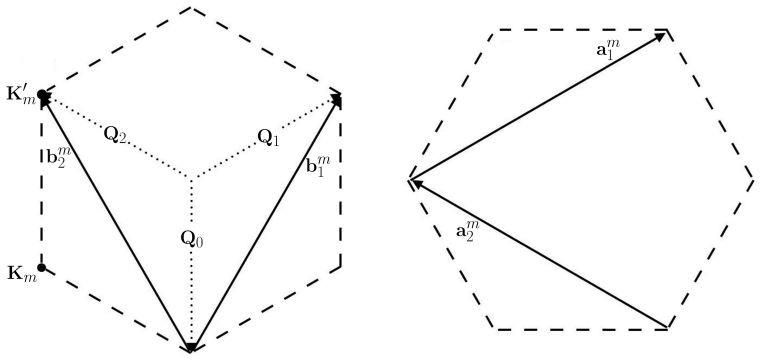

Figure 3.1: Illustration of important vectors.
left: Moiré Brillouin zone (mBZ) with the vectors $\mathbf{Q}_n$, $\mathbf{b}_n^m$ and the K, K' points shown in equations (3.23), (3.28) and (3.30). *right:* Real-space moiré unit cell with the $\mathbf{a}_n^m$ vectors in equation (3.28).

The following calculations assume small twist angles in the region of $0 < \theta \ll \pi/3$, where $k_\theta \ll k_D$. To obtain a low-energy theory, one can then focus on just one pair of nearby valleys in both layers. For most observables, the other decoupled valleys at momenta $-\mathbf{K}_\ell$ can be taken into account by a factor 2 as usual. This is the limit considered by Bistritzer and MacDonald [9], where issues of commensurability do not arise. The aspects of commensurability will be discussed in section 3.4.

Assuming a smooth function $t_\perp(p)$ near the K points for $qa \ll 1$ and taking the limit $|\mathbf{q}| \ll k_D$, one can neglect $\mathbf{q}$ in $t_\perp(p)$. Note, that also $k_\theta a \ll 1$ is fulfilled. One then can write (3.18) as

$$t_\perp^{\alpha\beta}(\mathbf{q}_1,\mathbf{q}_2) \simeq \frac{1}{A_{\mathrm{gr}}} \sum_{\mathbf{G}_1,\mathbf{G_2}} \delta_{\mathbf{K}_1+\mathbf{G}_1+\mathbf{q}_1,\mathbf{K}_2+\mathbf{G}_2+\mathbf{q}_2}\, e^{i[\mathbf{G}_1\cdot\mathbf{v}_{1,\alpha}-\mathbf{G}_2\cdot\mathbf{v}_{2,\beta}]} t_\perp(|\mathbf{K}_1+\mathbf{G}_1|). \tag{3.19}$$

The Bistritzer MacDonald model becomes useful due to the fact that only a few Umklapp processes contribute to (3.19). This is a result of an approximately constant $\tilde{t}_\perp(r < d_\perp)$ that rapidly decays with increasing r. One finds a rapid exponential decay of $t_\perp(p)$ for $pd_\perp > 1$. It is sufficient to keep only those $\mathbf{G}_1$ in equation (3.19) that satisfy $|\mathbf{K}_1 + \mathbf{G}_1| = k_D$. This corresponds to hopping between the three equivalent corner point pairs in the first Brillouin zone [9]. To that end, one restricts the summation in equation (3.19) to the three reciprocal lattice vectors for each individual layer $\ell = 1,2$

$$\mathbf{G}_\ell = \{\mathbf{g}_{\ell,n=0}, \mathbf{g}_{\ell,n=1}, \mathbf{g}_{\ell,n=2}\} = \{0, \mathbf{b}_{\ell,2}, -\mathbf{b}_{\ell,1}\}, \tag{3.20}$$

$$|\mathbf{K}_\ell + \mathbf{g}_{\ell,n}| = k_D = \frac{4\pi}{3a}. \tag{3.21}$$

Those three choices describe scattering between the three equivalent single layer K points. Since these points are shifted in a different way in both layers, they yield different momentum exchanges $\mathbf{Q}_n$ between the layers for $\theta \neq 0$. For a twist angle of $\theta = 0$ one recovers the Bernal stacked case with $\mathbf{Q}_n = 0$. Therefore, one can write with the interlayer-coupling $w \equiv \frac{t_\perp(k_D)}{A_{gr}} \simeq 110$ meV and the angle $\phi = 2\pi/3$

$$t_\perp^{\alpha\beta}(\mathbf{q}_1,\mathbf{q}_2) \simeq \sum_{n=0,1,2} \delta_{\mathbf{q}_2,\mathbf{q}_1+\mathbf{Q}_n} T_n^{\alpha\beta}, \quad T_n^{\alpha\beta} = w e^{i(\mathbf{g}_{1,n}\cdot\mathbf{v}_{1,\alpha}-\mathbf{g}_{2,n}\cdot\mathbf{v}_{2,\beta})}, \tag{3.22}$$

$$\mathbf{Q}_n = \mathbf{K}_1 + \mathbf{g}_{1,n} - (\mathbf{K}_2 + \mathbf{g}_{2,n}) = k_\theta \begin{pmatrix} \sin(n\phi) \\ -\cos(n\phi) \end{pmatrix}.$$

The value of w follows from (3.15) and is in agreement with Bistritzer and MacDonald's estimate in reference [9]. Explicitly

$$\mathbf{Q}_0 = -\Delta\mathbf{K} = k_\theta\,(0,-1), \quad \mathbf{Q}_1 = k_\theta \left(\frac{\sqrt{3}}{2}, \frac{1}{2}\right), \quad \mathbf{Q}_2 = -(\mathbf{Q}_0+\mathbf{Q}_1) = k_\theta \left(-\frac{\sqrt{3}}{2}, \frac{1}{2}\right). \tag{3.23}$$

The sublattice matrix $\hat{T}_n$ with $(\hat{T}_n)^{\alpha\beta} = T_n^{\alpha\beta}$ is given by

$$\hat{T}_{n=0,1,2} = w e^{i\alpha_n} \begin{pmatrix} e^{in\phi} & 1 \\ e^{-in\phi} & e^{in\phi} \end{pmatrix}, \quad \phi = \frac{2\pi}{3}, \quad \alpha_0 = 0, \quad \alpha_1 = -\mathbf{b}_2\cdot\mathbf{v}_0, \quad \alpha_2 = \mathbf{b}_1\cdot\mathbf{v_0}, \tag{3.24}$$

where one can use $e^{2i\phi} = e^{-i\phi}$. Note that for the case of zero twisted Bernal stacked layers with a twist angle $\theta = 0$ and shift $\mathbf{v}_0 = 0$, one can find a position independent tunneling matrix [9]

$$\sum_n T_n^{\alpha\beta} = 3w\delta_{\alpha A}\delta_{\beta B}. \tag{3.25}$$

Valley mixing by interlayer tunneling can be neglected for moderate large twist angles by introducing the low-energy fermion operators $\psi_{\ell,\alpha}(\mathbf{q}) \equiv c_{\ell,\alpha}(\mathbf{K}_\ell + \mathbf{q})$ near the $\mathbf{K}_\ell$ point, where one can recall $\mathbf{K}_\ell = \mathbf{O}(\theta_\ell)\mathbf{K}$ and require $qa \ll 1$. The Hamiltonian [9] gives

$$H = \sum_{\mathbf{q}}\sum_{\ell} \psi_\ell^\dagger(\mathbf{q}) \left[v\mathbf{q}\cdot\sigma^{\theta_\ell}\right] \psi_\ell(\mathbf{q}) + \sum_{\mathbf{q}}\sum_{n=0}^{2} \left(\psi_1^\dagger(\mathbf{q})\hat{T}_n\psi_2(\mathbf{q}+\mathbf{Q}_n) + \text{H.c.}\right). \tag{3.26}$$

It is convenient to introduce the dimensionless coupling parameter [9]

$$\alpha = \frac{w}{vk_\theta} \approx \frac{0.58}{\theta}. \tag{3.27}$$

For $\theta \ll \pi/3$, one finds $\hbar v k_\theta \sim 0.190 \cdot \theta$, with the angle in degrees and energy in eV, see reference [10]. One then arrives at the small-θ estimate given in the second step in equation (3.27). The parameter α fully controls the spectrum and combines the twist angle θ and the tunnel coupling strength into a single parameter.

3.3 Moiré superlattice

Using the Hamiltonian (3.26), one can see that repeated hopping processes generate an emergent moiré honeycomb lattice with nearest neighbor distance $|\mathbf{Q}_n| = k_\theta$ and lattice constant $\sqrt{3}k_\theta$. The corresponding moiré Brillouin zone is a hexagon with corners defined by the $\mathbf{Q}_n$, see Figure 3.1. The moiré Brillouin zone has two different Dirac points, $\mathbf{K}_m$ and $\mathbf{K}'_m$, illustrated in Figure 3.1. The A or B sites of this momentum-space honeycomb lattice correspond to the Dirac points $\mathbf{K}_{\ell=1,2}$ of the individual layers. One can choose the moiré reciprocal lattice vectors as $\mathbf{b}^m_{n=1,2} = \mathbf{Q}_n - \mathbf{Q}_0$. The corresponding real-space moiré basis vectors $\mathbf{a}^m_{1,2}$, holding the relation $\mathbf{a}^m_n \cdot \mathbf{b}^m_{n'} = 2\pi\delta_{nn'}$, are then given by [37]

$$\mathbf{b}_1^m = \sqrt{3}k_\theta \left(\frac{1}{2}, \frac{\sqrt{3}}{2}\right), \quad \mathbf{b}_2^m = \sqrt{3}k_\theta \left(-\frac{1}{2}, \frac{\sqrt{3}}{2}\right), \tag{3.28}$$

$$\mathbf{a}_1^m = \frac{4\pi}{3k_\theta} \left(\frac{\sqrt{3}}{2}, \frac{1}{2}\right), \quad \mathbf{a}_2^m = \frac{4\pi}{3k_\theta} \left(-\frac{\sqrt{3}}{2}, \frac{1}{2}\right). \tag{3.29}$$

The two Dirac points in the moiré Brillouin zone are located at

$$\mathbf{K}_m = \frac{-2\mathbf{b}_1^m + \mathbf{b}_2^m}{3} = -\mathbf{Q}_1, \quad \mathbf{K}'_m = -\mathbf{K}_m = +\mathbf{Q}_1, \tag{3.30}$$

and the basis sites of the real-space honeycomb moiré lattice can be chosen as

$$\mathbf{r}_A \equiv \mathbf{r}_0 = \frac{\mathbf{a}_1^m + 2\mathbf{a}_2^m}{3} = \frac{1}{\sqrt{3}}\frac{4\pi}{3k_\theta}\left(-\frac{1}{2}, \frac{\sqrt{3}}{2}\right), \tag{3.31}$$

$$\mathbf{r}_B = \frac{2\mathbf{a}_1^m + \mathbf{a}_2^m}{3} = \frac{1}{\sqrt{3}}\frac{4\pi}{3k_\theta}\left(\frac{1}{2}, \frac{\sqrt{3}}{2}\right). \tag{3.32}$$

In this notation $\mathbf{r}_A$ is the BA stacking point in real space, while $\mathbf{r}_B$ corresponds to the AB stacking point. At the origin of the hexagonal cell there are the regions of AA stacking cites. The real-space interference pattern is therefore characterized by the wavelength $L_m(\theta) = 4\pi/3k_\theta = a/[2\sin(\theta/2)]$.

Introducing the four-component spinors $\Psi_{\mathrm{BM}}(\mathbf{r}) = [\psi_{1A}(\mathbf{r}),\psi_{1B}(\mathbf{r}),\psi_{2A}(\mathbf{r}),\psi_{2B}(\mathbf{r})]^T$, the model (3.26) can be written as [9, 40]

$$H_{\mathrm{BM}} = \int d^2\mathbf{r}\Psi^\dagger_{\mathrm{BM}}(\mathbf{r})\mathcal{H}_{\mathrm{BM}}(\mathbf{r})\Psi_{\mathrm{BM}}(\mathbf{r}), \quad \mathcal{H}_{\mathrm{BM}}(\mathbf{r}) = \begin{pmatrix} \mathcal{H}_{D,1} & T(\mathbf{r}) \\ T^\dagger(\mathbf{r}) & \mathcal{H}_{D,2} \end{pmatrix}. \tag{3.33}$$

Compared to equation (3.26) the center of Bloch momentum is shifted to the Γ-point of the moiré Brillouin zone located at $\mathbf{\Gamma}^m = \frac{1}{2}(\mathbf{K}_1 + \mathbf{K}_2 + \mathbf{Q}_1 - \mathbf{Q}_2)$. The Γ-point characterizes the center of the moiré Brillouin zone. The 2×2 structure in equation (3.33) refers to layer space and uses

$$\mathcal{H}_{D,\ell} = v(-i\nabla - (-1)^\ell \mathbf{Q}_\ell)\cdot\sigma^{\theta_\ell} \tag{3.34}$$

with $\nabla = (\partial_x,\partial_y)$. The real-space hopping matrices $T(\mathbf{r})$ in sublattice space make the periodic structure of the inter-layer tunneling term explicit and are given by [9, 37]

$$T(\mathbf{r}) = \sum_{n=0,1,2} \hat{T}_n e^{-i(\mathbf{Q}_n - \mathbf{Q}_0)\cdot\mathbf{r}} = \hat{T}_0 + \hat{T}_1 e^{-i\mathbf{b}_1^m\cdot\mathbf{r}} + \hat{T}_2 e^{-i\mathbf{b}_2^m\cdot\mathbf{r}}, \tag{3.35}$$

$$\hat{T}_{n=0,1,2} = \kappa w\sigma_0 + w\cos(n\phi)\sigma_x + w\sin(n\phi)\sigma_y. \tag{3.36}$$

Here, the Bistritzer MacDonald model is generalized in the sense of coupling. The coupling w can differ for AA and AB inter-layer couplings. One can find equation (3.36) in the explicit form

$$\hat{T}_0 = w\left(\kappa\sigma_0 + \sigma_x\right), \quad \hat{T}_1 = w\left(\kappa\sigma_0 - \frac{1}{2}\sigma_x + \frac{\sqrt{3}}{2}\sigma_y\right), \quad \hat{T}_2 = w\left(\kappa\sigma_0 - \frac{1}{2}\sigma_x - \frac{\sqrt{3}}{2}\sigma_y\right). \tag{3.37}$$

The tunneling terms in a σ-dependent were introduced by the work of Lian et. al. [41]. Equation (3.35) shows in fact adjusted phases α_n such that equation (3.24) is recovered for $\kappa = 1$ with $\hat{T}_n = e^{i(\alpha_n + n\phi)}[\sigma_0 + \sigma_x\cos(n\phi) + \sigma_y\sin(n\phi)]$. Redefining $\alpha_n \to \alpha_n - n\phi$ and subsequently putting $\alpha_n = 0$, one arrives at (3.35).

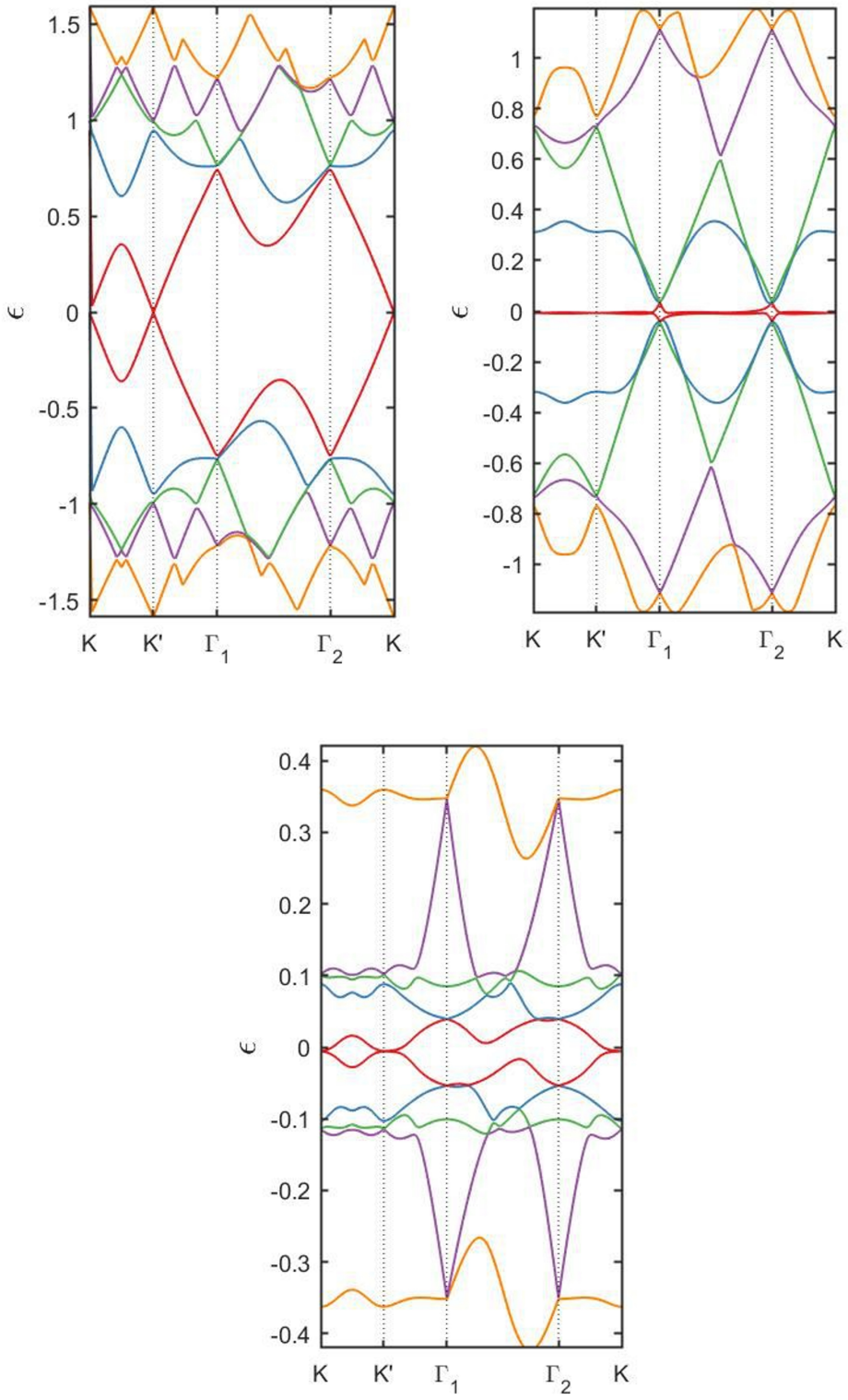

Figure 3.2: Energy spectrum and moiré bands.
Bandstructure computed from equation (3.38) along a trajectory $K \to K' \to \Gamma_1 \to \Gamma_2 \to K$ like [9] with $\kappa = 1$. *top left:* Calculations for a twist of $\alpha = 0.127$. *top right:* Twist angle of $\alpha = 0.606$. *bottom:* Same for $\alpha = 1.27$.

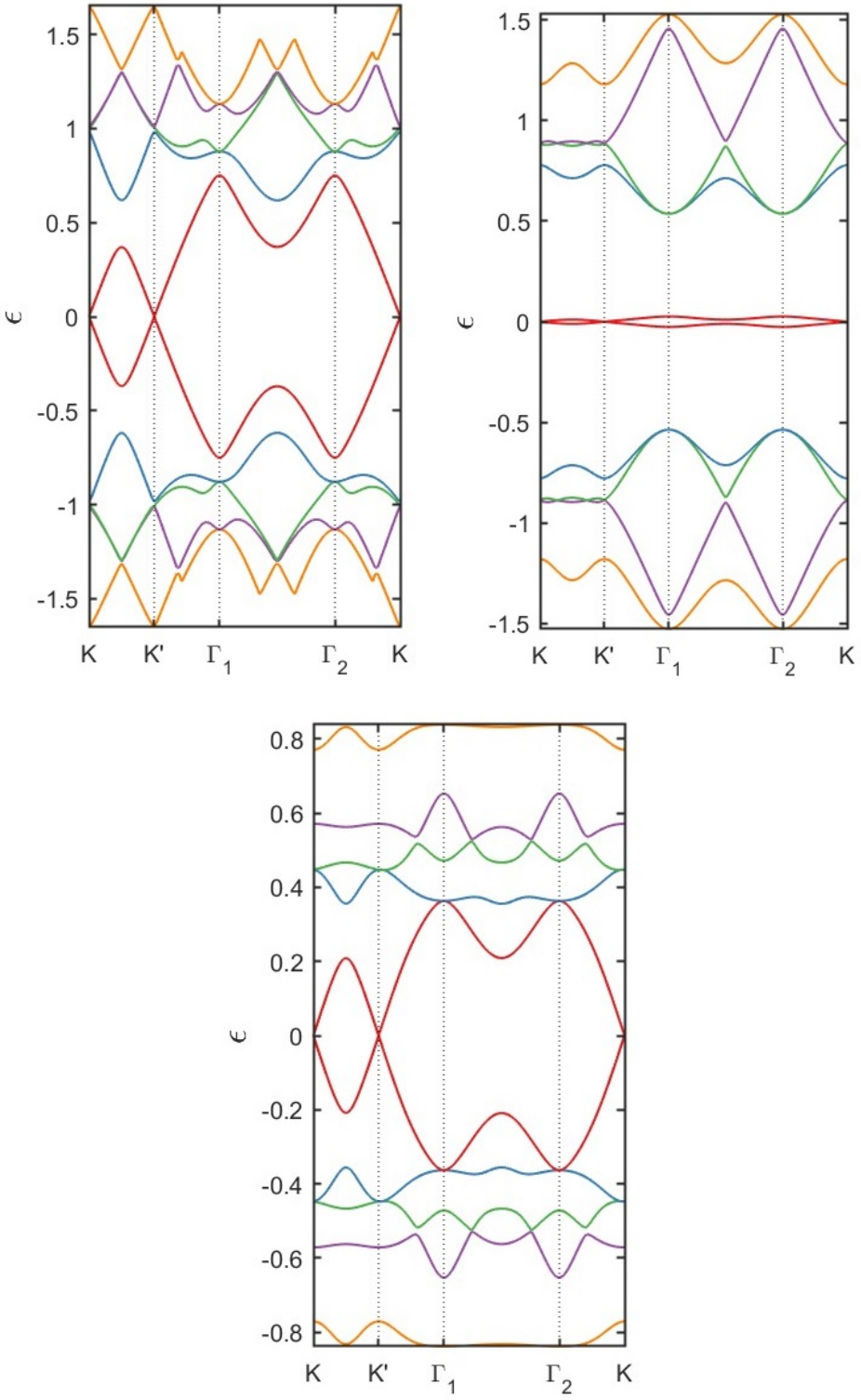

Figure 3.3: Energy spectrum and moiré bands.
Bandstructure computed from equation (3.38) along a trajectory $K \to K' \to \Gamma_1 \to \Gamma_2 \to K$ like [9] with $\kappa = 0$. *top left:* Calculations for a twist of $\alpha = 0.127$. *top right:* Twist angle of $\alpha = 0.606$. *bottom:* Same for $\alpha = 1.27$.

For the numerical evaluation of the band structure, $\mathbf{k}$ is defined within the moiré Brillouin zone and one can write the momentum as $\mathbf{q}_{n_1,n_2,\mathbf{k}} \equiv \mathbf{k} + n_1\mathbf{b}_1^m + n_2\mathbf{b}_2^m$ with $n_{1,2} \in Z$ such that equation (3.33) with $\psi_\ell(\mathbf{q}) \to \psi_{\ell,n_1,n_2,\mathbf{k}}$ assumes a form convenient for band structure calculations

$$\begin{aligned} H &= \sum_{\mathbf{k}\in \mathrm{mBZ}} \sum_{n_1,n_2} \Bigg(v \sum_{\ell=1,2} \psi^\dagger_{\ell,n_1,n_2,\mathbf{k}} \left([\mathbf{q}_{n_1,n_2,\mathbf{k}} - (-1)^\ell \mathbf{Q}_\ell] \cdot \sigma^{\theta_\ell} \right) \psi_{\ell,n_1,n_2,\mathbf{k}} + \\ &+ \left[\psi^\dagger_{1,n_1,n_2,\mathbf{k}} \left(\hat{T}_0 \psi_{2,n_1,n_2,\mathbf{k}} + \hat{T}_1 \psi_{2,n_1+1,n_2,\mathbf{k}} + \hat{T}_2 \psi_{2,n_1,n_2+1,\mathbf{k}} \right) + \mathrm{H.c.} \right] \Bigg) \end{aligned} \tag{3.38}$$

with the matrices $\hat{T}_n$ in the form (3.35). The sum over (n_1,n_2) must be truncated by selecting the bandwidth, where reference [9] argues that all momenta with $|\mathbf{q}_{n_1,n_2,\mathbf{k}}| < w/v$ should be taken into account. Typical results for the band structure obtained from equation (3.38) are shown in Figure 3.2 and reproduce the results of reference [9] quite accurately. Interestingly, Figure 3.3 indicates an accurate sensitivity of the bandstructure for a change in the parameter κ. The angle for which the bands flatten depend on κ. This will be studied in section 3.7. Here, the origin in reciprocal space is at the center of the first moiré Brillouin zone at $\Gamma_2 = \Gamma_m$. Different points of interest in Figure 3.2 can be expressed by $\mathbf{q}_{n_1,n_2,\mathbf{k}} \equiv \mathbf{k} + n_1\mathbf{b}_1^m + n_2\mathbf{b}_2^m$:

- K corresponds to $\mathbf{K}_m$ in Eq. (3.30), corresponding to $\mathbf{k} = -\mathbf{Q}_1$ and $n_1 = n_2 = 0$.
- K' is $\mathbf{K}'_m$ in Eq. (3.30), i.e., $\mathbf{k} = \mathbf{Q}_2$ and $n_1 = n_2 = 0$.
- Γ_1 is at $\mathbf{b}_2^m$ in Eq. (3.28), i.e., $\mathbf{k} = 0$ and $n_1 = 0, n_2 = 1$.
- Γ_2 is at the origin, $\mathbf{q} = \mathbf{k} = 0$, i.e., $n_1 = n_2 = 0$.

3.4 Commensurability

In this chapter, the case of commensurate twisted bilayer graphene [10] is briefly discussed. The shift $\mathbf{v}_0$ only shifts the moiré interference pattern but does not destroy it. Also, the energy spectrum is not affected by $\mathbf{v}_0$ like discussed before. One can therefore consider $\mathbf{v}_0 = 0$. A commensurate bilayer structure occurs whenever a superlattice translation maps the origin to another A_1B_2 point. This requirement leads to a Diophantine equation, which is most conveniently solved via symmetry analysis [10,42,43]. It turns out that all possible commensurate structures with $0 < \theta < \pi/3$ can be expressed in terms of pairs of positive co-prime integers (m,r):

$$\cos\theta(m,r) = 1 - \frac{r^2/2}{3m^2 + 3mr + r^2}. \tag{3.39}$$

The primitive translations $\{\mathbf{t}_1,\mathbf{t}_2\}$ of this Moiré superlattice come in two classes [42]. First for gcd(r,3) = 1, one finds

$$\text{SE odd}: \quad \mathbf{t}_1 = m\mathbf{a}_1 + (m+r)\mathbf{a}_2, \quad \mathbf{t}_2 = -(m+r)\mathbf{a}_1 + (2m+r)\mathbf{a}_2, \tag{3.40}$$

and the area of the unit cell is

$$A_{\text{sl}}^{(\text{SE odd})} = |\mathbf{t}_1 \times \mathbf{t}_2| = (3m^2+3mr+r^2)A_{\text{gr}} = (3m^2+3mr+r^2)\frac{\sqrt{3}a^2}{2}. \tag{3.41}$$

Here the vertices of the real-space Wigner-Seitz cell of the superlattice alternate between A_1B_2 sites and points with a hexagon center in both layers [10]. And secondly in the case of even SE, we have gcd(r,3) = 3, and each corner of the Wigner Seitz cell corresponds to a hexagon center in one layer and an atom (A or B) site in the other layer [10]. The primitive superlattice translations are now given by

$$\text{SE even}: \quad \mathbf{t}_1 = (m+r/3)\mathbf{a}_1 + (r/3)\mathbf{a}_2, \quad \mathbf{t}_2 = -(r/3)\mathbf{a}_1 + (m+r/3)\mathbf{a}_2, \tag{3.42}$$

$$A_{\text{sl}}^{(\text{SE even})} = (m^2+mr+r^2/3)\frac{\sqrt{3}a^2}{2}. \tag{3.43}$$

3.5 Limitations

Next, it will be shown that the angles α_n in equation (3.24), which are due to the relative shift vector $\mathbf{v}_0$, can be removed by a gauge transformation, i.e., the spectrum for infinitely extended samples of twisted bilayer graphene is independent of $\mathbf{v}_0$. To see this, one starts from equation (3.38) and considers a model where the $\hat{T}_n$ matrices are replaced by $e^{i\alpha_n}\hat{T}_n$ with arbitrary choice of α_n. Next, defining the phases $\varphi_{\ell,n_1,n_2} = \gamma\delta_{\ell,1} + \eta n_1 + \xi n_2$, with arbitrary parameters (γ,η,ξ), which can be chosen identical for all $\mathbf{k}$ and for both spinor entries. One then performs the gauge transformation $\psi_{\ell,n_1,n_2,\mathbf{k}} \to e^{-i\varphi_{\ell,n_1,n_2}}\psi_{\ell,n_1,n_2,\mathbf{k}}$. Choosing $\gamma = -\alpha_0$, $\eta = \alpha_1 - \alpha_0$, and $\xi = \alpha_2 - \alpha_0$, the phases α_n are gauged away from H in equation (3.38). Even if the spectrum is unaffected by $\mathbf{v}_0$, observables such as the interference pattern can still depend on the shift.

For $\alpha \gg 1$, one starts from the Bernal case, $\theta = 0$, and arrives to leading order at the low-energy Hamiltonian [44]

$$\left[\mathcal{H}_{\text{eff}}^{(\alpha\gg1)}\right]_{11} = \left[\mathcal{H}_{\text{eff}}^{(\alpha\gg1)}\right]_{22} = 0, \tag{3.44}$$

$$\left[\mathcal{H}_{\text{eff}}^{(\alpha\gg1)}\right]_{12} = -\frac{w}{\alpha^2}\left(\frac{(k_x-ik_y)^2}{k_\theta^2} - \frac{1}{4k_\theta^2}(\Delta K_x - i\Delta K_y)^2\right), \tag{3.45}$$

$$\left[\mathcal{H}_{\text{eff}}^{(\alpha\gg1)}\right]_{21} = -\frac{w}{\alpha^2}\left(\frac{(k_x+ik_y)^2}{k_\theta^2} - \frac{1}{4k_\theta^2}(\Delta K_x + i\Delta K_y)^2\right). \tag{3.46}$$

The Hamiltonian is expressed in the basis of states (A_1B_2). These states decouple from the (B_1A_2) states which are strongly hybridized and move to high energy.
For $\theta = 0$, one recovers the Bernal bilayer Hamiltonian. The next step is to analyze the low-energy limit with $q \ll k_\theta$ and $\alpha \ll 1$, which excludes the strong coupling regime $\theta < 2^\circ$. In this limit, we can truncate the full honeycomb lattice in Hamiltonian (3.38) down to just the lowest order. An additional simplification arises since for relatively small twists, the θ-dependence in the Pauli matrices σ^{θ_ℓ} causes only subleading effects [9]. One can use the 8-spinor notation

$$\Psi_{\mathbf{k}} = [\phi_{\ell=1}(\mathbf{k}), \phi_{\ell=2,n=0}(\mathbf{k}+\mathbf{Q}_0), \phi_{2,1}(\mathbf{k}+\mathbf{Q}_1), \phi_{2,2}(\mathbf{k}+\mathbf{Q}_2)]^T, \tag{3.47}$$

where each spinor entry $\phi_{\ell,n}$ has sublattice structure and $\mathbf{k} \in$ mBZ, see equation (3.38). One uses a representation [9] where $\mathbf{k}$ is taken with respect to $\mathbf{K}_m$. The lowest-order truncated single-particle Hamiltonian has the matrix form:

$$\mathcal{H}_{\mathbf{k}} = \begin{pmatrix} h(\mathbf{k}) & \hat{T}_0 & \hat{T}_1 & \hat{T}_2 \\ \hat{T}_0^\dagger & h(\mathbf{k}+\mathbf{Q}_0) & 0 & 0 \\ \hat{T}_1^\dagger & 0 & h(\mathbf{k}+\mathbf{Q}_1) & 0 \\ \hat{T}_2^\dagger & 0 & 0 & h(\mathbf{k}+\mathbf{Q}_2) \end{pmatrix}, \tag{3.48}$$

with $h(\mathbf{k}) = v\mathbf{k}\cdot\boldsymbol{\sigma}$. Assuming $\mathbf{k} \neq 0$ gives $h^{-1}(\mathbf{k}) = \frac{1}{vk^2}\mathbf{k}\cdot\boldsymbol{\sigma}$. First one can show that for $\mathbf{k} = 0$, right at the Dirac point $\mathbf{K}_m$, the Hamiltonian (3.48) has a two-fold degenerate zero-energy ground state, $\Psi^{(0)}_{j=1,2}$. Note, that the spinor components in layer 2 follow from the layer 1 spinor according to

$$\phi_{2,n} = -h^{-1}(\mathbf{Q}_n)\hat{T}_n^\dagger\phi_1. \tag{3.49}$$

Next one can write

$$\mathbf{Q}_n\cdot\sigma = ik_\theta \begin{pmatrix} 0 & e^{-in\phi} \\ -e^{in\phi} & 0 \end{pmatrix}. \tag{3.50}$$

This yields together with equation (3.24)

$$\hat{T}_n h^{-1}(\mathbf{Q}_n)\hat{T}_n^\dagger \propto \hat{T}_n\mathbf{Q}_n\cdot\sigma\hat{T}_n^\dagger = 0. \tag{3.51}$$

For zero modes, relation (3.49) then implies $\hat{T}_n\phi_{2,n} = 0$, and equation (3.48) tells us that ϕ_1 has to be one of the two zero modes of the decoupled layer 1, where $\phi_{2,n}$ then follows from equation (3.49). In this case, decoupled layers lead to $w = 0$. The two zero-mode states $\Psi^{(0)}_j$ are not normalized yet. Using the relations

$$\hat{T}_n\hat{T}_n^\dagger = 2w^2 \begin{pmatrix} 1 & e^{-in\phi} \\ e^{in\phi} & 1 \end{pmatrix} \text{ and } \sum_n e^{in\phi} = 0 \tag{3.52}$$

as well as $\langle\phi_1|\phi_1\rangle = \langle\phi_{2,n}|\phi_{2,n}\rangle = 1$ and $h^{-2}(\mathbf{Q}_n) = (vk_\theta)^{-2}$ one finds [9]

$$\langle\Psi^{(0)}_j|\Psi^{(0)}_j\rangle = 1 + \alpha^2\sum_{n=0,1,2}\langle\phi_{2,n}|\hat{T}_n\hat{T}_n^\dagger|\phi_{2,n}\rangle = 1 + 6\alpha^2. \tag{3.53}$$

To linearize in terms of $\mathbf{k}$ one uses the method of projecting $\mathcal{H}_{\mathbf{k}}$ to the low-energy space spanned by the two zero-mode states. Taking into account the normalization factor, the effective Hamiltonian for layer 1 has the matrix elements

$$\langle \Psi_i^{(0)} | \mathcal{H}_{\text{eff}}(\mathbf{k}) | \Psi_j^{(0)} \rangle = \frac{v}{1+6\alpha^2} [\phi_1^{(i)}]^\dagger \left(\mathbf{k}\cdot\sigma + \sum_n \hat{T}_n h^{-1}(\mathbf{Q}_n)\, \mathbf{k}\cdot\sigma\, h^{-1}(\mathbf{Q}_n) \hat{T}_n^\dagger \right) \phi_1^{(j)}. \tag{3.54}$$

Using equation (3.50) and computing the sum over n gives the explicit expression

$$\begin{aligned}
&\sum_{n=0,1,2} \hat{T}_n h^{-1}(\mathbf{Q}_n)\, \mathbf{k}\cdot\sigma\, h^{-1}(\mathbf{Q}_n) \hat{T}_n^\dagger \\
&= -\frac{\alpha^2}{w^2} \sum_n \hat{T}_n \begin{pmatrix} 0 & e^{-in\phi} \\ -e^{in\phi} & 0 \end{pmatrix} \begin{pmatrix} 0 & k_x - ik_y \\ k_x + ik_y & 0 \end{pmatrix} \begin{pmatrix} 0 & e^{-in\phi} \\ -e^{in\phi} & 0 \end{pmatrix} \hat{T}_n^\dagger \\
&= -\alpha^2 \sum_n \begin{pmatrix} -e^{in\phi} & 1 \\ -e^{-in\phi} & e^{in\phi} \end{pmatrix} \begin{pmatrix} 0 & k_x - ik_y \\ k_x + ik_y & 0 \end{pmatrix} \begin{pmatrix} e^{-in\phi} & e^{in\phi} \\ -1 & -e^{-in\phi} \end{pmatrix} \\
&= -\alpha^2 \sum_n \begin{pmatrix} k_x + ik_y & -(k_x - ik_y)e^{in\phi} \\ (k_x + ik_y)e^{in\phi} & -(k_x - ik_y)e^{-in\phi} \end{pmatrix} \begin{pmatrix} e^{-in\phi} & e^{in\phi} \\ -1 & -e^{-in\phi} \end{pmatrix} \\
&= -3\alpha^2 \mathbf{k}\cdot\sigma.
\end{aligned} \tag{3.55}$$

To lowest order in α and k, interlayer coupling effects are thus encoded by a renormalization of the Fermi velocity in layer 1, $\mathcal{H}_{\text{eff}}(\mathbf{k}) = v_{\text{eff}}(\theta)\, \mathbf{k}\cdot\sigma$, with [9, 40]

$$v_{\text{eff}}(\theta) = \frac{1-3\alpha^2}{1+6\alpha^2} v \simeq \left[1 - 9\alpha^2 + \mathcal{O}(\alpha^4)\right] v. \tag{3.56}$$

This perturbative expression predicts that for decreasing θ, the first zero of v_{eff} is reached at $\alpha = 1/3$ which corresponds to $\theta \approx 1.74°$, which is bigger than the correct non-perturbative first magic angle $\theta \approx 1.05°$. This is not surprising since the 8-band model (3.48) is only accurate for $\theta \gtrsim 2°$ [9]. The above argument also does not explain why the entire band is flat at magic angles. These aspects are the motivation for the next chapter.

3.6 Flat bands and magic angle

This chapter will focus on the strong coupling regime $\theta < 2°$ and discuss for this instance the importance of the work by Tarnopolsky, Kruchkov and Vishwanath [37]. Here, the real space version of the Bistritzer and MacDonald model in equation (3.33) will be used which manifests the chiral nature of the model for $\kappa = 0$. The case $\kappa < 1$, i.e., $w_{AA} < w_{AB}$ is relevant for $\theta < 2°$ because of the energetically preferred

Bernal stacking [11, 45]. Recent RG calculations for the interacting case argue that at low energies, the chiral limit is dynamically approached [46]. For $\kappa = 0$, analytical calculations are possible.

Note that, for $\kappa = 0$, it is possible to undo the rotation of the Pauli matrices by a unitary transformation. In addition, it is convenient to retain the momentum resulting from the expansion around $(\mathbf{K}_m, \mathbf{K}'_m)$ for the different layer entries in Ψ, where one can put $\mathbf{K}'_m = -\mathbf{K}_m$. Thus, the chiral spinor representation has the form [37]

$$\Psi_{c,\mathbf{k}}(\mathbf{r}) = e^{-i\tau_z \mathbf{K}_m \cdot \mathbf{r}} e^{i\frac{\theta}{4}\sigma_z\tau_z} \Psi_{\mathrm{BM},\mathbf{k}}(\mathbf{r}) = \begin{pmatrix} \psi_{1A} \\ \psi_{2A} \\ \psi_{1B} \\ \psi_{2B} \end{pmatrix} = \begin{pmatrix} \phi_A \\ \phi_B \end{pmatrix}, \tag{3.57}$$

where the spinor entries are reshuffled such that the upper and lower two entries ϕ_A and ϕ_B refer to sublattice block A and B. Bloch boundary conditions are now given by [47]

$$\Psi_{c,\mathbf{k}}(\mathbf{r} + \mathbf{a}_n^m) = e^{i(\mathbf{k} - i\tau_z \mathbf{K}_m)\cdot \mathbf{a}_n^m} \Psi_{c,\mathbf{k}}(\mathbf{r}). \tag{3.58}$$

For $\kappa = 0$, $T(\mathbf{r})$ in equation (3.35) is invariant under the rotation (3.57) because of

$$e^{i\frac{\theta}{4}\sigma_z\tau_z} \left[\{\sigma_x \cos(n\phi) + \sigma_y \sin(n\phi)\} \frac{\tau_x - i\tau_y}{2} \right] e^{-i\frac{\theta}{4}\sigma_z\tau_z} = \{\sigma_x \cos(n\phi) + \sigma_y \sin(n\phi)\} \frac{\tau_x - i\tau_y}{2} \tag{3.59}$$

where the bracketed term commutes with $\sigma_z\tau_z$. Putting $v = 1$, the Hamiltonian (3.33) thereby takes the chiral form [37]

$$H_c = \int d^2\mathbf{r}\ \Psi_c^\dagger(\mathbf{r}) \mathcal{H}_c(\mathbf{r}) \Psi_c(\mathbf{r}) \quad \text{with} \quad \mathcal{H}_c(\mathbf{r}) = \begin{pmatrix} 0 & D(\mathbf{r}) \\ D^\dagger(\mathbf{r}) & 0 \end{pmatrix}. \tag{3.60}$$

The 2×2 structure in $\mathcal{H}_c$ refers to sublattice space, where $D(\mathbf{r})$ has a 2×2 structure in layer space and reads

$$D(\mathbf{r}) \equiv \begin{pmatrix} -i\partial & wU_{-\phi}(\mathbf{r}) \\ wU_{-\phi}(-\mathbf{r}) & -i\partial \end{pmatrix}, \quad D^\dagger(\mathbf{r}) = \begin{pmatrix} -i\bar{\partial} & wU_{\phi}(\mathbf{r}) \\ wU_{\phi}(-\mathbf{r}) & -i\bar{\partial} \end{pmatrix}, \tag{3.61}$$

$$U_\phi(\mathbf{r}) \equiv \sum_{n=0,1,2} e^{in\phi} e^{-i\mathbf{Q}_n \cdot \mathbf{r}} = U^*_{-\phi}(-\mathbf{r}), \quad \partial = \partial_x - i\partial_y, \quad \bar{\partial} = \partial_x + i\partial_y, \quad \phi = 2\pi/3.$$

With α in equation (3.27) one has $w = \alpha k_\theta$. Furthermore, α is the only dimensionless parameter of the Hamiltonian (3.60) and fully controls all the physics.

The chiral model (3.60) reveals a set of different symmetries. Firstly, the model shows charge-$U(1)$ valley symmetry. The theories describing states near the valleys K_ℓ and those near $-K_\ell$ decouple and are related by time reversal $\mathcal{T}$. This is also a symmetry of the full Bistritzer MacDonald model [9]. Here only the $+K_\ell$ valleys are considered. Secondly, the model exhibits a chiral symmetry $\{\mathcal{H}_c, \sigma_z\tau_0\} = 0$. This relation requires

that there are no inter- or intra-layer (AA or BB) couplings. It directly implies a particle-hole symmetric spectrum where all eigenenergies come in $\pm E$ pairs and $E = 0$ is special. Furthermore, the model (3.60) shows C_3 rotation symmetry and $\mathcal{M}_y$ mirror symmetry which are not crucial in the following. Next is the $C_2\mathcal{T}$ symmetry. $T(\mathbf{r})$ in equation (3.35), with $\kappa = 0$, satisfies $T(\mathbf{r}) = \sigma_x T^*(-\mathbf{r})\sigma_x$. This relation implies

$$\tau_y D^\dagger(\mathbf{r})\tau_y = -D^\dagger(-\mathbf{r}), \tag{3.62}$$

for the linear Dirac spectrum. In the chiral basis, interlayer tunneling from top to bottom layer is then identical to tunneling from bottom to top layer together with spatial inversion. Moreover, a intra-valley inversion symmetry ($\mathcal{I}$) [47]

$$\mathcal{I}\mathcal{H}_c(\mathbf{r})\mathcal{I}^\dagger = \mathcal{H}_c(-\mathbf{r}), \quad \mathcal{I} = \sigma_z\tau_y = \mathcal{I}^\dagger = \mathcal{I}^{-1}, \tag{3.63}$$

is introduced due to equation (3.62) with $\kappa = 0$ and the linear Dirac spectrum. This symmetry maps Bloch states $\mathbf{k} \to -\mathbf{k}$ within the moiré Brillouin zone without mixing valleys. The intra-valley inversion symmetry implies that the dispersion of the chiral model is not only particle-hole symmetric but also inversion symmetric. To show this, note that for each eigenstate $\Psi_\mathbf{k}$ (with $\mathbf{k} \in$ mBZ) to energy $E_\mathbf{k}$, there is another eigenstate from the condition (3.63), $\Psi'_\mathbf{k}(\mathbf{r}) = \mathcal{I}\Psi_\mathbf{k}(-\mathbf{r})$, with the same energy:

$$\mathcal{H}_c(\mathbf{r})\Psi'_\mathbf{k}(\mathbf{r}) = \mathcal{H}_c(\mathbf{r})\mathcal{I}\Psi_\mathbf{k}(-\mathbf{r}) = \mathcal{I}\mathcal{H}_c(-\mathbf{r})\Psi_\mathbf{k}(-\mathbf{r}) = E_\mathbf{k}\Psi'_\mathbf{k}(\mathbf{r}). \tag{3.64}$$

Assuming a nondegenerate Bloch momentum, $\Psi'_\mathbf{k}(\mathbf{r})$ must be equivalent to $\Psi_{-\mathbf{k}}(\mathbf{r})$, i.e.,

$$\Psi_{-\mathbf{k}}(\mathbf{r}) = e^{i\zeta_\mathbf{k}}\sigma_z\tau_y\Psi_\mathbf{k}(-\mathbf{r}). \tag{3.65}$$

The same state will be reached by applying this transformation twice. This implies $\zeta_{-\mathbf{k}} = -\zeta_\mathbf{k}$. For the spinors $\phi_{A,\mathbf{k}}$ and $\phi_{B,\mathbf{k}}$ in the form of (3.57), which are 2-spinors in layer space, equation (3.65) implies

$$\phi_{A,\mathbf{k}}(\mathbf{r}) = e^{i\zeta_\mathbf{k}}\tau_y\phi_{A,-\mathbf{k}}(-\mathbf{r}), \quad \phi_{B,\mathbf{k}}(\mathbf{r}) = -e^{i\zeta_\mathbf{k}}\tau_y\phi_{B,-\mathbf{k}}(-\mathbf{r}). \tag{3.66}$$

At inversion symmetric points, $\mathbf{k}_{inv} = -\mathbf{k}_{inv}$ mod $\mathbf{G}^m$ with reciprocal lattice vectors $\mathbf{G}^m$ of the moiré Brillouin zone, $\zeta_{\mathbf{k}_{inv}}$ must be 0 or π. This inversion eigenvalue, $\eta = e^{i\zeta} = \pm 1$, can be extracted at the Γ-point of the moiré Brillouin zone, i.e., for $\mathbf{k}_{inv} = 0$:

$$\phi_{A,\mathbf{k}=0}(\mathbf{r}) = \eta\tau_y\phi_{A,\mathbf{k}=0}(-\mathbf{r}). \tag{3.67}$$

For the flat band appearing at the nth magic angle (see below), Ref. [47] found numerically that this inversion parity number alternates, $\eta_n = (-1)^{n+1}$.

In fact, there are certain values of $\alpha = \alpha_n$, which define the sequence of magic angles θ_n according to equation (3.27), see Figure 3.4. This was also studied by [37, 47]. There are two exact zero modes for all $\mathbf{k} \in$ mBZ, i.e., one finds two truly flat bands,

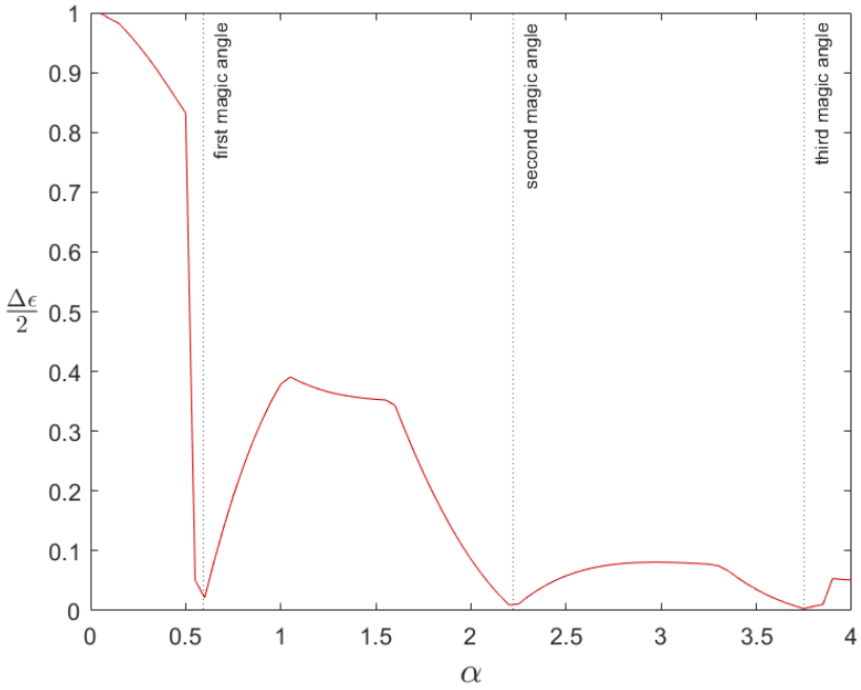

Figure 3.4: Periodicity of the magic angles for $\kappa = 0$.
The band gap $\Delta\epsilon$ vanishes for different so called magic angles, which exhibits a periodicity. Note that here just half of the band gap is plotted.

$E_{\mathbf{k}} = 0$. The chiral model yields a periodicity $\alpha_{n+1} \approx \alpha_n + 3/2$ for the magic angles, with $\alpha_n = \alpha(\theta_n)$.

Flat band states are localized either on sublattice A or B and follow as solutions of [37]

$$D(\mathbf{r})\phi_{B,\mathbf{k}}(\mathbf{r}) = 0, \quad D^\dagger(\mathbf{r})\phi_{A,\mathbf{k}}(\mathbf{r}) = 0. \tag{3.68}$$

One of these equations has to be solved, the other can be constructed from the solution. For instance, suppose one had solved the first equation in (3.68). From the knowledge of $\phi_{B,\mathbf{k}}(\mathbf{r})$, the second solution, $\phi_{A,\mathbf{k}}(\mathbf{r})$, follows by comparing $D^\dagger(\mathbf{r})\phi_{A,\mathbf{k}}(\mathbf{r}) = \left[D(-\mathbf{r})\phi^*_{A,\mathbf{k}}(\mathbf{r})\right]^* = 0$ and $D(\mathbf{r})\phi_{B,\mathbf{k}}(\mathbf{r}) = 0$ in the form

$$\phi_{A,\mathbf{k}}(\mathbf{r}) = \phi^*_{B,\mathbf{k}}(-\mathbf{r}), \tag{3.69}$$

possibly up to a phase factor. Focussing on $\phi_{A,\mathbf{k},\ell}(\mathbf{r})$ with $\ell = 1,2$ with equation (3.68) yields

$$-i\bar{\partial}\phi_{A,\mathbf{k},1}(\mathbf{r}) + wU_\phi(\mathbf{r})\phi_{A,\mathbf{k},2}(\mathbf{r}) = 0, \quad -i\bar{\partial}\phi_{B,\mathbf{k},2}(\mathbf{r}) + wU_\phi(-\mathbf{r})\phi_{A,\mathbf{k},1}(\mathbf{r}) = 0. \tag{3.70}$$

A zero mode for arbitrary α, which is pinned to zero energy by chiral symmetry [37], can be found right at the K point of the moiré Brillouin zone. To see this, note that at the corner points of the real-space cell, $\mathbf{r} = \pm\mathbf{r}_0$ in equation (3.31), see Figure 3.1, one finds

$$\mathbf{Q}_n \cdot \mathbf{r}_0 = (n-1)\phi \quad \longrightarrow \quad U_\phi(\mathbf{r}_0) = 3e^{i\phi}, \quad U_\phi(-\mathbf{r}_0) = e^{-i\phi}\sum_n e^{-in\phi} = 0. \tag{3.71}$$

The second equation in (3.70) then implies $\phi_{A,\mathbf{K}_m,2}(\mathbf{r}_0) = 0$ for arbitrary α since one can effectively put $\bar{\partial} \to 0$ at the Dirac point, i.e.,

$$\phi_{A,\mathbf{K}_m,2}(\pm\mathbf{r}_0) = \phi_{B,\mathbf{K}_m,2}(\pm\mathbf{r}_0) = 0. \tag{3.72}$$

One can then define a generalized Fermi velocity [37]

$$v_F(\alpha) = \sum_\ell \phi_{A,\mathbf{K}_m,\ell}(\mathbf{r})\phi_{A,\mathbf{K}_m,\ell}(-\mathbf{r}), \tag{3.73}$$

which is independent of $\mathbf{r}$. Indeed, then $\bar{\partial}v_F(\alpha) = 0$ by using equation (3.70), i.e., $v_F(\alpha)$ is a holomorphic function of z. Since this function is also cell-periodic, it therefore must be constant. By setting $\mathbf{r} = \mathbf{r}_0$ in the generalized form of the Fermi velocity (3.73), the condition $v_F(\alpha) = 0$ implies that the $\ell = 1$ component of either $\phi_{A,\mathbf{K}_m}(\mathbf{r}_0)$ or $\phi_{A,\mathbf{K}_m}(-\mathbf{r}_0)$ must vanish as well. This condition determines the sequence of magic angles.

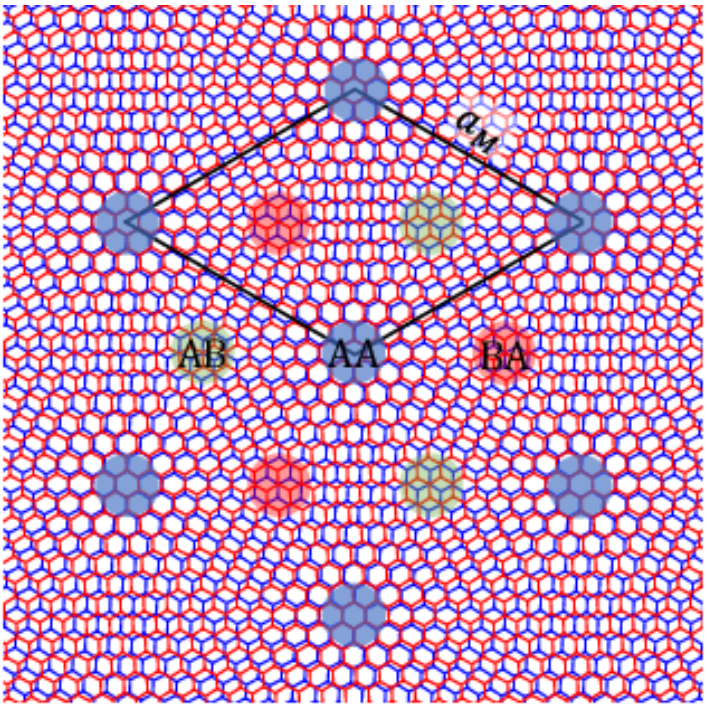

Figure 3.5: Geometry of stacking regions. Figure from [48].
Moiré superlattice with color coded stacking regions.

The next step is to generate magic-angle solutions for $\alpha = \alpha_n$ at arbitrary $\mathbf{k}$, i.e., states $\phi_{A,\mathbf{k}}(\mathbf{r})$, from the above solution at $\mathbf{k} = \mathbf{K}_m$ by using the fact that

$$D^\dagger(\mathbf{r})[F_\mathbf{k}(z)\phi_{A,\mathbf{K}_m}(\mathbf{r})] = 0 \tag{3.74}$$

automatically holds for any holomorphic function $F(z)$ with $z = x + iy$. Note that $D^\dagger(\mathbf{r})$ only contains the anti-holomorphic derivative $\bar{\partial}$. Functions thus constructed

might not be normalizable since a non-constant $F(z)$ cannot be bounded. The only exception arises if both components of $\phi_{A,K_m}(\mathbf{r}) = 0$ vanish at some point in space, i.e., at $\mathbf{r}_0$ or $-\mathbf{r}_0$. This then corresponds to the magic angles. By using an analogy to fractional quantum Hall states on a torus, the function $F_{\mathbf{k}}(z)$ is [37, 47]

$$F_{\mathbf{k}}(z) = e^{z_{\mathbf{k}}^*\left(z-\frac{z_{\mathbf{k}}}{2}\right)}\frac{\sigma(z-z_k)}{\sigma(z-z_0)}, \quad z = x+iy, \quad z_0 = x_0+iy_0, \tag{3.75}$$

$$z_{\mathbf{k}} = x_{\mathbf{k}} + iy_{\mathbf{k}}, \quad (\mathbf{r}_{\mathbf{k}})^{a=x,y} = \mathbf{r}_0^a + \epsilon^{ab}(\mathbf{k}-\mathbf{K}_m)_b, \tag{3.76}$$

with the modified Weierstrass sigma function $\sigma(z)$.

3.7 Robustness of magic angle

In this section the influence of different coupling strengths to the bandstructure and the magic angles will be discussed. This was briefly done for a few selected parameters in [37]. Following (3.36) and (3.37) one can distinguish two different couplings. The ratio of these couplings is given by the parameter κ. The coupling in AB/BA stacked or Bernal stacked regions is governed by $w_0 = w$ and $w_1 = \kappa w$ represents the coupling in AA stacked regions. For illustration of stacking regions see Figure 3.5 or reference [49]. When comparing Figures 3.2 and 3.3 it becomes clear that the variation of κ and thus the change in the ratio of w_0 and w_1 have an obvious influence on the band structure. Therefore, a change of the respective magic angles is also noticeable. In section 3.6 κ was set to zero and the magic angles $\alpha_1 \approx 0.6$, $\alpha_2 \approx 2.2$ and $\alpha_3 \approx 3.8$ had been revealed. For $\kappa = 1$ the magic angles are shifted towards lower values of α, see Figure 3.6. In this case, the magic angle for the third band is shifted to $\alpha_3 \approx 1.8$ and the magic angle of the second band to $\alpha_2 \approx 1.1$. Interestingly, for the first magic angles there seems to be no influence and one can still find $\alpha \approx 0.6$.

The robustness of the first magic angle is also confirmed for the case $\kappa = 0.5$. Figure 3.6 *bottom* also shows that the first magic angle can be just slightly influenced by variation of the coupling ratio. However, the second and third magic angles are shifted like illustrated in Figure 3.6 *bottom*.
Finally, Figure 3.7 shows the full evolution of the magic angle α for the whole spectrum of κ. This also confirms that the first angle is only marginally influenced. Contrary to this, the second and third magic angles exhibit a remarkable dependency on κ. Interestingly, the smallest α is needed for $\kappa = 1$ for both bands, corresponding to equal contribution of the couplings $w_0 = w_1$, while the bands flatten for larger α assuming $w_0 = w$ and $w_1 = 0$.

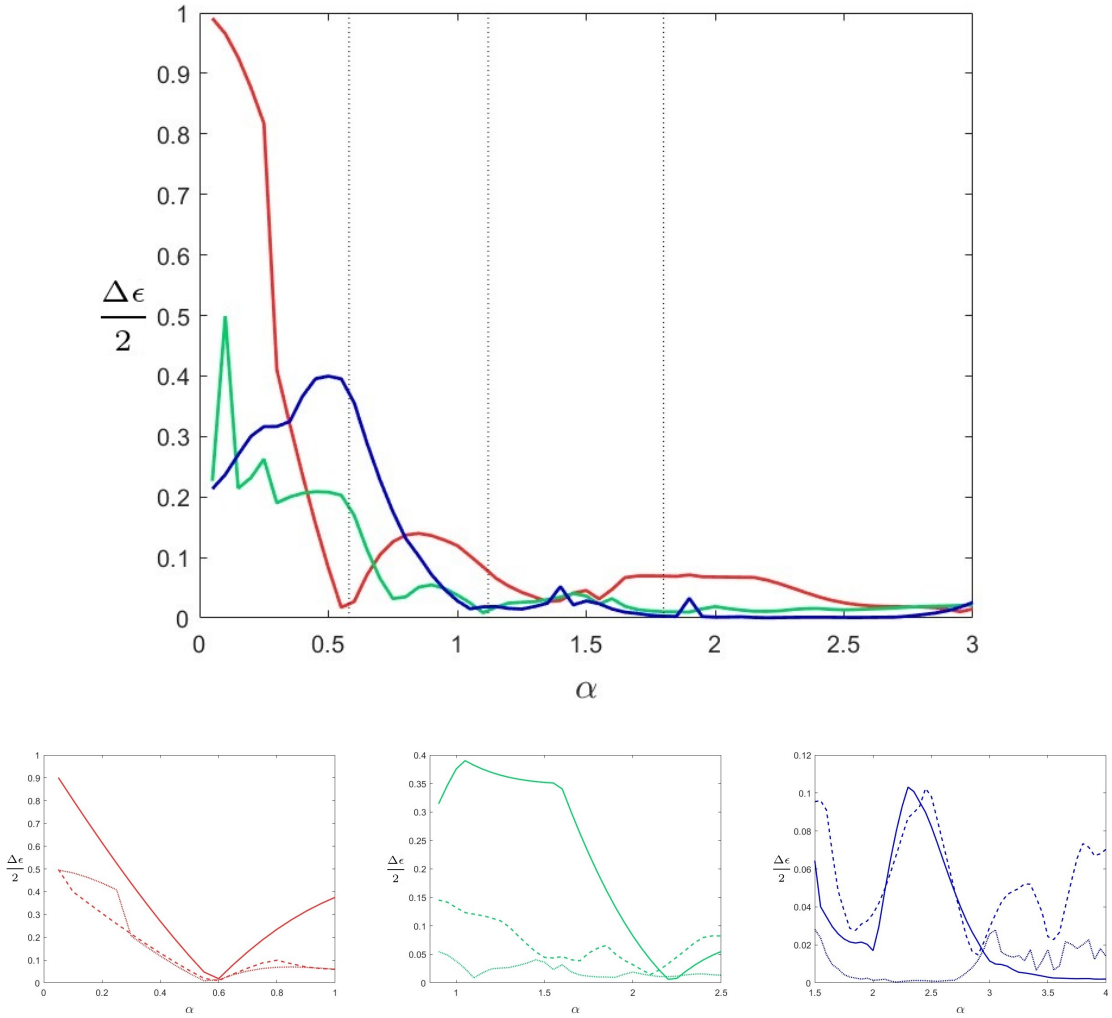

Figure 3.6: Periodicity of the magic angles.
top: The flattening of band gap $\Delta\epsilon$ of the corresponding bands. The first, second and third band are color coded with red, green and blue, respectively. *bottom:* Band gap $\Delta\epsilon$ calculated for $\kappa = 0, 0.5, 1$ corresponding to solid, dashed and dotted lines, respectively.

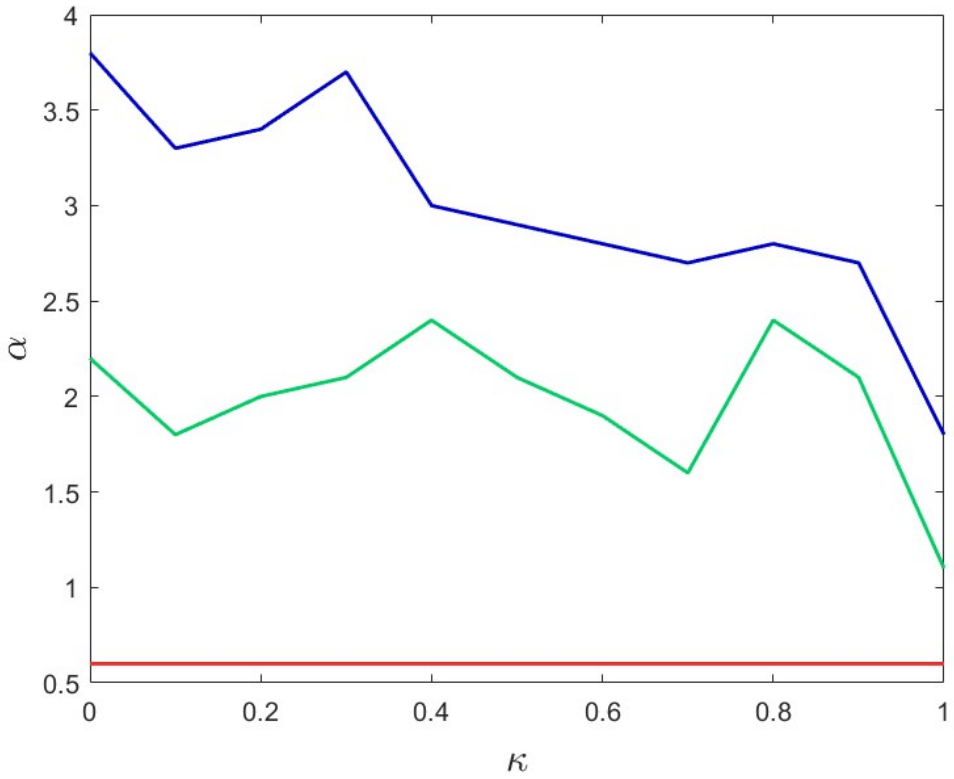

Figure 3.7: Magic angles in dependence of κ.
Magic angles for the first, second and third band using red, green and blue, respectively. These correspond to the first three magic angles in twisted bilayer graphene.

3.8 Summary

In this chapter, the influence of the moiré superlattice to electronic properties of twisted bilayer graphene was discussed. The base for that was to formulate a Dirac continuum theory like R. Bistritzer and A.H. MacDonald [9]. This continuum theory is valid for incommensurate and commensurate bilayers. This advance allows to employ Bloch theory in a quasiperiodic system without true crystal periodicity. The emergent periodicity is linked to the moiré interference pattern present even in the incommensurate case.

For values of $\theta \sim 2 - 10^\circ$ the main effect is a downwards renormalization of the Fermi velocity since van Hove singularities move towards the Dirac point. In the regime $0 < \theta \lesssim 2^\circ$ the layers are strongly coupled also at low-energy scales. In that case, interactions can become important since near certain so-called magic angles, one finds flat bands locked to zero energy. Here, the magic angles in general depend on the different couplings between the individual graphene layers. However, the first magic angle seems to be nearly robust against variation of two different coupling strengths. The magic angles of higher order sensitively shift for different values of κ, which corresponds to the ratio of the couplings w_0 and w_1.

Chapter 4

Mass superlattice

In the following chapter we study two-dimensional Dirac fermions in a mass superlattice $M(x)$, where $M(x)$ alternates between positive and negative mass and is assumed to be homogeneous along y-direction. The chapter is based on the work of De Martino, Dell'Anna, Handt, Miserocchi and Egger [50]. We show that the model in our case will be exactly solvable and nevertheless won´t loose fundamental physical properties.
In fact, we can find the typical highly anisotropic Dirac dispersion, see section 4.4 and 4.7. Furthermore, section 4.4 provides an analytical result for the renormalized velocity and section 4.3 reveals different types of boundary modes.

4.1 Model

In the following part, noninteracting electrons will be described by a two-dimensional Dirac Hamiltonian with a single Dirac cone. In particular, one can consider the two-dimensional Dirac Hamiltonian for single valley graphene, with periodic, piece-wise constant mass term, alternating between $+M$ to $-M$ in a period $d = 2l$ in the x-direction and with translational invariance in the y-direction. Furthermore, the model is also valid for the description of topological insulator physics. Assuming $\hbar = 1$ and setting the Fermi velocity $v_F = 1$ the Hamiltonian reads

$$H = -i\sigma_x\partial_x - i\sigma_y\partial_y + M(x)\sigma_z + V(x)\mathbb{1}. \tag{4.1}$$

This model is valid for an infinitely extended system in the xy-plane with the electrostatic potential $V(x)$ and the mass term $M(x)$, which are homogeneous along the y-direction. Furthermore, the momentum k_y is conserved. Here, the mass term can be

understood as a spatially periodic term which alternates between positive and negative values

$$M(x) = \begin{cases} +M & x \in [2nl,(2n+1)l], \\ -M & x \in [(2n+1)l,(2n+2)l], \end{cases} \qquad n \in \mathbb{Z} \tag{4.2}$$

Writing the wavefunction of equation (4.1) as

$$\Psi(x,y) = e^{ik_y y}\,\psi(x), \quad \psi(x) = \begin{pmatrix} u(x) \\ v(x) \end{pmatrix}, \tag{4.3}$$

the 1D Dirac equation for $\Psi(x)$ reads

$$\begin{pmatrix} M(x)+V(x) & -i(\partial_x + k_y) \\ -i(\partial_x - k_y) & -M(x)+V(x) \end{pmatrix} \begin{pmatrix} u \\ v \end{pmatrix} = E \begin{pmatrix} u \\ v \end{pmatrix}. \tag{4.4}$$

Firstly one assumes that the potential is uniform, V (x) = V. The uniform scalar potential can be restored by a simple shift $E \to E - V$. Solving for a constant $M(x) = M$ one gets

$$\begin{pmatrix} u \\ v \end{pmatrix} = a \begin{pmatrix} 1 \\ \frac{-i\kappa+ik_y}{M+E} \end{pmatrix} \exp(\kappa x) + b \begin{pmatrix} 1 \\ \frac{-i\kappa+ik_y}{M+E} \end{pmatrix} \exp(-\kappa x), \tag{4.5}$$

where a and b are complex coefficients. Notice that if $E^2 < M^2$, κ is real for all k_y and it never vanishes. If $E^2 > M^2$ and $k_y^2 < E^2 - M^2$, κ becomes imaginary. In this case, one can define $\kappa = ik$ to get the general expression

$$\kappa = \begin{cases} \sqrt{M^2 + k_y^2 - E^2}, & E^2 < k_y^2 + M^2, \\ ik \equiv i\sqrt{E^2 - M^2 - k_y^2}, & E^2 > k_y^2 + M^2. \end{cases} \tag{4.6}$$

The unnormalized wave function can be written as

$$\psi(x) = W_M(x) \begin{pmatrix} a \\ b \end{pmatrix} \tag{4.7}$$

with

$$W_M(x) = \begin{pmatrix} e^{\kappa x} & e^{-\kappa x} \\ i\frac{k_y-\kappa}{M+E}e^{\kappa x} & i\frac{k_y+\kappa}{M+E}e^{-\kappa x} \end{pmatrix}, \quad W_M^{-1}(x) = \frac{1}{2\kappa} \begin{pmatrix} (k_y+\kappa)e^{-\kappa x} & i(M+E)e^{-\kappa x} \\ -(k_y-\kappa)e^{\kappa x} & -i(M+E)e^{\kappa x} \end{pmatrix}. \tag{4.8}$$

This reveals spatially localized eigenstates on the length scale κ^{-1} near boundaries for low energies. For $E^2 > k_y^2 + M^2$, κ is purely imaginary. Therefore one finds plane-wave solutions propagating along the x-direction with wave number $k_x = k$. Note that the determinant of $W_M(x)$ in equation (4.8) is independent of x

$$\det W_M(x) = \frac{2i\kappa}{M+E}. \tag{4.9}$$

It is interesting to observe that

$$W_M^\dagger(x)\,\sigma_x\,W_M(x) = \begin{cases} -\frac{2\kappa}{E+M}\sigma_y, & E^2 < k_y^2 + M^2, \\ \frac{2k}{E+M}\sigma_z, & E^2 > k_y^2 + M^2. \end{cases} \tag{4.10}$$

This implies that the x-component of the current density is uniform:

$$j_x = \psi^\dagger \sigma_x \psi = \begin{cases} \frac{4\kappa \mathrm{Im}(b^* a)}{M+E}, & E^2 < k_y^2 + M^2, \\ \frac{2k(|a|^2 - |b|^2)}{M+E}, & E^2 > k_y^2 + M^2. \end{cases} \tag{4.11}$$

In the second illustration the mass term is assumed to be a single kink

$$M(x) = M\,\mathrm{sgn}(x) \quad \text{with} \quad M > 0. \tag{4.12}$$

The wave function then writes

$$\psi(x) = \begin{cases} W_{-M}(x) \begin{pmatrix} a_L \\ 0 \end{pmatrix} & \text{for } x < 0, \\ W_M(x) \begin{pmatrix} 0 \\ b_R \end{pmatrix} & \text{for } x > 0, \end{cases} \tag{4.13}$$

where κ is real and positive, such that the low-energy case of equation (4.6) is required. Also the normalizability requirement is fulfilled by setting $b_L = 0$ and $a_R = 0$. The continuity condition at $x = 0$ gives

$$\begin{pmatrix} 0 \\ b_R \end{pmatrix} = \Omega_S \begin{pmatrix} a_L \\ 0 \end{pmatrix}, \tag{4.14}$$

with

$$\Omega_S = W_M^{-1}(0)\,W_{-M}(0) = \frac{1}{\kappa(E-M)} \begin{pmatrix} E\kappa - k_y M & -(\kappa + k_y)M \\ (-\kappa + k_y)M & E\kappa + k_y M \end{pmatrix}. \tag{4.15}$$

This leads to

$$0 = (E\kappa - k_y M) a_L, \tag{4.16}$$

$$b_R = \frac{(-\kappa + k_y)M}{\kappa(E-M)} a_L. \tag{4.17}$$

Equation (4.16) determines the dispersion relation $E(k_y)$ for the propagating zero-mode localized at the kink:

$$E\sqrt{M^2 + k_y^2 - E^2} - k_y M = 0, \tag{4.18}$$

whose solution is $E = k_y$. This describes a 1D chiral mode propagating along the positive y-direction with velocity v_F. For the trivial case, $k_y = 0$, it is the usual zero-energy solution. There is a second solution, $E = sign(k_y)M$, but this is not acceptable. Equation (4.17) then implies

$$b_R = a_L. \tag{4.19}$$

Finally, the normalization condition fixes a_L. In the case of an anti-kink, $M(x) = -Msign(x)$, one just needs to replace M with $-M$ and one finds the dispersion $E = -k_y$ descibing a mode propagating in opposite direction.
The next step is to look at a single mass barrier of width l:

$$M(x) = \begin{cases} M & \text{for } |x| < l/2, \\ -M & \text{for } |x| > l/2. \end{cases} \tag{4.20}$$

Here again the focus is on localized solutions and κ is assumed to be real and positive, i.e., $E^2 < M^2 + k_y^2$. The wave function can be written as

$$\psi(x) = \begin{cases} W_{-M}(x) \begin{pmatrix} a_L \\ 0 \end{pmatrix} & \text{for } x < -\ell/2, \\ W_M(x) \begin{pmatrix} a \\ b \end{pmatrix} & \text{for } |x| < \ell/2, \\ W_{-M}(x) \begin{pmatrix} 0 \\ b_R \end{pmatrix} & \text{for } x > \ell/2, \end{cases} \tag{4.21}$$

where the requirement of normalizability is already taken into account. Imposing the continuity at $x = \pm l/2$ one again finds analogously to (4.22)

$$\begin{pmatrix} 0 \\ b_R \end{pmatrix} = \Omega_B \begin{pmatrix} a_L \\ 0 \end{pmatrix}, \tag{4.22}$$

with

$$\Omega_B = W_{-M}^{-1}(\ell/2)\, W_M(\ell/2)\, W_M^{-1}(-\ell/2)\, W_{-M}(-\ell/2), \tag{4.23}$$

where

$$[\Omega_B]_{11} = \frac{1}{\kappa^2(E^2 - M^2)}(E^2 - M^2)[k_y^2 - E^2 + M^2 e^{-2\kappa l}], \tag{4.24}$$

$$[\Omega_B]_{12} = \frac{1}{\kappa^2(E^2 - M^2)} \quad - 2M(\kappa + k_y)(E\kappa + k_y M)\sinh(\kappa l), \tag{4.25}$$

$$[\Omega_B]_{21} = \frac{1}{\kappa^2(E^2 - M^2)} 2M(\kappa - k_y)(E\kappa - k_y M)\sinh(\kappa l), \tag{4.26}$$

$$[\Omega_B]_{22} = \frac{1}{\kappa^2(E^2 - M^2)}(E^2 - M^2)[k_y^2 - E^2 + M^2 e^{2l\kappa}]. \tag{4.27}$$

Therefore, the dispersion relation of the localized modes is obtained by solving the equation

$$k_y^2 - E^2 + M^2 \cdot \exp\left(-2\kappa l\right) = 0. \tag{4.28}$$

For $l \to \infty$, one can neglect the exponential term and obtain

$$E = \pm k_y, \tag{4.29}$$

which are the dispersion relations of the two counterpropagating chiral modes localized at the edges of the barrier when they are very far apart. For large but finite l, the two modes hybridize, the dispersions acquire an exponentially small correction, and the crossing at $k_y = 0$ is replaced by an avoided crossing. To see this explicitly, one first focuses on $k_y = 0$ and finds the equation

$$E^2 = M^2 \cdot \exp\left(-2l\sqrt{M^2 - E^2}\right), \tag{4.30}$$

which, in the limit of large l, has the two solutions

$$E \approx \pm M \cdot \exp\left(-lM\right). \tag{4.31}$$

For small energies E and $|k_y|$,$|E| \ll M$ one finds an exponentially small gap

$$E_\pm(k_y) \approx \pm\sqrt{k_y^2 + M^2 e^{-2M\ell}}. \tag{4.32}$$

In this limit, the group velocities are given by

$$v_y \approx \pm \frac{k_y}{\sqrt{k_y^2 + M^2 e^{-2M\ell}}}. \tag{4.33}$$

4.2 Periodic structure

In this section, the periodic case for the mass term is shown. Two main requirements are necessary here. Firstly, the regions of positive and negative mass are assumed to be of the same spatial extent $l \equiv d/2$. Secondly, these regions have to be from the same absolute value $|M(x)| = M$. Overall this implies the symmetry $M(x + \ell) = -M(x)$. By use of the transfer matrix technique one arrives at the quantization condition. Here, the piece-wise constant periodic mass term (4.2) is rewritten in the form

$$M(x) = \begin{cases} +M, & nd \leq x < (n + \frac{1}{2})d, \\ -M, & (n + \frac{1}{2})d \leq x < (n + 1)d, \end{cases} \tag{4.34}$$

where d labels the lattice period and j the unit cell. Since one focuses on one unit cell, it is convenient to restrict calculations to the first unit cell $n = 0$ for simpler notation. The mass profile (4.34) is illustrated in Figure 4.1.

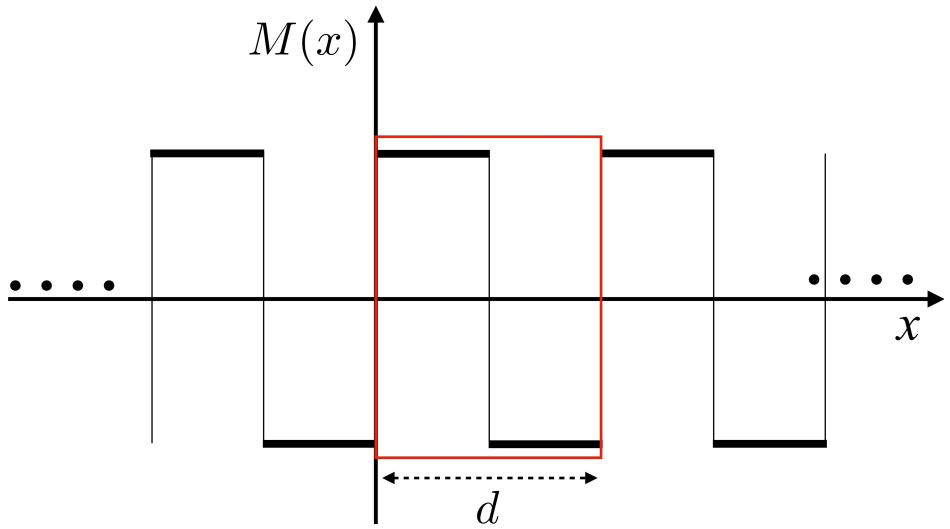

Figure 4.1: Periodic mass profile $M(x)$ of equation (4.34). Adapted from [50].

For $n = 0$ and with equation (4.7) the wave function takes the form

$$\psi(x) = \begin{cases} W_M(x) \begin{pmatrix} a_1 \\ b_1 \end{pmatrix} & \text{for } 0 < x < \ell, \\ W_{-M}(x) \begin{pmatrix} a_2 \\ b_2 \end{pmatrix} & \text{for } \ell < x < d. \end{cases} \tag{4.35}$$

If one imposes the continuity condition at $x = l$ this relates the coefficients (a_2,b_2) and (a_1,b_1)

$$W_M(l) \begin{pmatrix} a_1 \\ b_1 \end{pmatrix} = W_{-M}(l) \begin{pmatrix} a_2 \\ b2 \end{pmatrix}, \tag{4.36}$$

from which one finds

$$\begin{aligned} \begin{pmatrix} a_2 \\ b_2 \end{pmatrix} &= W_{-M}^{-1}(\ell)\, W_M(\ell) \begin{pmatrix} a_1 \\ b_1 \end{pmatrix} \\ &= \frac{1}{\kappa(E+M)} \begin{pmatrix} E\kappa + Mk_y & e^{-2\kappa l}(\kappa + k_y)M \\ e^{2\kappa l}(\kappa - k_y)M & E\kappa - Mk_y \end{pmatrix} \begin{pmatrix} a_1 \\ b_1 \end{pmatrix}. \end{aligned} \tag{4.37}$$

The transfer matrix across the unit cell $0 < x < d$ is then defined by the connection of $\Psi(0)$ and $\Psi(d)$

$$\psi(d) = T\psi(0), \tag{4.38}$$

where

$$T = W_{-M}(d)\, W_{-M}^{-1}(\ell)\, W_M(\ell)\, W_M^{-1}(0). \tag{4.39}$$

The transfer matrix elements are explicitly given by

$$T_{11} = \frac{M^2 + (k_y^2 - E^2)\cosh(\kappa d)}{\kappa^2} + \frac{ME[\cosh(\kappa d) - 1] + k_y \kappa \sinh(\kappa d)}{\kappa^2},$$

$$T_{12} = T_{21} = i\,\frac{E\kappa \sinh(\kappa d) + Mk_y(\cosh(\kappa d) - 1)}{\kappa^2}, \tag{4.40}$$

$$T_{22} = \frac{M^2 + (k_y^2 - E^2)\cosh(\kappa d)}{\kappa^2} - \frac{ME[\cosh(\kappa d) - 1] + k_y \kappa \sinh(\kappa d)}{\kappa^2}.$$

There are two important properties of the matrix (4.39). One can identify the symmetric structure in (4.40). Furthermore, one finds det $T = 1$ and the eigenvalues of T are reciprocal to each other and they can be parametrized as $\lambda_\pm = \exp(\pm iKd)$.
In this sense it is useful to work with the matrix Ω defined by

$$T = W_M(0)\,\Omega\,W_M^{-1}(0). \tag{4.41}$$

Replacing

$$\psi(0) = W_M(0)\begin{pmatrix} a_1 \\ b_1 \end{pmatrix} \quad \text{and} \quad \psi(d) = W_{-M}(d)\begin{pmatrix} a_2 \\ b_2 \end{pmatrix} \tag{4.42}$$

and using relation (4.37) one writes

$$\Omega = W_M^{-1}(0)\,W_{-M}(d)\,W_{-M}^{-1}(l)\,W_M(l). \tag{4.43}$$

The matrix elements are defined by

$$\Omega_{11} = \frac{M^2 + (k_y^2 - E^2)e^{\kappa d}}{\kappa^2},$$

$$\Omega_{12} = \frac{M(1 - e^{-\kappa d})(\kappa + k_y)(E\kappa - Mk_y)}{\kappa^2(E^2 - M^2)},$$

$$\Omega_{21} = \frac{M(1 - e^{-\kappa d})(\kappa - k_y)(E\kappa + Mk_y)}{\kappa^2(E^2 - M^2)},$$

$$\Omega_{22} = \frac{M^2 + (k_y^2 - E^2)e^{-\kappa d}}{\kappa^2}.$$

The matrix (4.43) provides quite similar properties like the transfer matrix above. Ω is real when assuming real κ. Again it is det $\Omega = 1$. Therefore, the eigenvalues of Ω are reciprocal to each other. Since Tr Ω = Tr T , the eigenvalues of Ω are the same as the eigenvalues of T , $\lambda_\pm = \exp(\pm iKd)$. Moreover, Ω_{12} vanishes for $E = k_y$ and Ω_{21} vanishes for $E = -k_y$ which results in

$$\lambda\,(E = k_y) = \begin{pmatrix} 1 & 0 \\ \frac{2E(\exp(Md)-1)}{E+M} & 1 \end{pmatrix}, \quad \lambda\,(E = -k_y) = \begin{pmatrix} 1 & \frac{2E(\exp(-Md)-1)}{E+M} \\ 0 & 1 \end{pmatrix}. \tag{4.44}$$

At this point, different boundary conditions can be imposed. In this section, the focus is on periodic solutions, hence one requires that ψ satisfies the Bloch condition

$$\psi(x+d) = e^{iKd}\,\psi(x), \tag{4.45}$$

where the quasi momentum K runs in the 1D Brillouin zone $-\pi/d < K \leq \pi/d$. Other solutions can be obtained by imposing the condition

$$\psi(x+d) = e^{\mp\mathcal{K}d}\,\psi(x) \tag{4.46}$$

or the condition

$$\psi(x+d) = -e^{\pm\mathcal{K}d}\,\psi(x), \tag{4.47}$$

with $\mathcal{K} > 0$. These describe evanescent waves and exist in systems with boundaries or non-constant potential. In general, one can write equation (4.45) for general complex K. Using (4.51) below and the fact that Tr Ω is real, one can show that there are three possible types of solutions. The first type of solution given by real K corresponds to Bloch waves and as second possibility, K can be complex which corresponds to evanescent state solutions, with $K = \pm i\mathcal{K}$ or $K = \mp i\mathcal{K} \pm \pi/d$. Evanescent waves following from (4.46) are called type I states and type II states derive from (4.47). Setting $x = 0$ and using the transfer matrix, the condition (4.45) can be rewritten as

$$W_M(0)\,\Omega\,W_M^{-1}(0)\,\psi(0) = e^{iKd}\psi(0), \tag{4.48}$$

which is equivalent to

$$\left(\Omega - e^{iKd}\mathbb{1}\right)\begin{pmatrix} a_1 \\ b_1 \end{pmatrix} = \begin{pmatrix} 0 \\ 0 \end{pmatrix}. \tag{4.49}$$

Then a non-trivial solution exists provided

$$\det\left(\Omega - e^{iKd}\mathbb{1}\right) = 0. \tag{4.50}$$

The compatibility condition (4.50) is equivalent to

$$\text{Tr }\Omega = 2\cos(Kd), \tag{4.51}$$

which gives the spectral equation

$$\cos(Kd) = \frac{M^2 + \left(k_y^2 - E^2\right)\cosh\left(d\sqrt{M^2 + k_y^2 - E^2}\right)}{M^2 + k_y^2 - E^2}. \tag{4.52}$$

Here, it will be useful to define a dimensionless parameter

$$\xi = (k_y^2 - E^2)d^2 \tag{4.53}$$

with Tr $\Omega(\xi) = 2f(\xi)$, such that one can write

$$f(\xi) = \cos(Kd) \tag{4.54}$$

with equation (4.51) and finally (4.52) gives

$$f(\xi) = \frac{(Md)^2 + \xi \cosh\left(\sqrt{(Md)^2 + \xi}\right)}{(Md)^2 + \xi}. \tag{4.55}$$

For $k_y = 0$, equation (4.55) coincides with the result obtained in [26] for the generalized Kronig-Penney model, as introduced in chapter 2.3, for a diatomic crystal

$$H = -\partial_x^2 + \sum_{i=1}^{2} \nu_i \sum_n \delta\left(x - R_i - 2nl\right) \tag{4.56}$$

and one finds a spectral equation with $B = \sqrt{M^2 - E^2}$ following [26]

$$\cos\left(2lK\right) = \cosh\left(2Bl\right) - \frac{2M^2}{B^2} \sinh^2\left(Bl\right). \tag{4.57}$$

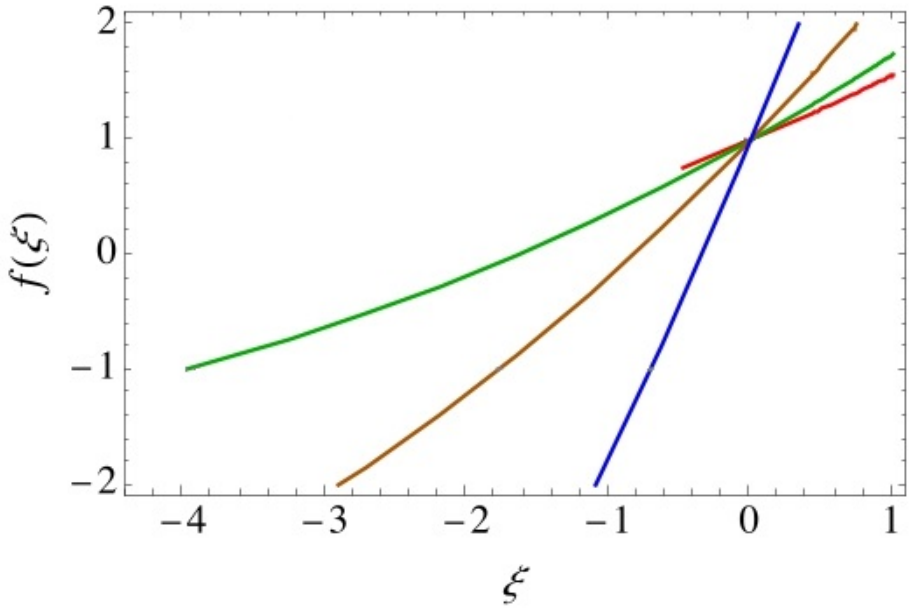

Figure 4.2: The function $f\left(\xi\right)$ of equation (4.55). Adapted from [50].
$f\left(\xi\right)$ is shown for various values of Md. $Md = 0.7$ corresponds to the red curve, while $Md = 2$ is shown by the green one. $Md = 3.5$ and $Md = 5$ then are illustrated in brown and blue, respectively.

Note that in the (E, k_y) region where the absolute value of the left-hand side of equation (4.52) exceeds one, there is no real solution for K. Due to this Bloch states are limited to $-1 \leq f(\xi) \leq 1$. Defining a critical point $\xi_c < 0$ via $f(\xi_c) = -1$ implies $\xi_c \leq \xi \leq 0$ for the above region. In the regions where no Bloch states exist, equation (4.54) is solved by complex valued quasi momenta. One can instead construct evanescent wave functions with imaginary $K = i\mathcal{K}$, or complex $K = i\mathcal{K} + \pi$ with $\mathcal{K} > 0$, which won't be periodic along x, but still yield solutions of the Dirac equation (4.4). They satisfy the boundary

conditions in the equations (4.46) and (4.47). For $\xi > 0$, type I evanescent states can be obtained. Type II evanescent states occur for $\xi < \xi_c$. In the low-energy regime $|E| < M$ type II solutions only exist for $Md > 2$, because in contrast to the $Md < 2$ case here the Fermi surface evolves from a closed curve into a pair of disconnected arcs. For an illustration of the critical point and behavior of equation (4.54) see Figure 4.2.

4.3 Boundary modes

In this part, a brief description of evanescent solutions is given. These evanescent states can arise in the presence of boundaries or nonuniform potentials and follow with a complex valued quasi-momentum K. In this section again the low-energy regime $|E| < M$ is considered with real-valued κ in equation (4.6) and $(Md)^2 + \xi > 0$ referring equation (4.55) is valid.
For given energy E and momentum k_y, the solution of the spectral equation (4.52) gives

$$Kd = \pm \arccos f(\xi). \tag{4.58}$$

This is plotted in Figure 4.3 as a function of k_y for two different values of E and briefly discussed in the following.

For small but non-zero and positive ξ one finds

$$\mathcal{K}d \simeq \frac{\sinh(Md/2)}{Md/2}\sqrt{\xi}, \tag{4.59}$$

which is interesting for later purpose and fits to the calculations for small energies, see (4.86) and (4.87). Evanescent states arise in the regions corresponding to $|f(\xi)| > 1$. From equation (4.52) one sees that if $f(\xi)$ exceeds 1, K must become imaginary, $K = i\mathcal{K}$ with always positive $\mathcal{K}$. Then the corresponding wave function of type I states will take the form (4.35) with

$$\frac{b_1(K = \pm i\mathcal{K})}{a_1} = \frac{e^{\mp \mathcal{K}d} - \Omega_{11}}{\Omega_{12}} \tag{4.60}$$

by using the relation (4.49) and the matrix elements of (4.43). For $K = i\mathcal{K}$ the wave function decays, for $K = -i\mathcal{K}$ there is a rising wave function. Interestingly, since a_1 and b_1 are real for real κ, the x-component of the current density vanishes.
If $f(\xi)$ decreases below -1, then K must become complex, $K = i\mathcal{K} + \pi/d$. The corresponding wave function will take the form (4.35) with

$$\frac{b_1(K = \mp i\mathcal{K} \pm \pi/d)}{a_1} = \frac{-e^{\pm \mathcal{K}d} - \Omega_{11}}{\Omega_{12}}. \tag{4.61}$$

As illustrated in the Figure 4.3 there exists a region for small $|k_y|$ and $Md > 2$ where a pair of type-II states with $K = \mp i\mathcal{K} \pm \pi/d$ is present.

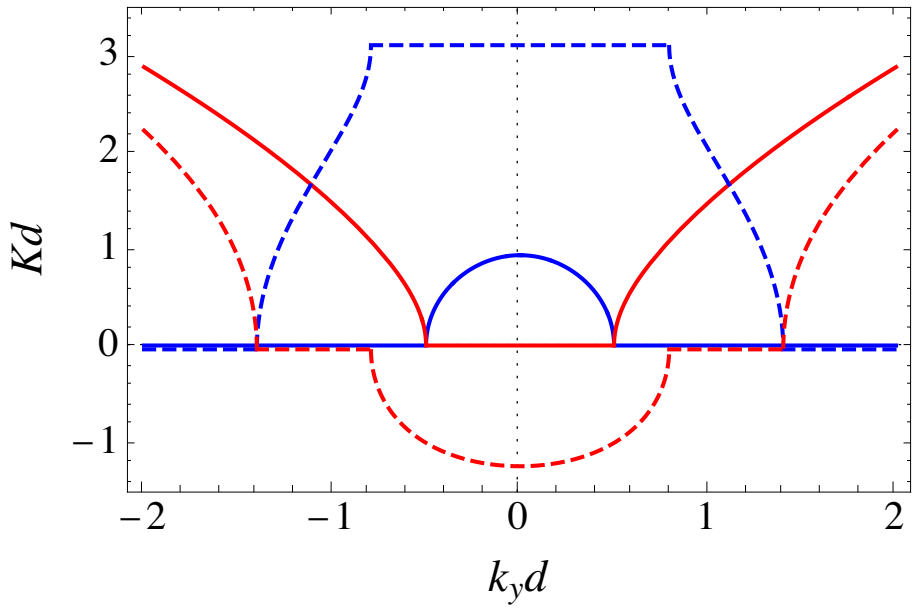

Figure 4.3: Quasi-momentum (4.58). Figure from [50].
K vs k_y for $Md = 4$ and the + sign in equation (4.58). The red curves illustrate the imaginary part of K, while the blue shows the real part. *solid lines:* For $|k_y| > |E|$ the real part is zero and K becomes imaginary. Here $Ed = 0.5$. This is when Tr $\Omega(E, k_y) > 2$. *dashed lines:* For $Ed = 1.4$, the real part is zero for $|k_y| > |E|$. There is a range of k_y around zero where K becomes complex. This is when Tr $\Omega(E, k_y) < -2$.

Equation (4.58) is plotted in Figure 4.3 as a function of k_y for two different values of E. From the figure it is obvious that, if one uses the equation (4.58), then when K is purely imaginary, its imaginary part is positive. When it is complex, its imaginary part is negative. It is important to keep this in mind when using (4.58) to calculate K. For $E^2 < M^2$, the evanescent states have two length scales. Locally, they decay and grow over the characteristic length κ^{-1}, which is a "microscopic" length that decreases for increasing k_y. On scales larger than d they decay or grow with the larger characteristic length $\mathcal{K}^{-1}$, that increases for increasing k_y.
For the calculation of the spectrum for boundary states a system that extends in the half-plane $x < x_0$ with $0 < x_0 < l$ is considered. Here, no potential step $V(x) = 0$ is required. Setting the usual boundary condition for the Dirac equation at position $x = x_0$, i.e., requiring that the component of the current density normal to the boundary vanishes, one finds

$$\mathcal{M}(\alpha)\Psi(x_0,y) = \pm\Psi(x_0,y), \tag{4.62}$$

where

$$\mathcal{M}(\alpha) = \sigma_y \cos(\alpha) + \sigma_z \sin(\alpha). \tag{4.63}$$

α is an angle that parametrizes the boundary condition. For definiteness, one can choose the eigenvalue + in equation (4.62). The other case is obtained by replacing $\alpha \to \alpha + \pi$. $|\alpha, +\rangle$ denotes the eigenstate of $M(\alpha)$ with eigenvalue +1:

$$|\alpha, +\rangle = \begin{pmatrix} \cos\left(\frac{\alpha}{2} - \frac{\pi}{4}\right) \\ -i \sin\left(\frac{\alpha}{2} + \frac{\pi}{4}\right) \end{pmatrix}, \tag{4.64}$$

$$|\alpha, -\rangle = \begin{pmatrix} \sin\left(\frac{\alpha}{2} - \frac{\pi}{4}\right) \\ i \cos\left(\frac{\alpha}{2} + \frac{\pi}{4}\right) \end{pmatrix}. \tag{4.65}$$

The range of k_y and E is assumed such that $|\,\mathrm{Tr}\ \Omega| > 2$. Therefore, the imaginary part of $Kd = \pm \arccos(\mathrm{Tr}\ \Omega/2)$ is finite and here only the wave function corresponding to an evanescent wave that decays for $x \to -\infty$ is taken. This wave function will be written as $\Psi_K(x)$. For type I states, that exist if $\mathrm{Tr}\ \Omega > 2$, this means that $Kd = -i\ \mathrm{Im}[\arccos(\mathrm{Tr}\ \Omega/2)] = -i\mathcal{K}d$ with $\mathcal{K} > 0$, and $\Psi_K(0)$ satisfies

$$\left(T - \exp\left(\mathcal{K}d\right)\right) \Psi_K(0) = 0. \tag{4.66}$$

For type II states, that exist if $\mathrm{Tr}\ \Omega < -2$, this means that $Kd = \pi + i\ \mathrm{Im}[\arccos(\mathrm{Tr}\ \Omega/2)] = \pi - i\mathcal{K}d$ with $\mathcal{K} > 0$, and $\Psi_K(0)$ satisfies

$$\left(T + \exp\left(\mathcal{K}d\right)\right) \Psi_K(0) = 0. \tag{4.67}$$

Note, that for type I states there is $\mathcal{K} = \mathrm{Im}[\arccos(\mathrm{Tr}\ \Omega/2)] > 0$, while for type II states, $\mathcal{K} = -\mathrm{Im}[\arccos(\mathrm{Tr}\ \Omega/2)] > 0$. It is convenient to write the two equations above as

$$\left(T - \exp\left(Kd\right)\right) \Psi_K(x) = 0. \tag{4.68}$$

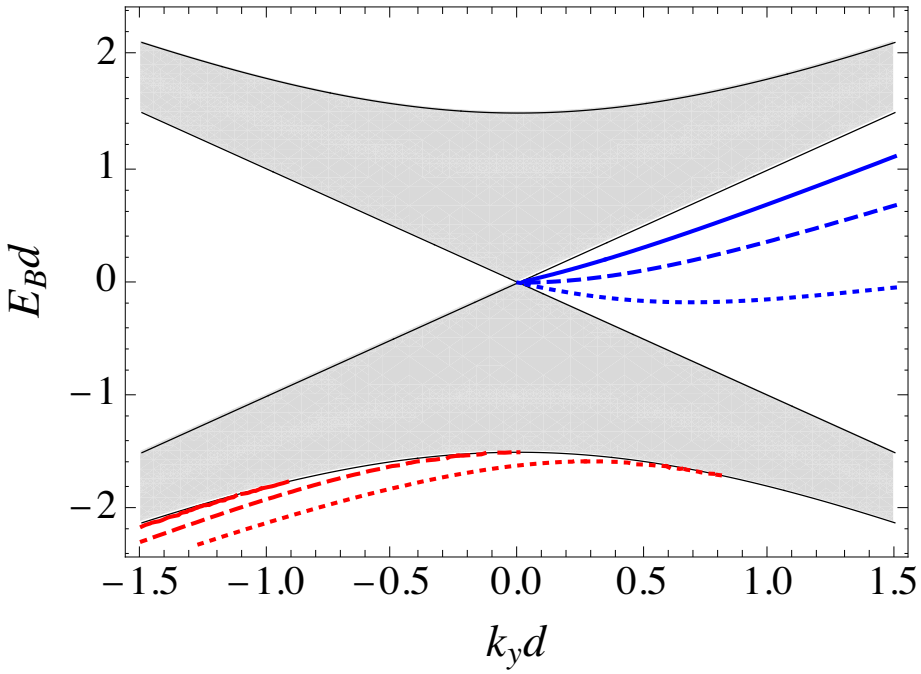

Figure 4.4: Dispersion relation of boundary states. Figure from [50].
Bloch waves exist in the grey region in the limits $\mathrm{Tr}\,\Omega < 2$ and $\mathrm{Tr}\,\Omega > -2$. Here, the boundary angles are $\alpha = \pi/3$ (solid), $\alpha = \pi/2$ (dashed), $\alpha = 2\pi/3$ (dotted) and $x_0 = 0.25\,d$, $Md = 3.1$. *blue:* Spectrum of type I boundary states. *red:* Spectrum of type II boundary states.

Now, imposing the boundary condition, the wavefunction at $x = x_0$ must be the eigenstate $|\alpha,+\rangle$ up to a constant:

$$\Psi_K(x_0) = C|\alpha,+\rangle. \tag{4.69}$$

Since

$$\Psi_k(x_0) = W_M(x_0) W_M^{-1}(0) \Psi_K(0) \tag{4.70}$$

one can find

$$\Psi_k(0) = W_M(0) W_M^{-1}(x_0) \Psi(x_0) = C W_M(0) W_M^{-1}(x_0) |\alpha,+\rangle. \tag{4.71}$$

Imposing the condition

$$(T - \exp(Kd)) \Psi_K(0) = 0 \tag{4.72}$$

this results in

$$(T - \exp(Kd)) W_M(0) W_M^{-1}(x_0) |\alpha,+\rangle = 0. \tag{4.73}$$

This equation determines the spectrum of the boundary states. For the numerics, it is more convenient to use (4.51) and one derives the spectral equation

$$\left(\Omega - e^{iKd}\mathbb{1}\right) W_M^{-1}(x_0)|\alpha\rangle = 0 \tag{4.74}$$

with $K = -i\mathcal{K}$ for type I states and $K = -i\mathcal{K} + \pi/d$ for the type II states.
The Figure 4.4 illustrates the spectrum of boundary states, where the energy is in the range $E^2 < M^2$. For the case $Md = 1.7$ only type I states exist and typical features are shown. The shape of the spectrum depends significantly on the angle α and the boundary location x_0. In addition, the dispersion is not symmetric in k_y. For values with $Md > 2$ both type I and type II states exist and also exhibit the above features. The antisymmetry in k_y then implies a current, which leads to observability in transport experiments.

4.4 Bloch states

In between the grey lines in Figure 4.4 Bloch states arise. To study these states one has to find the solutions of the spectral condition (4.54) for real quasi-momenta K in the 1D Brillouin zone $-\pi/d < K \leq \pi/d$. For numerics it is convenient to introduce the function

$$\tilde{\Phi}(E,K,k_y) = f\left((k_y^2 - E^2)d^2\right) - \cos(Kd). \tag{4.75}$$

The quantization condition $\tilde{\Phi}(E,K,k_y) = 0$ then refers to equation (4.54) and determines the spectrum. In general, one can implicitly find $E(K,k_y)$ from numerics and plot the band structure shown in Figure 4.5.

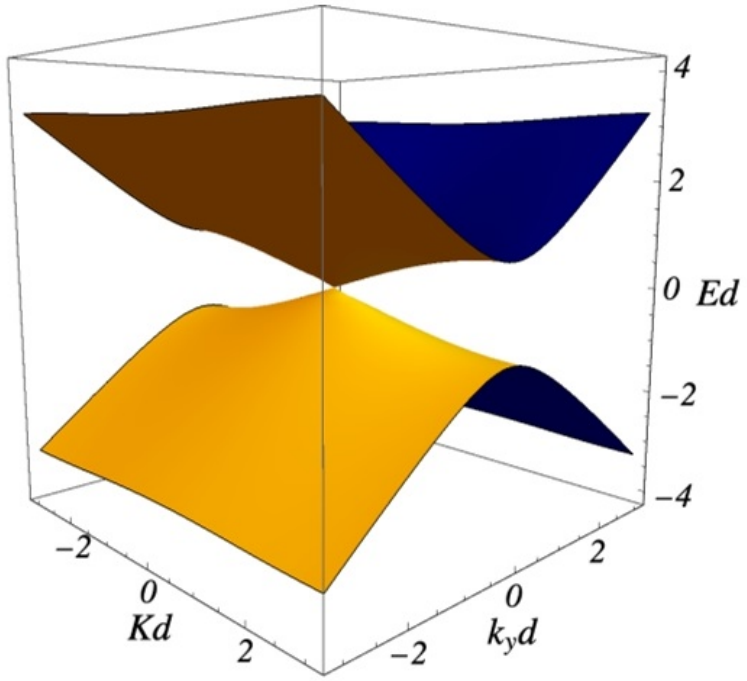

Figure 4.5: Dispersion relation of Bloch states for $Md = 5$. Figure from [50].

In the following, a few cases will be discussed that can be solved analytically. For this purpose E, K and k_y are measured in units of $1/d$ and the spectral equation (4.52) is rewritten with the parameter $\eta = Md$. Then condition (4.75) is analogous to

$$\Phi(E,K,k_y) = \eta^2 + \left(k_y^2 - E^2\right)\cosh\left(\sqrt{\eta^2 + k_y^2 - E^2}\right) - \left(\eta^2 + k_y^2 - E^2\right)\cos(K). \quad (4.76)$$

Equation (4.76) determines a set of particle-hole symmetric bands $E_{n,\pm}(K,k_y)$ with $n \in \mathbb{Z}$. Here, n labels the different bands. The group velocity is given by

$$v_x = -\frac{\partial_K \Phi}{\partial_E \Phi}\bigg|_{E=E_{n,\pm}} = \frac{\kappa^3 \sin(K)}{E\left(2\kappa\left(\cosh(\kappa) - \cos(K)\right) + \left(\kappa^2 - \eta^2\right)\sinh(\kappa)\right)}\bigg|_{E=E_{n,\pm}}, \quad (4.77)$$

$$v_y = -\frac{\partial_{k_y} \Phi}{\partial_E \Phi}\bigg|_{E=E_{n,\pm}} = \frac{k_y}{E}\bigg|_{E=E_{n,\pm}}. \quad (4.78)$$

For the limit of $\eta = Md \to 0$ equations (4.55) and (4.76) yield

$$\cosh\left(\sqrt{k_y^2 - E^2}\right) = \cos(K), \quad (4.79)$$

which gives the usual linear spectrum of the Dirac equation with the x-component of the momentum restricted to the first Brillouin zone:

$$E = \pm E_n(K,k_y) = \pm\sqrt{(K + 2\pi n)^2 + k_y^2}, \quad n \in \mathbb{Z}, \quad -\pi < K \leq \pi. \quad (4.80)$$

This band structure features an isolated node and crossing point at $E = 0$ due to $E_{0,+}(0,0) = E_{0,-}(0,0)$. Moreover, there are crossing points for finite energies at $K = 0$, because $E_{n,\pm}(0,k_y) = E_{-n,\pm}(0,k_y)$, and at $K = \pi$, because $E_{n,\pm}(\pi,k_y) = E_{-n-1,\pm}(\pi,k_y)$. But in fact they are not isolated, because they move with k_y. For very large Md the bandwidth in x-direction is strongly suppressed

$$E \approx \pm\sqrt{k_y^2 + 2\eta^2\left(1-\cos(K)\right)\exp(-\eta)}. \tag{4.81}$$

For finite η, at the center of the 1D Brillouin zone, $K = 0$, equation (4.76) gives

$$\left(E^2 - k_y^2\right)\cosh\left(\sqrt{\eta^2 + k_y^2 - E^2}\right) = E^2 - k_y^2, \tag{4.82}$$

whose solutions are

$$E_{0,\pm}\left(0,k_y\right) = \pm k_y \tag{4.83}$$

$$E_{0,\pm}\left(0,k_y\right) = \pm\sqrt{\eta^2 + k_y^2 + (2\pi n)^2}, \quad n = \pm 1, \pm 2, \pm 3, ... \tag{4.84}$$

Note that each $E_{n,\pm}(0,k_y)$ is doubly degenerate, because $E_{n,\pm}(0,k_y) = E_{-n,\pm}(0,k_y)$. The degeneracy is lifted for finite K as shown below. For not too large k_y, the first pair of solutions is inside the mass gap $|E_{0,\pm}(0)| < \eta$, all the others are outside the gap. For $k_y = 0$, the band structure has crossings at $E = 0, \pm\sqrt{\eta^2 + (2\pi n)^2}$. For finite η around $(K,k_y,E) = (0,0,0)$ one can expand and find

$$1 + \frac{\cosh(\eta - 1)}{\eta^2}\left(k_y^2 - E^2\right) = 1 - \frac{1}{2}K^2, \tag{4.85}$$

which gives an anisotropic conical dispersion relation for small energies and small momenta

$$E_{0,\pm}(K,k_y) \approx \pm\sqrt{v_{x,0}^2 K^2 + k_y}. \tag{4.86}$$

Here, the renormalized x-component of the velocity is

$$v_{x,0} = \sqrt{\frac{\eta^2}{2(\cosh(\eta) - 1)}} = \frac{\eta/2}{\sinh(\eta/2)}. \tag{4.87}$$

It is clear that for $\eta \to 0$ the usual linear spectrum with $v_{x,0} = 1$ is recovered.
Similarly, one can expand around the Γ-point $(K,k_y,E) = \left(0,0,\sqrt{\eta^2 + (2\pi n)^2}\right)$ and find

$$E_{n,\pm}(K,k_y) \approx \pm\left(\sqrt{\eta^2 + (2\pi n)^2} + \frac{k_y^2}{2\sqrt{\eta^2 + (2\pi n)^2}}\right) \pm v_{x,n}|K|, \tag{4.88}$$

with

$$v_{x,n} = \frac{(2\pi n)^2}{\eta^2 + (2\pi n)^2}. \tag{4.89}$$

All four combinations of signs in equation (4.88) should be considered. The double degeneracy of each eigenvalue $E_{n,\pm}(0,0)$ is lifted by a finite K. Note that a finite k_y does not lift the degeneracy at $K = 0$, hence there is a nodal line. It is interesting to compare this result with the case of uniform mass $M(x) = M$. Using the transfer matrix approach, one finds the equation

$$\cosh\sqrt{\eta^2 + k_y^2 - E^2} = \cos(K), \tag{4.90}$$

whose solutions are

$$E_{n,\pm}(K,k_y) = \pm\sqrt{\eta^2 + k_y^2 + (2\pi n + K)^2}, \quad n \in \mathbb{Z}, \quad -\pi < K \leq \pi. \tag{4.91}$$

Note that there is no zero energy mode that relates to the anisotropic Dirac cone of equation (4.86).

Expanding around the Γ-point one finds

$$E_{0,\pm}(K,k_y) \approx \pm\left(\eta + \frac{k_y^2 + K^2}{2\eta}\right), \tag{4.92}$$

$$E_{n,\pm}(K,k_y) \approx \pm\left(\sqrt{\eta^2 + (2\pi n)^2} + \frac{k_y^2}{2\sqrt{\eta^2 + (2\pi n)^2}} + sign(n)\tilde{v}_{x,n}K\right) \tag{4.93}$$

with

$$n = \pm 1, \pm 2, \pm 3, \ldots \text{ and } \tilde{v}_{x,n} = \frac{2\pi n}{\sqrt{\eta^2 + (2\pi n)^2}}. \tag{4.94}$$

Remember $E = \pm\sqrt{\eta^2 + (2\pi n)^2}$ is the energy of the crossing points. The main difference with the case of alternating mass is the absence of the zero modes and such a resulting energy shift. Furthermore, a different renormalization of the x-component of the velocity occures.

4.5 Bloch wave function

Now, assume K is real for considering the wave function itself. The wave function can be written as $\Psi(x) = u_K(x)\exp(iKx)$, where $u_K(x)$ is a spinor with the periodicity of the lattice, $u_K(x + d) = u_K(x)$, given by

$$u_K(x) = \begin{cases} \exp(-iKx)W_{E,M}(x)\begin{pmatrix} a_1 \\ b_1 \end{pmatrix}, & 0 < x < l, \\ \exp(-iKx)W_{E,-M}(x)\begin{pmatrix} a_2 \\ b_2 \end{pmatrix}, & l < x < d. \end{cases} \tag{4.95}$$

From equation (4.49) one finds

$$b_1(K) = \frac{\exp(iKd) - \Omega_{11}}{\Omega_{12}} a_1 \tag{4.96}$$

and with equation (4.37) $\begin{pmatrix} a_2 \\ b_2 \end{pmatrix}$ is determined. The coefficient a_1 is fixed by the normalization condition in the unit cell

$$\int_0^d dx \quad |u_K(x)|^2 = 1. \tag{4.97}$$

From equation (4.11) it follows that the x-component of the current density for real κ in the region $0 < x < l$ is given by

$$j_x = \frac{-4\kappa \sin(Kd)}{(M+E)\Omega_{12}} |a_1|^2, \tag{4.98}$$

Note that this expression is odd in K. Since the x-component of the current density must be uniform along x, this expression must be valid in the whole unit cell. Moreover, it seems that j_x is divergent if Ω_{12} vanishes, but this is incorrect, because Ω_{12} vanishes for $k_y \to E$ and in this limit $K \to 0$. For the general scattering problem, instead of condition (4.97) it is more convenient to adopt a normalization such that the wave function carries unit current. This is obtained by setting

$$|a_1|^2 = \left| \frac{(M+E)\Omega_{12}}{-4\kappa \sin(Kd)} \right|, \tag{4.99}$$

The absolute value is needed because the current can be positive or negative. Equation (4.99) fixes a_1 up to an irrelevant phase. Notice that $|a_1(-K)|^2 = |a_1(K)|^2$. It follows that the x-component of the current density can also be expressed as

$$j_x = \frac{2i \sin(Kd)}{T_{12}} |u(0)|^2, \tag{4.100}$$

where $u(0)$ is the upper component of $\Psi(0)$.

4.6 Potential step

In this section the Hamiltonian (4.1) with a mass term following (4.34) in the presence of the potential step at position x_s

$$V(x) = \begin{cases} -V_L & x < x_s \\ \\ V_R & x > x_s \end{cases} \tag{4.101}$$

is studied. Here, the step is located in a region of positive mass, i.e., $0 < x_s < l$. This implies that M is positive both on the left and the right of the step. Furthermore, the step is assumed to be of moderate size with $0 < V_L < M/2$ and $0 < V_R < M/2$. One considers an np junction set-up, with $V_L, V_R > 0$ and focuses on an energy range where only the zero-mode band is involved, i.e., only subgap states. The calculation then restricts to real values of κ, see (4.6). Note, that close enough to $(K, k_y) = (0, 0)$, the zero-mode band dispersion is an anisotropic double cone, see (4.86). To ensure that κ is real for any k_y, one assumes in the right and in the left subsystems

$$|E + V_L|,|E - V_R| < M, \tag{4.102}$$

which is equivalent to

$$-M + V_R < E < M - V_L. \tag{4.103}$$

This is in particular important for values of k_y approaching zero and guarantees that

$$\kappa_L = \sqrt{M^2 + k_y^2 - (E + V_L)^2}, \quad \kappa_R = \sqrt{M^2 + k_y^2 - (E - V_R)^2} \tag{4.104}$$

are always real. In the following, the reflection coefficient at energy E is calculated assuming

$$-V_L < E < V_R. \tag{4.105}$$

This implies that the state at energy E is a particle state on the left and a hole state on the right of the junction. The associated group velocity is then parallel to the momentum on the right and anti-parallel on the left. Note that as long as $V_R + V_L < M$ the condition (4.105) automatically implies (4.103).

4.6.1 Scattering problem

From the band structure it is obvious that there are two Fermi momenta $\pm K_L(E)$ on the left side of the step and two Fermi momenta $\pm K_R(E)$ on the right. The exact values can be determined by the dispersion relation using (4.75):

$$\Phi(E + V_L,K_L,k_y) = 0, \quad \Phi(E - V_R,K_R,k_y) = 0. \tag{4.106}$$

The wave function can be written as

$$\psi_<(x < x_s) = W_{E+V_L,M}(x) \left[\begin{pmatrix} a_1 \\ b_1 \end{pmatrix}_{K_L} + r \begin{pmatrix} a_1 \\ b_1 \end{pmatrix}_{-K_L} \right],$$

$$\psi_>(x > x_s) = t\, W_{E-V_R,M}(x) \begin{pmatrix} a_1 \\ b_1 \end{pmatrix}_{-K_R}, \tag{4.107}$$

where we have reintroduced the energy subscript on the matrix W, r is the reflection amplitude and t the transmission amplitude. In general, these amplitudes are

complex-valued. The normalization of the incident, reflected and transmitted wave functions follow from (4.99). Notice that the wave function $\Psi_>$ is evaluated at $-K_R$, as it describes a hole propagating to the right. The transmission coefficient $\mathcal{T}$ can be expressed as

$$\mathcal{T} = |t|^2 = |c|^2 \left| \frac{a_1(K_L)}{a_1(K_R)} \right|^2, \tag{4.108}$$

where c is calculated from Eq. (4.109) below with all $a_1(\pm K_{L,R})$ set to 1. The continuity condition for the wave function at the step position gives a system of two linear equations

$$\Psi_<(x_s) = \Psi_>(x_s)$$

$$W_{E_L,M}(x_s) \left[\begin{pmatrix} 1 \\ b_1 \end{pmatrix}_{K_L} + r \begin{pmatrix} 1 \\ b_1 \end{pmatrix}_{-K_L} \right] = c W_{E_R,M}(x_s) \begin{pmatrix} 1 \\ b_1 \end{pmatrix}_{-K_R}, \tag{4.109}$$

where $E_L = E + V_L$ and $E_R = E - V_R$ and with (4.43)

$$b_1(\pm K_L) = \frac{e^{\pm i K_L d} - \Omega_{11}(E + V_L)}{\Omega_{12}(E + V_L)}, \tag{4.110}$$

$$b_1(\pm K_R) = \frac{e^{\pm i K_R d} - \Omega_{11}(E - V_R)}{\Omega_{12}(E - V_R)}. \tag{4.111}$$

By solving the system for r, one determines the reflection probability $\mathcal{R} = |r|^2$. It is useful to define

$$\begin{pmatrix} A \\ B \end{pmatrix}_K = W^{-1}_{E_L,M}(x_s)\, W_{E_R,M}(x_s) \begin{pmatrix} 1 \\ b_1 \end{pmatrix}_K. \tag{4.112}$$

The matrix $W^{-1}_{E_L,M}(x_s)\, W_{E_R,M}(x_s)$ is real if κ is real. One then obtains

$$r = -\frac{B(-K_R) - b_1(K_L) A(-K_R)}{B(-K_R) - b_1(-K_L) A(-K_R)}, \tag{4.113}$$

$$c = \frac{b_1(K_L) - b_1(-K_L)}{B(-K_R) - b_1(-K_L) A(-K_R)}.$$

The reflection and transmission probabilities are finally given by

$$\mathcal{R} = \left| \frac{B(-K_R) - b_1(K_L) A(-K_R)}{B(-K_R) - b_1(-K_L) A(-K_R)} \right|^2, \tag{4.114}$$

$$\mathcal{T} = \frac{4\kappa_R \sin(K_R)}{(E_R + M)\,\Omega_{12}(E_R)} \frac{(E_L + M)\,\Omega_{12}(E_L)}{-4\kappa_L \sin(K_L)} \left| \frac{b_1(K_L) - b_1(-K_L)}{B(-K_R) - b_1(-K_L) A(-K_R)} \right|^2. \tag{4.115}$$

Both $\mathcal{R}$ and $\mathcal{T}$ are functions of energy E and momentum k_y. The formulas above are derived under the assumption that at the given value of energy and momentum,

there exists a Bloch wave incident from the left side, i.e., there is a real solution K_L to equation (4.106). Therefore, the range of k_y must be restricted, when plotting $\mathcal{R}$ or $\mathcal{T}$ as function of k_y at given E. The restriction is given by

$$-2 < \text{Tr } \Omega(E + V_L, k_y) < 2, \tag{4.116}$$

or the left side of equation (4.52) is smaller than mod1 by replacing $E \to E + V_L$. This would be equivalent to (4.116). There are no propagating states in the region $x > x_0$, if $|\text{Tr } \Omega(E + V_L, k_y)| < 2$ but $|\text{Tr } \Omega(E - V_R, k_y)| > 2$. Therefore, the states are fully reflected and the reflection coefficient must be 1. Indeed, if K_L is real but $K_R = iK_R$ or $K_R = iK_R + \pi/d$, then equation (4.114) gives $\mathcal{R} = 1$. In this case, the formula for the transmission (4.115) should not be used, but instead $\mathcal{T} = 0$. Explicitly, one finds that the two inequalities (4.116) can be casted into the following form:

$$\text{Tr } \Omega(E + V_L, k_y) < 2 \Leftrightarrow (E + V_L)^2 - k_y^2 > 0, \tag{4.117}$$

$$\text{Tr } \Omega(E + V_L, k_y) > -2 \Leftrightarrow (E + V_L)^2 - k_y^2 < \frac{2M^2}{\cosh\sqrt{M^2 + k_y^2 - (E + V_L)^2} + 1}, \tag{4.118}$$

where $\kappa^2 > 0$ is assumed. From the first condition one sees that there is an upper bound for the allowed k_y^2, such that $k_{y,max} = |E + V_L|$. The second condition is always satisfied for k_y^2 close enough to $(E+V_L)^2$. However, depending on $E+V_L$ and M, there might also be a lower bound on k_y^2 . Indeed, both sides of the inequality are decreasing functions of k_y^2 with a maximum at $k_y = 0$. Then, if the maximum of the left-hand side is larger than the maximum of the right-hand side, there can be a range of k_y^2 around zero in which the inequality is not satisfied. This occurs if M is large enough and $M^2 - (E + V_L)^2$ small enough. The lower bound k_y^2 is then the solution of

$$(E + V_L)^2 - k_y^2 < \frac{2M^2}{\cosh\sqrt{M^2 + k_y^2 - (E + V_L)^2} + 1}, \tag{4.119}$$

which results in

$$(E + V_L)^2 > \frac{2M^2}{\cosh\sqrt{M^2 - (E + V_L)^2} + 1}. \tag{4.120}$$

By exactly looking at the reflection (4.114) and transmission (4.115) one can find strong dependencies to the behaviour by varying the parameters. This is illustrated for the case of equal step size $V_L = V_R = V_s$. Starting with the transmission probability $\mathcal{T}$, Figure 4.6 illustrates that for fixed step position x_s there is a symmetry given by

$$\mathcal{T}(E = 0, -k_y) = \mathcal{T}(E = 0, +k_y). \tag{4.121}$$

Furthermore, there is a wide region around $k_y = 0$ where also $\mathcal{T}$ completely vanishes. The extent in $\pm k_y$ direction seems to be independent of the step size. This region

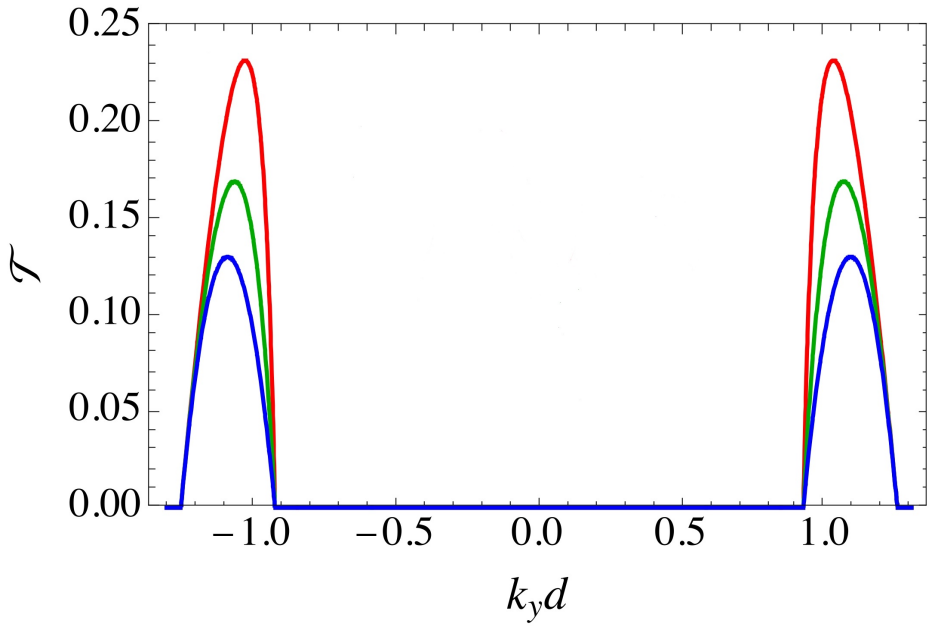

Figure 4.6: Dependency of transmission probability $\mathcal{T}$ on k_y. Figure from [50]. Here the illustration is for fixed $E = 0$, $V_s d = 1.25$ and $Md = 5$ while the step position varies. $x_s/d = 0.05$ corresponds to the red curve. Further $x_s/d = 0.1$ is shown in green and $x_s/d = 0.25$ blue.

shrinks for decreasing Md, for further illustration see [50]. The transmission exhibits peaks near k_{min} and k_{max} where the height strongly depends on the step position for fixed energy. In addition, Figure 4.7 reveals that the transmission probability is high where also the probability density is maximum. Additionally, one finds the symmetry

$$\mathcal{T}\left(\frac{d}{2} - x_s, k_y\right) = \mathcal{T}\left(x_s, -k_y\right). \tag{4.122}$$

4.6.2 Conductance

For calculating the conductance of the potential step system, one can impose periodic boundary conditions in the y-direction, such that $k_y = \frac{2\pi m}{w}$ with $m \in \mathbb{Z}$ labels discrete transverse states. Because of the noninteracting behaviour the conductance can directly be determined from the transmission $\mathcal{T}$ in equation (4.115). According to the

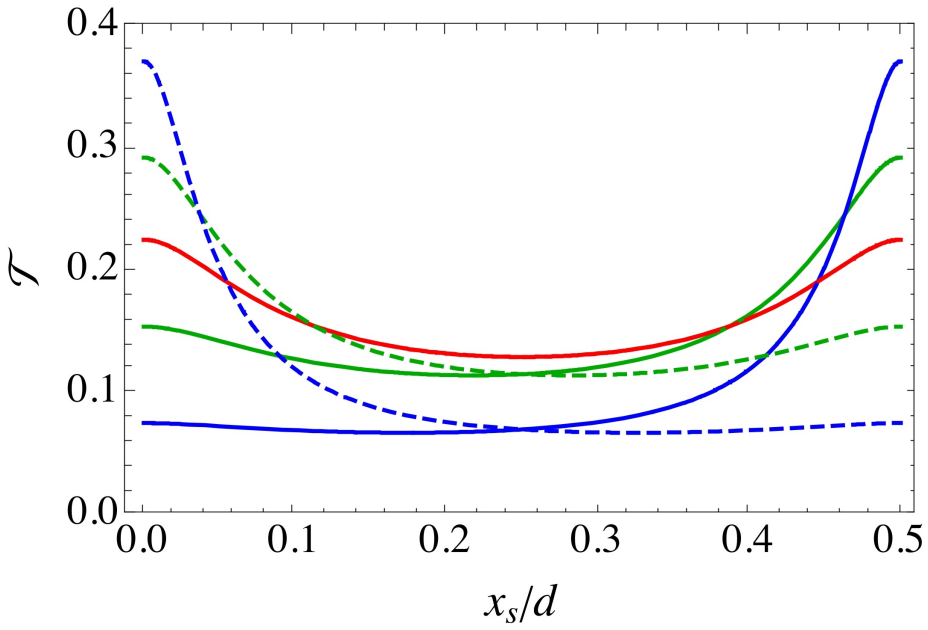

Figure 4.7: Dependency of transmission probability $\mathcal{T}$ on x_s. Figure from [50]. Here the illustration is for fixed $V_s d = 1.25$ and $Md = 5$ while the energy or step position varies. The dashed lines correspond to $k_y d = -1.1$ while the case $k_y d = 1.1$ is illustrated with solid lines. $E = 0$ corresponds to the red curve. Further $E = 0.05$ is shown in green and $E = 0.1$ blue.

Landauer-Büttinger formalism each available transverse state at the Fermi energy at zero temperature contributes $\frac{e^2}{h}\mathcal{T}$ to the linear conductance. Then one finds

$$G(E_F) = \frac{Ne^2}{2\pi\hbar} \sum_{k_y} \mathcal{T}(E_F, k_y) \tag{4.123}$$

$$\approx \frac{Ne^2 w}{(2\pi)^2 \hbar} \int dk_y \quad \mathcal{T}(E_F, k_y), \tag{4.124}$$

with the degeneracy factor N. The integration limits are constructed in the region of k_y such that

$$-2 < |\,\mathrm{Tr}\;\; \Omega(E + V_L, k_y)| < 2, \quad -2 < |\,\mathrm{Tr}\;\; \Omega(E - V_R, k_y)| < 2. \tag{4.125}$$

This formula then gives the conductance of a stripe with width w along the y-direction, where the electrodes are connected at $x \to \infty$. For a system of monolayer graphene the spin and valley degeneracy would provide $N = 4$.
The conductance shows a periodicity for the step position x_s and exhibits a period of $d/2$. Furthermore, the conductance has a local minimum at the position $x_s = d/4$. In general there is the symmetry:

$$G\left(\frac{d}{2} - x_s\right) = G\left(x_s\right). \tag{4.126}$$

In addition, the conductance strongly depends on the step size V_s. For larger V_s the curve of the conductance flattens. Interestingly, the dependency of the step position also shrinks for decreasing M.

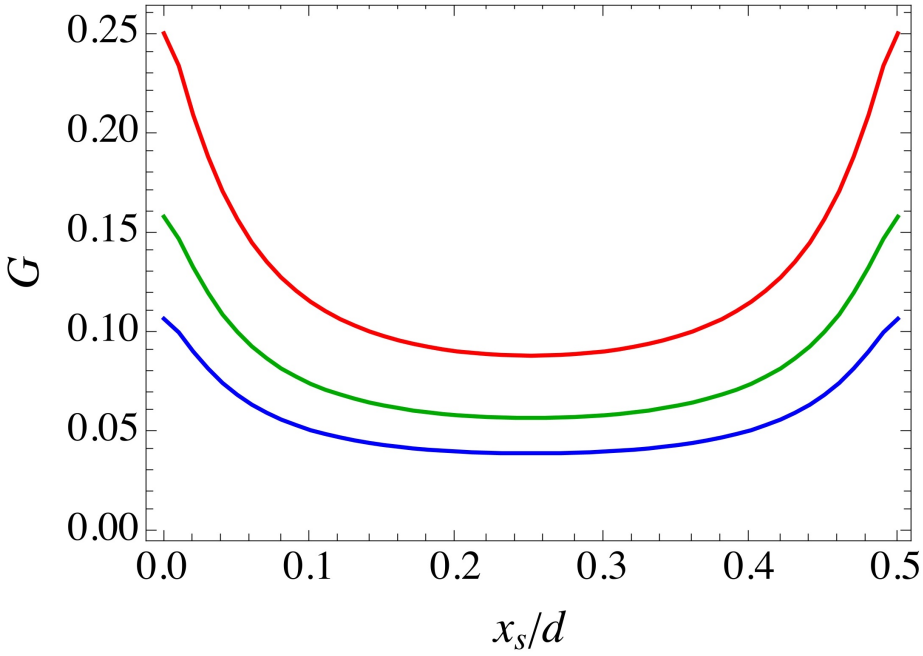

Figure 4.8: Conductance G in dependency of x_s. Figure from [50].
Here the illustration is for fixed $E_F = 0$ and $Md = 5$ while the step size varies. The plots follow from equation (4.124). $V_s d = 1.1$ corresponds to the red curve. Further $V_s d = 1.25$ is shown in green and $V_s d = 1.4$ blue.

4.6.3 Interface modes

In this part the case of localized solutions at the interface is considered. Hence, the focus is on the regime

$$|\,\mathrm{Tr}\;\Omega(E + V_L, k_y)| < -2, \quad |\,\mathrm{Tr}\;\Omega(E - V_R, k_y)| < -2, \tag{4.127}$$

assuming that there is a possible range of k_y where this is valid. The localized solutions form interface states at the step position x_s composed of type I and type II modes at opposite sides. A type II-II interface mode then is formed in the regime (4.127) which is also equivalent to the condition

$$f(\zeta_L) < -1, \quad f(\zeta_R) < -1 \tag{4.128}$$

with complex $K_{L,R}$,

$$K_L = i\mathcal{K}_L + \frac{\pi}{d}, \quad K_R = i\mathcal{K}_R + \frac{\pi}{d}. \tag{4.129}$$

For $E > 0$ and a type I-II interface mode one finds type II states on the left and type I states on the right of the step position, which indicates

$$K_L = -i\mathcal{K}_L + \frac{\pi}{d}, \quad K_R = +i\mathcal{K}_R. \tag{4.130}$$

This assignment flips for energies smaller than zero such that

$$K_L = -i\mathcal{K}_L, \quad K_R = +i\mathcal{K}_R - \frac{\pi}{d}. \tag{4.131}$$

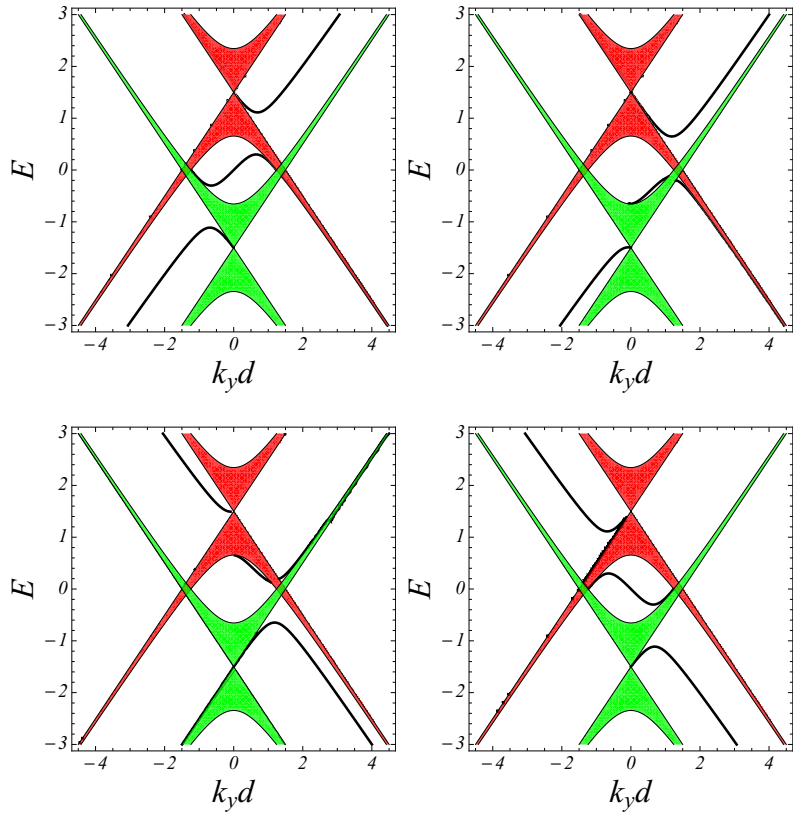

Figure 4.9: Dispersion relation of interface states. Adapted from [50].
Interface states for a potential step $V_s d = 1.5$ for $Md = 5$. The green and red regions correspond to Bloch states, while black lines indicate interface states. Interface states in the central region are of type II-II and in the outer region of type I-II. *top left:* $x_s = 0$. *top right:* $x_s = 0.1d$. *bottom left:* $x_s = 0.4d$. *bottom right:* $x_s = 0.5d$.

The matching condition will take the form

$$W_{E+V_s,M}(x_s) \begin{pmatrix} 1 \\ b_1 \end{pmatrix}_{K_L} = c\, W_{E-V_s,M}(x_s) \begin{pmatrix} 1 \\ b_1 \end{pmatrix}_{K_R}, \tag{4.132}$$

where $a_1 = 1$ and for b_1 see equations (4.110) and (4.111) analogous to section 4.6.1. From this one finds

$$\left(\Omega(E + V_s) - e^{iK_L d}\mathbb{1}\right) \begin{pmatrix} A(K_R) \\ B(K_R) \end{pmatrix} = 0. \tag{4.133}$$

This equation implicitly defines the dispersion relation of the interface mode. In fact, there exist type II-II interface modes in the central region around $(k_y d, E) = (0,0)$, see Figure 4.9. In this context also type I-II modes can be observed. Interestingly, no interface modes of type I-I exist. To understand this, note that these modes arise from a crossing point defined by either ($k_y = 0$, $E = V_s$) or ($k_y = 0$, $E = -V_s$). On the other hand, a necessary condition for the mode is $k_y^2 > (E_I \pm V_s)^2$. Both conditions cannot be valid at the crossing point simultaneously.

4.7 Zero-energy states

In this section the limit of large $\eta = dM \gg 1$ is discussed. The essential low-energy physics is captured by projecting onto the basis of zero-energy modes located at the positions of the kinks and anti-kinks of the mass. The kinks and anti-kinks form a one-dimensional bipartite lattice in the x-direction. The sublattice A comprises the sites at the positions $x_{An} = 2x_n - l/2$ for kinks, the sublattice B comprises the sites at the positions $x_{Bn} = 2x_n + l/2$ for anti-kinks, where $x_n = nd/2$ with $n \in \mathbb{Z}$ labels the unit cells. Furthermore, the origin of the coordinate system along x is shifted in this section by

$$x \to x - \frac{l}{2}, \tag{4.134}$$

so that the origin is an inversion point of the lattice and $M(-x) = M(x)$. In the unit cell around the origin there is $n = 0$ and $|x| < l$, such that the mass profile reads

$$M(x) = \begin{cases} (1+\gamma)M, & |x| < \frac{\ell}{2}, \\ -(1-\gamma)M, & \frac{\ell}{2} < |x| < \ell, \end{cases} \tag{4.135}$$

where γ is the asymmetry parameter. If $|\gamma|$ exceeds 1, the mass has always the same sign, and the zero modes disappear. In the following section $|\gamma| < 1$ is assumed. The periodicity of $M(x)$ follows from $M(x + x_n) = M(x)$. Notice that if $|\gamma| = 0$, then $M(x + l) = -M(x)$ and one retains equation (4.34). This property is lost if $|\gamma| \neq 0$. $M_K(x)$ and $\bar{M}_K(x)$ denote the kink and anti-kink profiles, where

$$\begin{aligned} M_K(x) &= (1+\gamma)M\theta(x) - (1-\gamma)M\theta(-x) \\ &= M\mathrm{sign}(x) + \gamma M, \end{aligned} \tag{4.136}$$

$$\begin{aligned} \bar{M}_K(x) &= -(1-\gamma)M\theta(x) + (1+\gamma)M\theta(-x) \\ &= -M\mathrm{sign}(x) + \gamma M \end{aligned} \tag{4.137}$$

with

$$M_K(-x) = \bar{M}_K(x). \tag{4.138}$$

The zero-energy states for a kink or anti-kink satisfy

$$\begin{aligned}(-i\sigma_x\partial_x + \mathcal{M}_K(x)\sigma_z)\,\phi_+(x) = 0,\\ \left(-i\sigma_x\partial_x + \bar{\mathcal{M}}_K(x)\sigma_z\right)\phi_-(x) = 0\end{aligned} \tag{4.139}$$

and are given explicitly by

$$\phi_\pm(x) = \sqrt{M(1-\gamma^2)}\,e^{-F(\pm x)}|\pm\rangle, \tag{4.140}$$

where

$$F(x) = Mx[(1+\gamma)\theta(x) - (1-\gamma)\theta(-x)] = M|x| + Mx\gamma \tag{4.141}$$

$$|\pm\rangle = \frac{1}{\sqrt{2}}\begin{pmatrix}1\\ \pm i\end{pmatrix}. \tag{4.142}$$

Notice that $\phi_\pm(x)$ are orthonormalized eigenstates of σ_y, and $\phi_-(x) = \sigma_z\phi_+(-x)$. The electron field operator in terms of zero modes is then given by

$$\hat{\Psi}(x,y) = \sum_n\,[\phi_+(x-x_{An})\,\hat{\psi}_{An}(y) + \phi_-(x-x_{Bn})\,\hat{\psi}_{Bn}(y)] \tag{4.143}$$

$$= \frac{1}{\sqrt{L}}\sum_{n,k_y}\,e^{ik_y y}\,[\phi_+(x-x_{An})\,c_{Ank_y} + \phi_-(x-x_{Bn})\,c_{Bnk_y}], \tag{4.144}$$

where $\hat{\psi}_{\alpha n}(y)$ are one-dimensional fermion field operators for each sublattice $\alpha = A,B$ and $c_{\alpha nk_y}$ denotes the fermion operators. In addition, the states fulfill the periodic boundary condition $\hat{\psi}_{\alpha n}(y+L) = \hat{\psi}_{\alpha n}(y)$ with $k_y = \frac{2\pi m}{L}$. The effective low-energy Hamiltonian is then obtained by projecting the initial Hamiltonian (4.1) onto (4.144) and assuming the mass profile to be like (4.135) and $V = 0$. Finally, one finds

$$\begin{aligned}H_{eff} &= \int dxdy\,\hat{\Psi}^\dagger(x,y)H\hat{\Psi}(x,y)\\ &= \sum_{\alpha\alpha',nn',k_y} c^\dagger_{\alpha nk_y}h^{\alpha\alpha'}_{nn'}(k_y)\,c_{\alpha' n'k_y},\end{aligned} \tag{4.145}$$

with

$$h^{AA}_{nn'}(k_y) = k_y \int dx\, \phi_+(x - x_{An})\phi_+(x - x_{An'})$$

$$= k_y M(1-\gamma^2) \int dx\, e^{-F(x-x_{An})-F(x-x_{An'})}, \tag{4.146}$$

$$h^{BB}_{nn'}(k_y) = -k_y \int dx\, \phi_-(x - x_{Bn})\phi_-(x - x_{Bn'})$$

$$= -k_y M(1-\gamma^2) \int dx\, e^{-F(-x+x_{Bn})-F(-x+x_{Bn'})}, \tag{4.147}$$

$$h^{AB}_{nn'}(k_y) = \int dx\, \phi_+(x - x_{An})[M(x) - \bar{M}_K(x - x_{Bn'})]\phi_-(x - x_{Bn'})$$

$$= M(1-\gamma^2) \int dx\, e^{-F(x-x_{An})-F(-x+x_{Bn'})}[M(x) - \bar{M}_K(x - x_{Bn'})], \tag{4.148}$$

$$h^{BA}_{nn'}(k_y) = \int dx\, \phi_-(x - x_{Bn})[M(x) - \bar{M}_K(x - x_{An})]\phi_+(x - x_{An'})$$

$$= M(1-\gamma^2) \int dx\, e^{-F(-x+x_{Bn})-F(x-x_{An'})}[M(x) - M_K(x - x_{An'})]. \tag{4.149}$$

One can show that $h^{AB}_{nn'}(k_y) = h^{BA}_{nn'}(k_y)$, as the Hamiltonian must be Hermitian. All these matrix elements only depend on the separation

$$x_{nn'} = x_n - x_{n'} = (n - n') = d \tag{4.150}$$

and decay exponentially with it. Equation (4.146) yields with (4.150)

$$h^{AA}_{nn'}(k_y) = k_y M(1-\gamma^2) \int dx\, e^{-F(x-x_{An})-F(x-x_{An'})} = k_y M(1-\gamma^2) \int dx\, e^{-F(x-x_{nn'})-F(x)}$$

$$= k_y f_{|n-n'|}, \tag{4.151}$$

where the dimensionless numbers are defined as

$$f_{|n-n'|} = f_o = (1-\gamma^2)\eta \int dt\, \exp\left(-\eta(|t| + |t-o| + \gamma(2t-o))\right)$$

$$= \left(\cosh(\gamma o M d) + \frac{\sinh(\gamma o M d)}{\gamma}\right) \exp(-oMd) \tag{4.152}$$

with o = 0,1,2,3,... and $h^{AA}_{nn'}(k_y) = -h^{BB}_{nn'}(k_y)$ and change of variable $t = x/d$. The numbers f, see equation (4.152), are the overlaps between zero-energy modes of the same sublattice. In particular, notice that $f(0) = 1$. The overlaps between zero-energy modes of different sublattices vanish because of the opposite eigenstates of σ_y. The

integral of the off-diagonal element (4.148) can be evaluated with exponential accuracy for the cases of interest, i.e., for small values of the separation (4.150). $h^{AB}_{nn'}(k_y)$ is then independent of k_y and can be rewritten to the form

$$h^{AB}_{nn'} = M(1-\gamma^2)\int dx\, e^{-F(x-x_{nn'}+l)-F(-x)}[M(x+l/2)-\bar{M}_K(x)]$$

$$= Mg_{|n-n'|}, \tag{4.153}$$

where the dimensionless function g_m is given by

$$g_m = (1-\gamma^2)Md\,\exp\left(\gamma\left(m-\frac{1}{2}\right)Md\right)\int dt\,\exp\left(-Md(|t|+|t-m+1/2|)\right)$$

$$\times\left(\frac{M(t+1/4)}{M}+\mathrm{sgn}(t)-\gamma\right). \tag{4.154}$$

The cases of interest are

$$g_0 \approx -(1-\gamma^2)e^{-(1+\gamma)\frac{Md}{2}}, \tag{4.155}$$

$$g_1 \approx (1-\gamma^2)e^{-(1-\gamma)\frac{Md}{2}}. \tag{4.156}$$

In equation (4.153) the periodicity of $M(x+x_n)=M(x)$ is used. Note that $M(-x)=M(x)$ and $M(x+l)=-M(x)$ hold for $\gamma=0$ and imply $g(n)=-g_{1-m}$. Both functions f and g decrease exponentially with the separation $x_{nn'}$. It is therefore enough to keep only the term n' for f and the terms n' and $n'+1$ for g in equation (4.145). The reason for the two terms for g is that the first describes hopping between A and B sites in the same unit cell of the bipartite lattice, while the second describes the hopping between A and B sites in neighboring unit cells. One defines the Fourier transformation in x-direction based on the fermion operators

$$c_{\alpha nk_y} = \int_{-\pi/d}^{\pi/d}\frac{dK}{2\pi}\exp(inKd)c_{\alpha Kk_y}, \quad \alpha = A,B. \tag{4.157}$$

Since the functions f and g only depend on the difference (4.150), the Hamiltonian in Fourier space is diagonal and one gets

$$\hat{H} = \frac{1}{L}\sum_k\int\frac{dK}{2\pi}\tilde{f}(k_x)k_y\left(c^\dagger_{AKk_y}c_{AKk_y}-c^\dagger_{BKk_y}c_{BKk_y}\right)$$

$$+\left(\tilde{g}(K)Mc^\dagger_{AKk_y}c_{BKk_y}+\tilde{g}^*(K)c^\dagger_{BKk_y}c_{AKk_y}\right). \tag{4.158}$$

For $L\to\infty$ this results in

$$H_{eff} = \int\frac{dKdk_y}{(2\pi)^2}\begin{pmatrix}c^\dagger_{Ajk_y}\\ c^\dagger_{Bjk_y}\end{pmatrix}\tilde{\mathcal{H}}(K,k_y)\begin{pmatrix}c_{Ajk_y}\\ c_{Bjk_y}\end{pmatrix}, \tag{4.159}$$

with

$$\tilde{\mathcal{H}}(K,k_y) = \begin{pmatrix} \tilde{f}(K)k_y & \tilde{g}(K)M \\ \tilde{g}^*(K)M & -\tilde{f}(K)k_y \end{pmatrix} \tag{4.160}$$

and

$$\tilde{f}(K) = f_0 + 2\sum_{l=1}^{\infty} f_l \cos(lKd) \approx 1, \tag{4.161}$$

$$\tilde{g}(K) = \sum_m g_m e^{-imKd} \approx g_0 + g_1 e^{-iKd}. \tag{4.162}$$

Diagonalizing the Hamiltonian (4.160) by taking care of the approximated Fourier transformed expressions (4.161) gives the eigenenergies

$$E(K,k_y) = \pm\sqrt{k_y^2 + M^2[g_0^2 + g_1^2 + 2g_0 g_1 \cos(Kd)]} \tag{4.163}$$

and directly reproduces the zero order obtained via the spectral equation (4.54) in chapter 4.2. For $\gamma = 0$, this expression coincides with the expansion of the exact dispersion close to the Γ-point (4.86) and again gives an anisotropic massive Dirac fermion energy

$$E(K,k_y) = \pm\sqrt{\tilde{v}_x^2 K^2 + v_F^2 k_y^2 + \Delta^2}, \tag{4.164}$$

with

$$\Delta = 2(1-\gamma^2)M \exp(-Md/2)\sinh(\gamma Md/2), \tag{4.165}$$

$$\frac{\tilde{v}_x}{v_F} = (1-\gamma^2)Md\exp(-Md/2). \tag{4.166}$$

Close to this point, the Hamiltonian reads

$$\tilde{\mathcal{H}}(K,k_y) = Mg_1 Kd\,\tau_y + k_y\tau_z - \left(\Delta + \frac{1}{2}Mg_1(Kd)^2\right)\tau_x, \tag{4.167}$$

where τ_a denotes the Pauli matrices in sublattice space which is formed by kinks and anti-kinks and the gap $\Delta = -(g_0+g_1)M > 0$. This Hamiltonian can be mapped onto the standard gapped graphene Hamiltonian by a unitary transformation. Since $v_{x,0} = \tilde{v}_x$ equation (4.88) is reproduced by (3.68) in the case of vanishing γ.

4.8 Magnetic field

In this section, the idea of the Dirac equation with periodic mass in the presence of a uniform magnetic field perpendicular to the system is sketched. By use of the Landau gauge $A = (0,Bx,0)$ the Hamiltonian (4.1) is adapted to

$$H = [-i\sigma_x\partial_x + \sigma_y(-i\partial_y + x/l_B^2)] + M(x)\sigma_z + V(x)\mathbb{1}. \tag{4.168}$$

Here again, $\hbar = v = 1$ and the magnetic length $l_B = \sqrt{\hbar c/eB}$ and (4.2) is used. Furthermore, the variables are dimensionless with length in units of the magnetic length l_B and energy in the units of the cyclotron frequency ω_c.
Using the translational invariance in the y-direction, one can write

$$\Psi(x,y) = \exp(ik_y y)\,\phi_{k_y}(x), \tag{4.169}$$

and the Hamiltonian (4.168) takes the form

$$H(k_y) = \frac{1}{\sqrt{2}}(-i\sigma_x\partial_x + \sigma_y(k_y + x)) + M(x)\sigma_z \tag{4.170}$$

$$= \begin{pmatrix} M & -ia \\ ia^\dagger & -M \end{pmatrix}, \tag{4.171}$$

where the potential V is neglected and

$$a = \partial_q + \frac{q}{2}, \quad a^\dagger = -\partial_q + \frac{q}{2},$$

$$q = \sqrt{2}(x + k_y), \quad [a,a^\dagger] = 1.$$

By use of $\phi_{k_y}(x) = (u,v)^T$ the two equations

$$av = i(E - M - V)u, \quad a^\dagger u = -i(E + M - V)v \tag{4.172}$$

arise and by eliminating u one finds for the case of $V = 0$

$$-iv(a^\dagger a - (E^2 - M^2)) = 0. \tag{4.173}$$

This looks quite familiar to a Webers like equation. Solving (4.173) one can assume $v_1 = iD_p(q)$ with $D_p(q)$ representing the parabolic cylinder function. In the following the relations

$$a = \frac{pD_{p-1}(q)}{D_p(q)} \quad \text{and} \quad a^\dagger = \frac{D_{p+1}(q)}{D_p(q)} \tag{4.174}$$

will be used. With the use of (4.172) the expression for u_1 is fixed to

$$u_1 = p\,\frac{D_{p-1}(q)}{E - M}. \tag{4.175}$$

Analogously one can find for $v_2 = -iD_p(-q)$ the second solution. The shift of $q \to -q$ implies also a change of sign in a and gives

$$u_2 = p\,\frac{D_{p-1}(-q)}{E - M}. \tag{4.176}$$

Finally the eigenstates are given by

$$\phi_M^{(1)}(x) = \begin{pmatrix} (E^2 - M^2)\frac{D_{p-1}(q)}{E-M} \\ iD_p(q) \end{pmatrix} = \begin{pmatrix} (E + M)D_{p-1}(q) \\ iD_p(q) \end{pmatrix}, \tag{4.177}$$

$$\phi_M^{(2)}(x) = \begin{pmatrix} (E + M)D_{p-1}(-q) \\ -iD_p(-q) \end{pmatrix}. \tag{4.178}$$

Here, M is assumed to be constant and p follows from equations (4.174) and (4.173). For the case of a single mass kink the ansatz analogous to (4.13) will be used. The general solution can then be written as

$$\Psi(x) = W_M(x) \begin{pmatrix} a \\ b \end{pmatrix}, \tag{4.179}$$

where the matrix $W_M(x)$ is given by

$$W_M(x) = \left(\phi_M^{(2)}(x)\ \phi_M^{(1)}(x)\right) \tag{4.180}$$

$$= \begin{pmatrix} (E+M)D_{p-1}(-q) & (E+M)D_{p-1}(q) \\ -iD_p(-q) & iD_p(q) \end{pmatrix}. \tag{4.181}$$

Imposing continuity at position $x = 0$ gives

$$W_M^{-1}(0)W_{-M}(0) \begin{pmatrix} a_L \\ 0 \end{pmatrix} = \begin{pmatrix} 0 \\ b_R \end{pmatrix}. \tag{4.182}$$

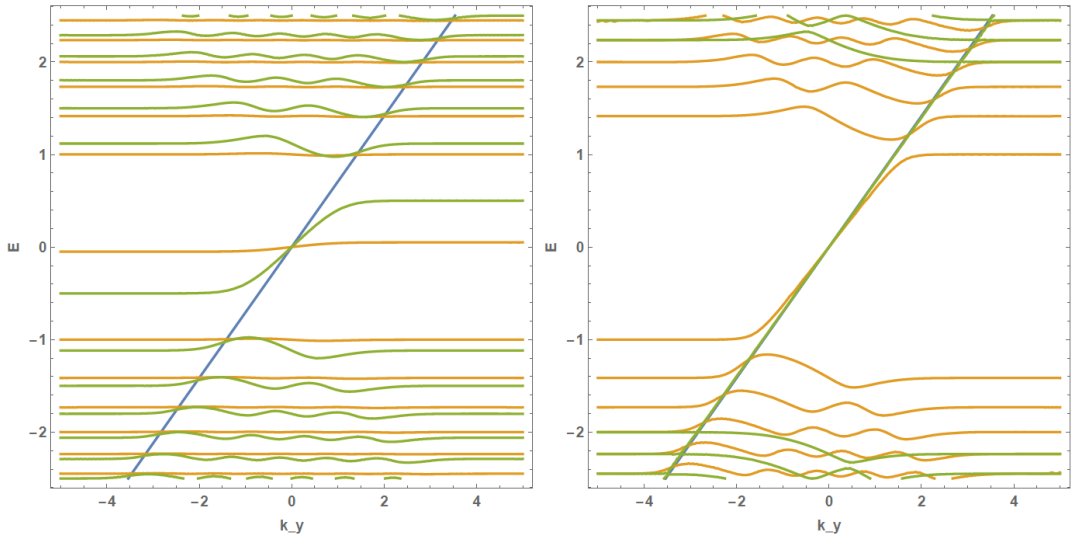

Figure 4.10: Dispersion relation for single mass kink following (4.183) and (4.184). The blue line indicates the linear dispersion $E = k_y/\sqrt{2}$. *left:* Calculation done for $M = 0.05$ (yellow) and $M = 0.5$ (green). *right:* Here $M = 1{,}2$ are used for the yellow and green lines. The green line exactly covers the linear dispersion.

The quantization condition is then

$$\left[W_M^{-1}(0)W_{-M}(0)\right]_{11} = 0, \tag{4.183}$$

which finally gives

$$(E-M)D_p(\sqrt{2}k_y)D_{p-1}(-\sqrt{2}k_y)+(E+M)D_{p-1}(\sqrt{2}k_y)D_p(-\sqrt{2}k_y)=0. \quad (4.184)$$

For an infinite system, one gets the usual relativistic Landau levels

$$E_n = sign(n)\sqrt{|n|+M^2}, \quad n=\pm 1,\pm 2,\pm 3... \quad (4.185)$$

$$E_0 = -M, \quad (4.186)$$

where the solution is not normalizable. The numerical solution of equation (4.184) is shown in Figure 4.10. For $M \ll 1$ there are almost perfectly flat Landau levels. For increasing values of M one can see that the Landau levels acquire a dispersion, especially close to $k_y = 0$. For M sufficiently large the usual interface mode with linear dispersion which exists for $B = 0$ is recovered.

4.9 Summary

In this chapter, two-dimensional Dirac fermions in a mass superlattice have been discussed. The mass superlattice was assumed to be piece-wise constant and alternates between positive and negative mass along the y-direction.
We showed that the low-energy calculation binds a Jackiw-Rebbi zero mode. Furthermore, we find the anisotropic Dirac cone dispersion. Due to the most general ansatz imaginary and real solutions for the periodicity conditions are allowed. We predict the existence of boundary modes and in presence of a potential step the existence of interface modes. These modes characterize evanescent solutions of the periodicity condition. Interestingly, we find two different types of interface modes. The first type occurs for a momentum larger than the energy and the second type for a momentum that is smaller than the energy.
We suppose that the boundary and interface modes carry unidirectional currents and therefore could be observable in STM measurements.

Chapter 5

Conclusion and Outlook

In this chapter we give a short summary of some key aspects and findings and outline the opportunities for further investigation and experiments.
In chapter 3 we started to introduce the most important quantities of twisted bilayer graphene. Most of the properties can be described in terms of its band structure. These energy bands are called moiré bands which originate from the superlattice, the moiré lattice. The superlattice affects the properties of the structure. While monolayer graphene exhibits Dirac cones, the energy levels of twisted bilayer graphene completely flatten for a well defined series of magic angles, see section 3.6. Thus, it seems to be obvious that superlattice effects can modify band structures and introduce novel properties. We have been able to show numerically that the values of the magic angles, apart from the first, highly depend on the strength of coupling amplitudes in AA stacked and AB/BA stacked regions. Interestingly, the first magic angle seems to be nearly robust.
In chapter 4 we then focused on a mass superlattice with a piece-wise constant mass term that alternates between positive and negative values. We have been able to show that this model turns out to be exactly solvable. We saw that the low-energy part of the spectrum is spanned in this model by the chiral zero mode. Therefore, the low-energy physics are directly linked to the chiral zero modes. Furthermore, we find the anisotropic Dirac cone dispersion as well as boundary modes. Looking at the dispersion relation for boundary modes, we see an asymmetry in k_y which implies unidirectional currents carried by the boundary modes. Thus, we expect that the modes can be observed in transport experiments. Furthermore, they could be detected in STM measurements. In presence of a potential step we also predict two different types of interface modes. Firstly, we recover type I states with momentum $|ky|$ larger than the energy $|E|$. Secondly, for a momentum $|ky|$ smaller than the energy $|E|$ we talk about type II states. These type II states can only occur if the product of the amplitude of the mass term and the superlattice period is greater than 2. Both types

should be observable analogous to the boundary modes above.
In general, the work and the introduced model of the mass superlattice can be useful for further experimental and theoretical work on this topic. For instance the model can be expanded with the intention to study magnetic fields, see section 4.8, or electron-electron interactions.

Bibliography

[1] Toshiya Ideue and Yoshihiro Iwasa. Symmetry breaking and nonlinear electric transport in van der waals nanostructures. *Annu. Rev. Condens. Matter Phys.*, 12(1):201–223, 2021.

[2] Jennifer Cano, Shiang Fang, J. H. Pixley, and Justin H. Wilson. Moiré superlattice on the surface of a topological insulator. *Phys. Rev. B*, 103:155157, Apr 2021.

[3] Philip Richard Wallace. The band theory of graphite. *Physical review*, 71(9):622, 1947.

[4] Lev Davidovich Landau. On the theory of phase transitions. i. *Zh. Eksp. Teor. Fiz.*, 11:19, 1937.

[5] Lev Davidovich Landau. On the theory of phase transitions. ii. *Zh. Eksp. Teor. Fiz.*, 11:627, 1937.

[6] Kostya S Novoselov, Andre K Geim, Sergei V Morozov, De-eng Jiang, Yanshui Zhang, Sergey V Dubonos, Irina V Grigorieva, and Alexandr A Firsov. Electric field effect in atomically thin carbon films. *science*, 306(5696):666–669, 2004.

[7] Kostya S Novoselov, Andre K Geim, Sergei Vladimirovich Morozov, Dingde Jiang, Michail I Katsnelson, Irina V Grigorieva, SVb Dubonos, Firsov, and AA. Two-dimensional gas of massless dirac fermions in graphene. *nature*, 438(7065):197–200, 2005.

[8] The Royal Swedish Academy of Sciences. The nobel prize in physics 2010, 2010.

[9] Rafi Bistritzer and Allan H MacDonald. Moiré bands in twisted double-layer graphene. *Proceedings of the National Academy of Sciences*, 108(30):12233–12237, 2011.

[10] JMB Lopes Dos Santos, NMR Peres, and AH Castro Neto. Continuum model of the twisted graphene bilayer. *Physical review B*, 86(15):155449, 2012.

[11] Leon Balents. General continuum model for twisted bilayer graphene and arbitrary smooth deformations. *SciPost Physics*, 7(4):048, 2019.

[12] Mikito Koshino. Interlayer interaction in general incommensurate atomic layers. *New Journal of Physics*, 17(1):015014, 2015.

[13] Alexandr Vladimirovich Rozhkov, AO Sboychakov, AL Rakhmanov, and Franco Nori. Electronic properties of graphene-based bilayer systems. *Physics Reports*, 648:1–104, 2016.

[14] Gonçalo Catarina, Bruno Amorim, Eduardo V Castro, JMVP Lopes, and Nuno Peres. Twisted bilayer graphene: low-energy physics, electronic and optical properties. *Handbook of Graphene*, 3:177–232, 2019.

[15] Yuan Cao, Valla Fatemi, Shiang Fang, Kenji Watanabe, Takashi Taniguchi, Efthimios Kaxiras, and Pablo Jarillo-Herrero. Unconventional superconductivity in magic-angle graphene superlattices. *Nature*, 556(7699):43–50, 2018.

[16] GM Maksimova, ES Azarova, AV Telezhnikov, and VA Burdov. Graphene superlattice with periodically modulated dirac gap. *Physical review B*, 86(20):205422, 2012.

[17] José Alberto Briones-Torres, J Madrigal-Melchor, Juan Carlos Martínez-Orozco, and Isaac Rodríguez-Vargas. Electrostatic and substrate-based monolayer graphene superlattices: Energy minibands and its relation with the characteristics of the conductance curves. *Superlattices and Microstructures*, 73:98–112, 2014.

[18] Roman Jackiw and Cláudio Rebbi. Solitons with fermion number 1/2. *Physical Review D*, 13(12):3398, 1976.

[19] Andre K Geim and Irina V Grigorieva. Van der waals heterostructures. *Nature*, 499(7459):419–425, 2013.

[20] Xavier Blase, Angel Rubio, Steven G Louie, and Marvin L Cohen. Quasiparticle band structure of bulk hexagonal boron nitride and related systems. *Physical review B*, 51(11):6868, 1995.

[21] John C Slater and George F Koster. Simplified lcao method for the periodic potential problem. *Physical review*, 94(6):1498, 1954.

[22] Charles Kittel and Paul McEuen. *Introduction to solid state physics*. John Wiley & Sons, 2018.

[23] Richard M Martin. *Electronic structure: basic theory and practical methods*. Cambridge university press, 2020.

[24] Neil W Ashcroft and N David Mermin. *Solid state physics*. Cengage Learning, 2022.

[25] R de L Kronig and William George Penney. Quantum mechanics of electrons in crystal lattices. *Proceedings of the royal society of London. series A, containing papers of a mathematical and physical character*, 130(814):499–513, 1931.

[26] AM Eldib, HF Hassan, and MA Mohamed. Generalisation of the kronig-penney

model. *Journal of Physics C: Solid State Physics*, 20(20):3011, 1987.

[27] David Griffiths. *Introduction to elementary particles*. John Wiley & Sons, 2020.

[28] Jun John Sakurai, San Fu Tuan, and Roger G Newton. Modern quantum mechanics, 1986.

[29] Paul Adrien Maurice Dirac. The quantum theory of the electron. *Proceedings of the Royal Society of London. Series A, Containing Papers of a Mathematical and Physical Character*, 117(778):610–624, 1928.

[30] M Zahid Hasan and Charles L Kane. Colloquium: topological insulators. *Reviews of modern physics*, 82(4):3045, 2010.

[31] AA Burkov and Leon Balents. Weyl semimetal in a topological insulator multilayer. *Physical review letters*, 107(12):127205, 2011.

[32] AH Castro Neto, Francisco Guinea, Nuno MR Peres, Kostya S Novoselov, and Andre K Geim. The electronic properties of graphene. *Reviews of modern physics*, 81(1):109, 2009.

[33] G Dresselhaus, Mildred S Dresselhaus, and Riichiro Saito. *Physical properties of carbon nanotubes*. World scientific, 1998.

[34] Rolf Landauer. Spatial variation of currents and fields due to localized scatterers in metallic conduction. *IBM Journal of research and development*, 1(3):223–231, 1957.

[35] M Büttiker. Role of quantum coherence in series resistors. *Physical Review B*, 33(5):3020, 1986.

[36] TJ Thornton, CJB Ford, DA Wharam, R Newbury, M Pepper, H Ahmed, JEF Frost, DC Peacock, DA Ritchie, and GAC Jones. Transport properties of narrow, variable width channels in the 2deg of a gaas: Algaas heterojunction. In *Physics and Technology of Submicron Structures: Proceedings of the Fifth International Winter School, Mauterndorf, Austria, February 22–26, 1988*, pages 208–217. Springer, 1988.

[37] Grigory Tarnopolsky, Alex Jura Kruchkov, and Ashvin Vishwanath. Origin of magic angles in twisted bilayer graphene. *Physical review letters*, 122(10):106405, 2019.

[38] G Trambly De Laissardiere, Didier Mayou, and Laurence Magaud. Numerical studies of confined states in rotated bilayers of graphene. *Physical Review B*, 86(12):125413, 2012.

[39] Andrey Kretinin, GL Yu, Rashid Jalil, Yuan Cao, Freddie Withers, Artem Mishchenko, MI Katsnelson, KS Novoselov, AK Geim, and Fransisco Guinea. Quantum capacitance measurements of electron-hole asymmetry and next-nearest-

neighbor hopping in graphene. *Physical Review B*, 88(16):165427, 2013.

[40] JMB Lopes Dos Santos, NMR Peres, and AH Castro Neto. Graphene bilayer with a twist: Electronic structure. *Physical review letters*, 99(25):256802, 2007.

[41] Biao Lian, Zhijun Wang, and B Andrei Bernevig. Twisted bilayer graphene: A phonon-driven superconductor. *Physical review letters*, 122(25):257002, 2019.

[42] Eugene J Mele. Commensuration and interlayer coherence in twisted bilayer graphene. *Physical Review B*, 81(16):161405, 2010.

[43] S Shallcross, S Sharma, E Kandelaki, and OA Pankratov. Electronic structure of turbostratic graphene. *Physical Review B*, 81(16):165105, 2010.

[44] R De Gail, MO Goerbig, F Guinea, G Montambaux, and AH Castro Neto. Topologically protected zero modes in twisted bilayer graphene. *Physical Review B*, 84(4):045436, 2011.

[45] Stephen Carr, Shiang Fang, Ziyan Zhu, and Efthimios Kaxiras. Exact continuum model for low-energy electronic states of twisted bilayer graphene. *Physical Review Research*, 1(1):013001, 2019.

[46] Oskar Vafek and Jian Kang. Renormalization group study of hidden symmetry in twisted bilayer graphene with coulomb interactions. *Physical Review Letters*, 125(25):257602, 2020.

[47] Jie Wang, Yunqin Zheng, Andrew J Millis, and Jennifer Cano. Chiral approximation to twisted bilayer graphene: Exact intravalley inversion symmetry, nodal structure, and implications for higher magic angles. *Physical Review Research*, 3(2):023155, 2021.

[48] Fengcheng Wu, Allan H MacDonald, and Ivar Martin. Theory of phonon-mediated superconductivity in twisted bilayer graphene. *Physical review letters*, 121(25):257001, 2018.

[49] Aline Ramires and Jose L Lado. Electrically tunable gauge fields in tiny-angle twisted bilayer graphene. *Physical review letters*, 121(14):146801, 2018.

[50] Alessandro De Martino, Luca Dell'Anna, Lukas Handt, Andrea Miserocchi, and Reinhold Egger. Two-dimensional dirac fermions in a mass superlattice. *Physical Review B*, 107(11):115420, 2023.

Eidesstattliche Versicherung

Ich versichere an Eides Statt, dass die Dissertation von mir selbständig und ohne unzulässige fremde Hilfe unter Beachtung der „Grundsätze zur Sicherung guter wissenschaftlicher Praxis an der Heinrich-Heine-Universität Düsseldorf" erstellt worden ist. Weiterhin erkläre ich, dass ich diese Dissertation keiner anderen Fakultät bereits vorgelegt habe und ich bisher keinerlei erfolglose oder erfolgreiche Promotionsversuche unternommen habe. Darüberhinaus ist mir bekannt, dass jedweder Betrugsversuch zum Nichtbestehen oder Aberkennung der Prüfungsleistung führen kann.

Ort, Datum	Lukas Handt

Acknowledgements

Ich danke ...
... meinem Doktorvater Prof. Dr. Reinhold Egger für die Unterstützung und Hilfe in meiner Zeit als Doktorand, aber auch in den Zeiten als Bachelor- und Masterstudent. Ich danke dafür, dass er immer ein offenes Ohr hatte und immer erreichbar war, auch während der Pandemie.
... PD Dr. Hermann Kampermann für die Übernahme der Mentorenschaft und des Koreferats dieser Dissertation.
... Prof. Dr. Alessandro De Martino, Associate Professor Dr. Luca Dell'Anna und Andrea Miserocchi für die gute Zusammenarbeit und interessanten Diskussionen.
... allen aktuellen und früheren Mitgliedern des Instituts für Theoretische Physik IV der HHU für die herzliche Aufnahme schon als Bachelorstudent. Besonders danken möchte ich hier Dr. Oleksander Zazunov für die hilfreichen Gespräche zu Projektbeginn und auch zu Zeiten des Masterstudiums war er immer ein wichtiger Ansprechpartner. Außerdem danke ich Tim Bauer und Samuel Morales für das Lesen meiner Dissertation und die hilfreichen Diskussionen. Ein großer Dank geht an Claudia Stader für die Hilfe bei vielen organisatorischen Dingen und die lieben Gesprächen. Weiter danke ich Dr. Kathrin Dorn und Kateryna Zatsarynna für die angenehme Büronachbarschaft und schönen sowie hilfreichen Gesprächen.
... Dr. Mehrdad Golkia und Dr. Christian Wimmenauer für die Unterstützung bei organisatorischen Fragen und hilfreichen Telefonaten.
... Andreas Gruner, der die Faszination für die Physik in meiner Schulzeit noch weiter angefacht hat.
... meinen Eltern Markus und Susanne sowie meiner Schwester Maike für die Unterstüzung in egal welcher Lebenslage.
... meinem besten Freund Fred, der mich seit Kindertagen begleitet, für die Gespräche fernab der Physik.

Publication

Two-dimensional Dirac fermions in a mass superlattice

Alessandro De Martino, Luca Dell'Anna, Lukas Handt, Andrea Miserocchi, and Reinhold Egger, Phys. Rev. B 107, 115420 (2023).
DOI: https://doi.org/10.1103/PhysRevB.107.115420
My contributions to this project was the scientific discussions, work and preparation of the paper. I was involved in the analytical calculation of the model itself and such in calculation of the three general assumption of homogeneous mass, mass kink and mass barrier as well as the periodic mass case. Furthermore, I was involved in the calculation of the potential step like calculation the reflection, transmission and conductance. Moreover, I generated numerical data for the spectral equation. I also implemented the reflection, transmission and conductance numerically and generated the data.

Two-dimensional Dirac fermions in a mass superlattice

Alessandro De Martino,[1] Luca Dell'Anna,[2] Lukas Handt,[3] Andrea Miserocchi,[2,3] and Reinhold Egger[3]
[1]*Department of Mathematics, City, University of London, London EC1V 0HB, United Kingdom*
[2]*Dipartimento di Fisica e Astronomia G. Galilei, Università degli studi di Padova, 35131 Padova, Italy*
[3]*Institut für Theoretische Physik, Heinrich-Heine-Universität, D-40225 Düsseldorf, Germany*

(Received 19 December 2022; accepted 6 March 2023; published 20 March 2023)

We study two-dimensional (2D) Dirac fermions in the presence of a periodic mass term alternating between positive and negative values along one direction. This scenario could be realized for a graphene monolayer or for the surface states of topological insulators. The low-energy physics is governed by chiral Jackiw-Rebbi modes propagating along zero-mass lines, with the energy dispersion of the Bloch states given by an anisotropic Dirac cone. By means of the transfer matrix approach, we obtain exact results for a piecewise constant mass superlattice. On top of Bloch states, two different classes of boundary and/or interface modes can exist in a finite-size geometry or in a nonuniform electrostatic potential, respectively. We compute the dispersion relation for both types of boundary and interface modes, which originate either from states close to the superlattice Brillouin zone (BZ) center or, via a Lifshitz transition, from states near the BZ boundary. In the presence of a potential step, we predict that the interface modes, the Bloch wave functions, and the electrical conductance will sensitively depend on the step position relative to the mass superlattice.

DOI: 10.1103/PhysRevB.107.115420

I. INTRODUCTION

It is well known that the band structure of solids can be modified in a controllable way by means of superlattice potentials. For instance, the use of electrostatic superlattice potentials has been suggested as versatile and tunable tool for creating emergent Dirac fermions with anisotropic dispersion in two-dimensional (2D) graphene monolayers [1–7] or in few-layer black phosphorus devices [8]. Similarly, moiré superlattice effects can induce a spectacular restructuring of the band structure in twisted bilayer graphene [9], layered van der Waals materials [10], and topological insulators (TIs) [11], including the formation of topologically nontrivial and nearly flat bands with strong correlation effects [12]. Apart from the mostly considered case of electrostatic superlattices, interesting modifications of the band structure have also been predicted for magnetic superlattices and for periodic modulations of the spin-orbit coupling; see, e.g., Refs. [13–16] for the case of graphene monolayers.

In the present work, we focus on yet another superlattice type which can be realized in 2D Dirac materials, e.g., in graphene monolayers [17] or the surface states of TIs [18,19]. We study the effects of a one-dimensional (1D) *mass superlattice* $M(x)$, which periodically alternates between regions of positive and negative mass. (The mass term is assumed homogeneous along the y direction, with the 2D material in the xy plane.) For the graphene case, such a mass profile could arise from a sublattice-dependent potential due to substrate or strain effects [17]. For TI surface states, it could (approximately) be generated by the exchange field of an array of magnetic stripes with alternating magnetization direction.

It is well known that a single mass kink binds a fermionic zero mode by the Jackiw-Rebbi mechanism [20–22]. This zero mode is unidirectional ("chiral") and propagates with the Fermi velocity v_F either in the positive or negative y direction while being exponentially localized near the mass kink along the x direction. In general terms, a sign change of the mass for 2D Dirac fermions corresponds to a transition between two topological Chern insulators with a different Chern number [23]. By the bulk-boundary correspondence, zero-mass lines at the interfaces then harbor chiral zero modes. For the TI realization, experimental evidence for such chiral zero modes has been reported in Refs. [24,25]. In Bernal-stacked bilayer graphene devices, in the presence of either interlayer bias voltage kinks, tilt boundaries, or in folded geometries, one expects topological valley-momentum-locked zero-line modes [26,27] that closely resemble the above chiral zero mode [28,29]. We refer the reader to Ref. [30] for a recent survey, including a summary of the experimental evidence for zero-line modes in bilayer graphene. In particular, such modes have been identified by scanning tunneling microscopy (STM) [31]. Similar zero-line modes also appear in the helical network description of minimally twisted bilayer graphene [32]. More generally, depending on the symmetries of the problem, 1D zero-line modes can also appear near line defects such as dislocations [33,34].

For 2D Dirac fermions with a periodic mass $M(x)$ alternating between positive and negative values, chiral 1D modes are located near the positions with $M(x) = 0$, with adjacent modes having opposite propagation direction. While low-energy transport remains efficient along the y direction, the band structure flattens along the x direction. For large mass amplitude (and assuming the same absolute value for positive and negative mass regions), the residual overlap between counterpropagating neighboring chiral modes generates a small velocity $v_x \ll v_F$ along the x direction. In effect, one then arrives at a highly anisotropic Dirac cone dispersion at low energies [35,36]. We here show that the case of a

piecewise constant periodic mass term is exactly solvable. Our calculations confirm the existence of anisotropic Dirac cones, yield analytical results for the ratio v_x/v_F, and provide a useful starting point for future studies of interaction effects and/or magnetic fields. We note that in Refs. [37,38], closely related models have been studied. In particular, the authors of Ref. [37] show that for smooth mass kinks, additional nonchiral localized states analogous to Volkov-Pankratov states [39,40] can exist. However, the anisotropy of the Dirac cone dispersion has not been discussed in Ref. [37]. Moreover, while Ref. [38] (see also Ref. [41]) contains a detailed discussion of the electronic spectrum for a periodic mass problem, their mass term alternates between zero and a finite value, in contrast to the mass term considered below. As a consequence, chiral zero modes and physical effects caused by these modes are absent in Refs. [38,41]. Let us also mention that we here study a coupled-wire model, see Refs. [42,43] for related but different examples, where the 1D wires correspond to chiral zero modes with alternating propagation direction [44].

A central result of our work is to point out the existence of *two types of boundary modes* in the presence of a sample boundary along the y direction. The modes are spatially confined to the vicinity of the boundary but can propagate along the boundary. Similarly, for an electrostatic potential step along the x direction, we predict two types of *interface modes*. The two different mode types emerge either near the center of the superlattice Brillouin zone (BZ) or near the BZ boundary. In the latter case, we observe that such modes appear only if the mass amplitude exceeds a critical value. Under this condition, the Fermi surface for the lowest band undergoes a Lifshitz transition [45], opening up from a closed elliptic contour into a pair of open (disconnected) arcs. Remarkably, both types of boundary and/or interface modes can only exist in the presence of the mass superlattice, and their spatial decay length can exceed the lattice constant of the mass term.

The structure of this paper is as follows. In Sec. II, we introduce the model and the assumptions behind it, and we consider the cases of a single mass kink and of a mass barrier. (Technical details have been relegated to the Appendix.) Next, in Sec. III we use the transfer matrix approach to determine the band structure and the Bloch states for a piecewise periodic mass term with alternating regions of mass $\pm M$; see Eq. (3.1) below. In this case, we find a gapless low-energy anisotropic Dirac cone near the Γ point of the superlattice BZ. However, if the positive and negative mass amplitudes differ, a spectral gap will open, as shown in Sec. III C, where we construct a systematic low-energy theory. Importantly, in the presence of boundaries or in an inhomogeneous electrostatic potential, the spectral condition also allows for evanescent wave solutions. We discuss boundary modes in Sec. IV. In Sec. V, we include an electrostatic potential step along the x direction, which defines an np junction. We determine the transmission probability for Bloch states and show that the conductance across the step will sensitively depend on the step position. This dependence is a direct consequence of the fact that low-energy states have significant weight only near the positions of mass (anti)kinks. In Sec. V C, we show that interface modes of various types can exist and we compute their energy dispersion. The paper concludes with an outlook in Sec. VI.

II. MODEL

In this paper, we study noninteracting electrons described by a 2D Dirac Hamiltonian with a single Dirac cone. This model captures the essential physics of the spin-momentum locked and protected surface states in 3D TI materials [18,19], as well as the low-energy physics of 2D graphene monolayers which is governed by states close to a single K point ("valley") [17]. For the latter case, the assumption of a single K point requires the mass or potential terms considered below to be actually smooth on the scale of the lattice spacing of graphene. For an infinitely extended system in the xy plane, using units with $\hbar = 1$ and Fermi velocity $v_F = 1$ throughout, we study the Hamiltonian

$$H = -i\sigma_x\partial_x - i\sigma_y\partial_y + M(x)\sigma_z + V(x)\mathbb{1}, \tag{2.1}$$

with the electrostatic potential $V(x)$ and the mass term $M(x)$. Both terms are assumed homogeneous along the y direction. As a consequence of this translation invariance, the wave vector (or momentum) component k_y is conserved. The Pauli matrices $\sigma_{x,y,z}$ and the 2×2 identity matrix $\mathbb{1}$ act in spin space for TI surface states, and in the sublattice space of the honeycomb lattice for the case of graphene.

For given momentum k_y, the spinor eigenstates of Eq. (2.1) can be written as

$$\Psi(x,y) = e^{ik_y y}\,\psi(x), \quad \psi(x) = \begin{pmatrix} u(x) \\ v(x) \end{pmatrix}, \tag{2.2}$$

which results in the 1D Dirac equation

$$\begin{pmatrix} M(x)+V(x) & -i(\partial_x + k_y) \\ -i(\partial_x - k_y) & -M(x)+V(x) \end{pmatrix}\begin{pmatrix} u \\ v \end{pmatrix} = E\begin{pmatrix} u \\ v \end{pmatrix}. \tag{2.3}$$

In this work, we are interested in the case of a spatially periodic mass term which alternates between positive and negative values. As a simple and exactly solvable model, we will consider the piecewise constant periodic mass term discussed in Sec. III. For the TI case, such a mass term can (approximately) be generated by the deposition of ferromagnetic insulator stripes with alternating magnetization on a TI surface, where the magnetic exchange contributions produce a periodic mass term [36]. Similarly, for a graphene monolayer, a suitably patterned substrate creates a sublattice-dependent superlattice potential which in effect gives a periodic mass term [17].

In the remainder of this section, to prepare the ground for the periodic mass case in Sec. III, we will analyze three simpler problems. In Sec. II A, we determine the general solution of Eq. (2.3) for the homogeneous case. In Sec. II B, we rederive the well-known low-energy spectrum for a mass kink, $M(x) = M\,\mathrm{sgn}(x)$, which binds a 1D chiral zero mode propagating along the y direction [18,20–22]. In Sec. II C, we study a mass barrier composed of a mass kink and an antikink, where one finds two counterpropagating chiral zero modes. For ease of notation, we often keep the dependence on k_y and E implicit.

A. Homogeneous problem

Let us first specify the general (not normalized) eigenstates of Eq. (2.3) for a region with constant potential, $V(x) = V$, and constant mass, $M(x) = M$. A uniform scalar potential

can be included by shifting $E \to E - V$, which we implicitly assume below. For $M(x) = M$, the solution is given by

$$\psi(x) = W_M(x)\begin{pmatrix} a \\ b \end{pmatrix}, \tag{2.4}$$

where a and b are arbitrary complex coefficients and we define the matrix

$$W_M(x) = \begin{pmatrix} e^{\kappa x} & e^{-\kappa x} \\ i\frac{k_y-\kappa}{M+E}e^{\kappa x} & i\frac{k_y+\kappa}{M+E}e^{-\kappa x} \end{pmatrix}, \tag{2.5}$$

with the definition

$$\kappa = \begin{cases} \sqrt{M^2 + k_y^2 - E^2}, & E^2 < k_y^2 + M^2, \\ ik \equiv i\sqrt{E^2 - M^2 - k_y^2}, & E^2 > k_y^2 + M^2. \end{cases} \tag{2.6}$$

For low energies, $E^2 < k_y^2 + M^2$, we have evanescent waves along the x direction, and the eigenstates are spatially localized on the length scale κ^{-1} near boundaries or mass kinks. For $E^2 > k_y^2 + M^2$, $\kappa = ik$ is purely imaginary and we find plane-wave solutions propagating along the x direction with wave number $k_x = k$. Useful expressions involving $W_M(x)$ in Eq. (2.5) are summarized in the Appendix. In particular, Eqs. (A3) and (A4) imply that the x component of the particle current density is given by

$$j_x = \psi^\dagger \sigma_x \psi = \begin{cases} \frac{4\kappa \mathrm{Im}(b^* a)}{M+E}, & E^2 < k_y^2 + M^2, \\ \frac{2k(|a|^2 - |b|^2)}{M+E}, & E^2 > k_y^2 + M^2. \end{cases} \tag{2.7}$$

B. Mass kink

We turn to the case of a single mass kink, $M(x) = M\,\mathrm{sgn}(x)$ with $M > 0$; see Ref. [22]. We here discuss only the low-energy case, $E^2 < k_y^2 + M^2$, where κ in Eq. (2.6) is real. From Eq. (2.4), normalizable eigenstates then have the form

$$\psi(x) = \begin{cases} W_{-M}(x)\begin{pmatrix} a_L \\ 0 \end{pmatrix}, & \text{for } x < 0, \\ W_M(x)\begin{pmatrix} 0 \\ b_R \end{pmatrix}, & \text{for } x > 0, \end{cases} \tag{2.8}$$

where the coefficients a_L and b_R are determined by continuity of $\psi(x)$ at $x = 0$ and normalization. Using Eq. (A2), we define the matrix

$$\begin{aligned} \Omega_M &= W_M^{-1}(0)\, W_{-M}(0) \\ &= \frac{1}{\kappa(E-M)}\begin{pmatrix} E\kappa - k_y M & -(\kappa + k_y)M \\ (-\kappa + k_y)M & E\kappa + k_y M \end{pmatrix}, \end{aligned} \tag{2.9}$$

such that the continuity condition takes the form

$$\begin{pmatrix} 0 \\ b_R \end{pmatrix} = \Omega_M \begin{pmatrix} a_L \\ 0 \end{pmatrix}. \tag{2.10}$$

As a result, we get the relations $0 = (E\kappa - k_y M)a_L$ and $b_R = \frac{(-\kappa+k_y)M}{\kappa(E-M)}a_L$. For nontrivial solutions, we must have $E\kappa - k_y M = 0$ from the first relation, which is solved by the dispersion relation $E(k_y) = k_y$ of a 1D chiral mode. The second relation then yields $b_R = a_L$ for the spinor wave function, where a_L is finally determined by normalization. This chiral mode propagates with velocity v_F along the positive y direction and is localized near the mass kink at $x = 0$ in the x direction. Similarly, for an antikink mass profile with M replaced by $-M$, one finds a 1D chiral mode propagating along the negative y direction, with dispersion relation $E(k_y) = -k_y$.

C. Mass barrier

Next we consider a mass barrier of width ℓ described by [27]

$$M(x) = \begin{cases} M, & \text{for } |x| < \ell/2, \\ -M, & \text{for } |x| > \ell/2. \end{cases} \tag{2.11}$$

We search for low-energy solutions with $E^2 < k_y^2 + M^2$, where normalizable eigenstates can be written as

$$\psi(x) = \begin{cases} W_{-M}(x)\begin{pmatrix} a_L \\ 0 \end{pmatrix}, & \text{for } x < -\ell/2, \\ W_M(x)\begin{pmatrix} a \\ b \end{pmatrix}, & \text{for } |x| < \ell/2, \\ W_{-M}(x)\begin{pmatrix} 0 \\ b_R \end{pmatrix}, & \text{for } x > \ell/2, \end{cases} \tag{2.12}$$

with coefficients a_L, a, b, and b_R. Imposing continuity at $x = \pm\ell/2$, one can eliminate a and b. We arrive at Eq. (2.10) but with Ω_M replaced by

$$\Omega_B = W_{-M}^{-1}(\ell/2)\, W_M(\ell/2)\, W_M^{-1}(-\ell/2)\, W_{-M}(-\ell/2); \tag{2.13}$$

see Eq. (A5) for explicit matrix elements. The dispersion relation follows from $[\Omega_B]_{11} = 0$, which reads explicitly

$$E^2 = k_y^2 + M^2 e^{-2\kappa\ell}. \tag{2.14}$$

For barrier width $\ell \to \infty$, we can neglect the exponential term and obtain $E_\pm(k_y) = \pm k_y$, corresponding to a pair of counterpropagating chiral zero modes localized at the barrier edges. For large but finite barrier width with $M\ell \gg 1$, the two chiral zero modes hybridize. The level crossing at $k_y = 0$ is now replaced by an avoided crossing, where Eq. (2.14) yields $E_\pm(k_y = 0) \simeq \pm M e^{-\ell M}$. The low-energy dispersion then acquires an exponentially small gap due to the avoided crossing, $E_\pm(k_y) \simeq \pm\sqrt{k_y^2 + M^2 e^{-2M\ell}}$.

III. PERIODIC MASS

In this section, we discuss the solution of the Dirac equation (2.3) for the piecewise constant periodic mass term sketched in Fig. 1, which is given by

$$M(x) = \begin{cases} +M, & jd \leqslant x < (j + \frac{1}{2})d, \\ -M, & (j + \frac{1}{2})d \leqslant x < (j+1)d, \end{cases} \tag{3.1}$$

where d is the lattice period and $j \in \mathbb{Z}$ labels the unit cell. For simplicity, we here assumed that the regions of positive and negative mass have the same spatial extent, $\ell \equiv d/2$, and the same absolute value of the mass, $|M(x)| = M$. This implies the symmetry $M(x + \ell) = -M(x)$. Our calculations can easily be adapted to the general case, where we find that the spectrum acquires a gap; see Sec. III C. For now, however, let us focus on Eq. (3.1). In Sec. III A, we employ the transfer matrix method to solve the spectral problem and, in particular, to derive the energy quantization condition. The band structure and the corresponding Bloch states are described in Sec. III B, while we postpone the discussion of evanescent

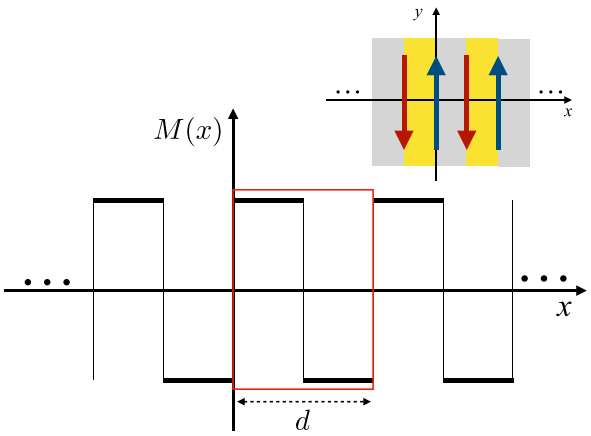

FIG. 1. Piecewise constant periodic mass profile $M(x)$ in Eq. (3.1). A unit cell of length d is indicated by the red square. The inset indicates the regions of positive (gray) and negative (yellow) mass in the xy plane. 1D chiral zero modes are generated near the (anti)kink positions by the Jackiw-Rebbi mechanism, with the respective propagation direction indicated by arrows.

state solutions to Sec. IV. Finally, in Sec. III C, a systematic low-energy theory is constructed by projecting the model to the subspace spanned by the chiral zero modes.

A. Transfer matrix and spectral equation

We first consider the unit cell $0 < x < d$, where $\psi(d)$ and $\psi(0)$ are connected by the transfer matrix T,

$$\psi(d) = T\,\psi(0). \tag{3.2}$$

In this unit cell, Eq. (2.4) implies that the wave function has the form

$$\psi(x) = \begin{cases} W_M(x)\begin{pmatrix} a_1 \\ b_1 \end{pmatrix}, & \text{for } 0 < x < \ell, \\ W_{-M}(x)\begin{pmatrix} a_2 \\ b_2 \end{pmatrix}, & \text{for } \ell < x < d, \end{cases} \tag{3.3}$$

with $W_{\pm M}(x)$ in Eq. (2.5). The continuity of $\psi(x)$ at $x = \ell$ relates the complex coefficients (a_2, b_2) and (a_1, b_1) according to

$$\begin{pmatrix} a_2 \\ b_2 \end{pmatrix} = W_{-M}^{-1}(\ell)\,W_M(\ell)\begin{pmatrix} a_1 \\ b_1 \end{pmatrix}, \tag{3.4}$$

with $W_{-M}^{-1}(\ell)\,W_M(\ell)$ given in Eq. (A2). We can therefore express the transfer matrix as

$$T = W_{-M}(d)\,W_{-M}^{-1}(\ell)\,W_M(\ell)\,W_M^{-1}(0). \tag{3.5}$$

The explicit form of the matrix elements of T is given by Eq. (A7) in the Appendix. The matrix T is symmetric and has $\det T = 1$. Its eigenvalues can be written as $\lambda_\pm = e^{\pm iKd}$, where K can be interpreted as a quasimomentum along the x direction. As discussed below, K can be either real-valued (for Bloch waves) or complex-valued (for evanescent modes).

In what follows, instead of T, we find it more convenient to use a modified transfer matrix Ω defined by

$$T = W_M(0)\,\Omega\,W_M^{-1}(0). \tag{3.6}$$

Using Eq. (3.5) and the relations $\psi(0) = W_M(0)\binom{a_1}{b_1}$ and $\psi(d) = W_{-M}(d)\binom{a_2}{b_2}$, which follow from Eq. (3.3), we arrive at[1]

$$\Omega = W_M^{-1}(0)\,W_{-M}(d)\,W_{-M}^{-1}(\ell)\,W_M(\ell). \tag{3.7}$$

The corresponding matrix elements are specified in Eq. (A6). We again have $\det\Omega = 1$, and Ω has the same eigenvalues $\lambda_\pm = e^{\pm iKd}$ as T.

We next require that $\psi(x)$ satisfy the Bloch periodicity condition

$$\psi(x + d) = e^{iKd}\,\psi(x), \tag{3.8}$$

with a quasimomentum K along the x direction. For Bloch wave solutions, K must be real. We then take K from the first BZ of the mass superlattice,

$$-\frac{\pi}{d} < K \leqslant \frac{\pi}{d}, \tag{3.9}$$

where $(K, k_y) = (0, 0)$ is the "Γ point." More generally, we can impose Eq. (3.8) for complex values of K. We find three possible types of solutions, where K is either real (Bloch waves) or complex (evanescent waves), with $K = \pm i\mathcal{K}$ or $K = \mp i\mathcal{K} \pm \pi/d$. The inverse length scale $\mathcal{K} > 0$ is determined below. Evanescent state solutions thus are obtained by imposing either

$$\psi(x + d) = e^{\mp\mathcal{K}d}\,\psi(x) \tag{3.10}$$

or

$$\psi(x + d) = -e^{\pm\mathcal{K}d}\,\psi(x). \tag{3.11}$$

In what follows, evanescent waves derived from Eqs. (3.10) and (3.11) are denoted as "type-I" and "type-II" states, respectively. While for the infinitely extended system evanescent states are not normalizable and hence not admissible, they emerge in the presence of boundaries or nonuniform potentials; see Secs. IV and V C.

Setting $x = 0$ and using the transfer matrix, Eq. (3.8) is next written as

$$W_M(0)\,\Omega\,W_M^{-1}(0)\,\psi(0) = e^{iKd}\psi(0), \tag{3.12}$$

which is equivalent to the condition

$$\left(\Omega - e^{iKd}\,\mathbb{1}\right)\begin{pmatrix} a_1 \\ b_1 \end{pmatrix} = \begin{pmatrix} 0 \\ 0 \end{pmatrix}. \tag{3.13}$$

Nontrivial solutions of Eq. (3.13) can only exist if

$$\det\left(\Omega - e^{iKd}\,\mathbb{1}\right) = 0. \tag{3.14}$$

The compatibility condition (3.14) is equivalent to the spectral equation

$$f(\xi) = \cos(Kd), \tag{3.15}$$

[1]With the matrix $D(x) = \mathrm{diag}(e^{\kappa x}, e^{-\kappa x})$ and the matrix Ω_M for the single-kink problem in Eq. (2.9), we may express Ω as $\Omega = \Omega_M\,D(\ell)\,\Omega_M^{-1}\,D(\ell)$. This establishes a relation between the single-kink problem and the periodic problem.

where we define $f(\xi) \equiv \frac{1}{2}\mathrm{Tr}\,\Omega(\xi)$ with the dimensionless variable

$$\xi = \left(k_y^2 - E^2\right)d^2. \tag{3.16}$$

Using Eq. (A6), one finds

$$f(\xi) = \frac{(Md)^2 + \xi\cosh(\sqrt{(Md)^2+\xi})}{(Md)^2+\xi}. \tag{3.17}$$

The spectral equation thus depends on the single dimensionless parameter Md, and E and k_y appear only through the dimensionless variable ξ. Below, we mostly focus on the low-energy regime, subject to the condition

$$|E| < M, \tag{3.18}$$

such that $\xi > -(Md)^2$. The function $f(\xi)$ is shown for several values of Md in Fig. 2(a). Bloch states are possible for $-1 \leqslant f(\xi) \leqslant 1$ corresponding to $\xi_c \leqslant \xi \leqslant 0$, where $\xi_c < 0$ is defined by the condition $f(\xi_c) = -1$. Outside this window, no real solutions for the quasimomentum K can be found. However, Eq. (3.15) also allows for solutions with complex-valued K. For $f(\xi) > 1$, corresponding to $\xi > 0$ and therefore $|E| < |k_y|$, we obtain type-I evanescent states. On the other hand, for $\xi < \xi_c$, we can have type-II evanescent states at energies above a critical value, $|E| > E_c$ with $E_c d = \sqrt{-\xi_c}$, where we find the analytical estimate

$$E_c d \approx \begin{cases} 3 - Md/2, & Md \approx 2, \\ 2Mde^{-Md/2}, & Md \gg 1. \end{cases} \tag{3.19}$$

In the low-energy regime (3.18), solutions for ξ_c, and thus type-II states, exist only for $Md > 2$. This is related to the fact that if $Md < 2$, for any Fermi level $|E_\mathrm{F}| < M$, the Fermi surface is a closed curve in the 2D BZ. If $Md > 2$, instead, the Fermi surface evolves from a closed curve (for $|E_\mathrm{F}| < E_c$) into a pair of disconnected arcs (for $E_c < |E_\mathrm{F}| < M$). The critical point $|E_\mathrm{F}| = E_c$ corresponds to a Lifshitz transition. Numerical results for E_c vs Md along with the estimates in Eq. (3.19) are shown in the inset of Fig. 2(a). For large $Md \gg 1$, type-II states are also realized at very low energies.

We discuss type-I and type-II states in more detail in Sec. IV and focus on Bloch states with real K for the remainder of this section. We note in passing that Eq. (3.15) has also been specified in Ref. [37]. However, the solutions $E = \pm\sqrt{k_y^2 + M^2}$ reported in Ref. [37] are spurious, and the anisotropy of the emergent Dirac cone near the Γ point has been missed; see Eq. (3.25) below. It is also worth mentioning that for $k_y = 0$, Eq. (3.15) coincides with the spectral equation for a generalized Kronig-Penney model of diatomic crystals [46,47].

B. Band structure and Bloch states

We first study the solutions of the spectral condition (3.15) for real quasimomenta K in the 1D BZ (3.9). The corresponding Bloch bands form the band structure of the mass superlattice. For computing the band structure and the group velocities, it is convenient to introduce the auxiliary function

$$\Phi(E, K, k_y) = f\left(\left(k_y^2 - E^2\right)d^2\right) - \cos(Kd), \tag{3.20}$$

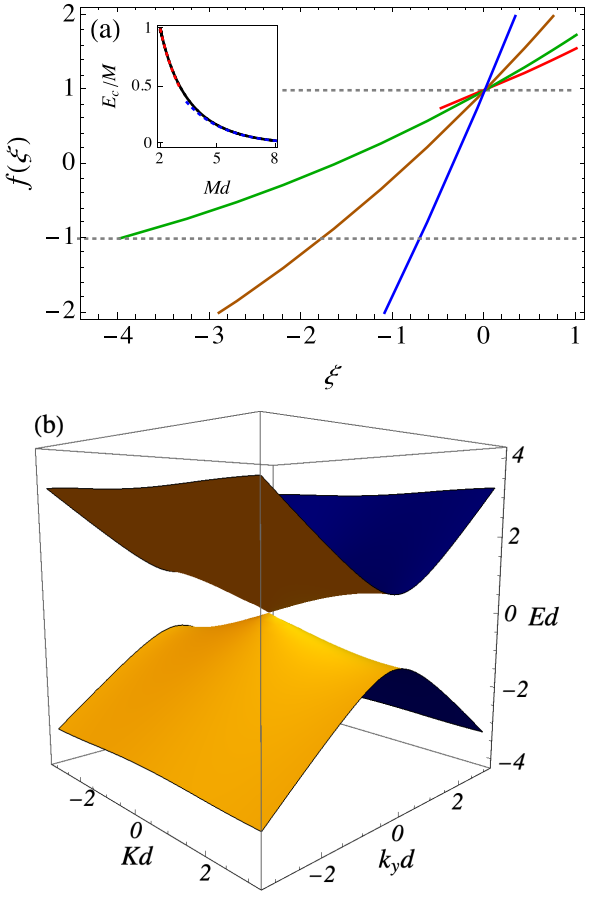

FIG. 2. Spectrum of the 2D Dirac Hamiltonian with the periodic mass term (3.1). (a) The function $f(\xi)$ vs ξ, see Eq. (3.17), in the regime $\xi > -(Md)^2$, for $Md = 0.7, 2, 3.5$, and 5, corresponding to the red, green, brown, and blue curves, respectively. According to Eq. (3.15), Bloch states require $|f(\xi)| \leqslant 1$. For $f(\xi) > 1$ [$f(\xi) < -1$], type-I [type-II] evanescent states are possible. Inset: Critical energy E_c vs Md, where type-II states can only exist for $|E| > E_c$. The solid curve gives numerically exact results. The red and blue dotted curves give the analytical estimates (3.19) for $Md \approx 2$ and $Md \gg 1$, respectively. (b) Low-energy band structure, $E = \pm E_n(K, k_y)$, for Bloch states with $n = 0$ and $Md = 5$.

where Eq. (3.15) is equivalent to the condition $\Phi(E, K, k_y) = 0$. The band structure calculation amounts to finding the implicit function $E(K, k_y)$ defined by this condition. In limiting cases, this can be done analytically (see below), but in general one has to resort to numerics. In any case, one finds a particle-hole symmetric spectrum, $E = \pm E_n(K, k_y)$, where $n \in \mathbb{Z}$ labels different bands with non-negative energy $E_n(K, k_y)$. The group velocity (v_x, v_y) for a given eigenstate follows with $E = \pm E_n(K, k_y)$ from Eq. (3.20) as

$$v_x = -\frac{\partial_K \Phi}{\partial_E \Phi}, \quad v_y = -\frac{\partial_{k_y} \Phi}{\partial_E \Phi}. \tag{3.21}$$

The low-energy spectrum determined numerically is shown in Fig. 2(b). To understand these results, we now examine limiting cases where analytical progress is possible.

First, for $Md \to 0$, Eq. (3.15) recovers the standard isotropic massless Dirac cone with $k_x = K$ restricted to the first BZ (3.9),

$$E = \pm E_n(K, k_y) = \pm\sqrt{(K + 2\pi n/d)^2 + k_y^2}, \tag{3.22}$$

which includes an isolated Dirac node at zero energy as well as finite-energy crossing points for $K = 0$, because $E_n(0, k_y) = E_{-n}(0, k_y)$, and for $K = \frac{\pi}{d}$, because $E_n(\frac{\pi}{d}, k_y) = E_{-n-1}(\frac{\pi}{d}, k_y)$. The finite-energy crossings points are not isolated but form lines when varying k_y. We will show next that a finite value of Md does not spoil the above nodal structures at the center of the 1D BZ, but it does lift the degeneracies at the BZ boundary where gaps open.

For finite Md, let us first consider the 1D BZ center $K = 0$. We then find that Eq. (3.15) has the non-negative solutions

$$E_0(0, k_y) = |k_y|, \quad E_{n\neq 0}(0, k_y) = \sqrt{k_y^2 + \left(\frac{2\pi n}{d}\right)^2 + M^2}, \tag{3.23}$$

where each energy $E_{n\neq 0}(0, k_y)$ is twofold degenerate due to $\pm n$ bands. However, this degeneracy is lifted for $K \neq 0$; see Eq. (3.27) below. From Eq. (3.23), using $E_n^{(c)} \equiv E_n(0, 0)$ for the Γ-point energy of the respective band, Γ-point crossings occur at zero energy ($n = 0$) and at the finite energies $\pm E_{n\neq 0}^{(c)}$ with

$$E_{n\neq 0}^{(c)} = \sqrt{M^2 + (2\pi n/d)^2}. \tag{3.24}$$

The zero-energy node is of special interest. By expanding Eq. (3.15) for small energies and small momenta, one obtains an *anisotropic* conical Dirac dispersion,

$$E = \pm E_{n=0}(K, k_y) \simeq \pm\sqrt{v_{x,0}^2 K^2 + v_F^2 k_y^2}, \tag{3.25}$$

with a renormalized velocity along the x direction,

$$\frac{v_{x,0}}{v_F} = \frac{Md/2}{\sinh(Md/2)}. \tag{3.26}$$

Numerical results for the full low-energy band structure are shown in Fig. 2(b). Near the Γ point, they agree with Eq. (3.25). Evidently, for $Md \to 0$, Eqs. (3.25) and (3.26) recover the isotropic Dirac cone in Eq. (3.22). For $Md \gg 1$, however, $v_{x,0}/v_F$ is exponentially small and the dispersion becomes almost flat in the K direction. In this case, the individual mass kinks and antikinks in the periodic mass profile (3.1), which are centered at $x = jd/2$ with integer j, bind 1D chiral zero modes by means of the Jackiw-Rebbi mechanism, see Sec. II. As we elaborate in Sec. III C, superpositions of chiral zero modes generate the $n = 0$ band dispersion (3.25), where the finite hybridization between the counterpropagating zero modes at neighboring mass kinks and antikinks is responsible for the finite but exponentially small velocity (3.26). While the anisotropic Dirac cone dispersion associated with zero modes in periodic mass profiles has been discussed before [36], the piecewise constant mass term (3.1) admits an exact solution. We note that anisotropic Dirac cones can alternatively be engineered by means of scalar superlattice potentials [1,2,4,7,8] or by using periodic magnetic fields [13–15].

Similarly, we may expand around the Γ point for the finite-energy crossing points (3.24), where we obtain

$$E_{n\neq 0}(K, k_y) \simeq E_n^{(c)} + \frac{k_y^2}{2E_n^{(c)}} + \mathrm{sgn}(n)\, v_{x,n} K, \tag{3.27}$$

with the velocities $v_{x,n\neq 0} = [2\pi n/(E_n^{(c)} d)]^2$ along the x direction. We observe that a finite k_y does not lift the twofold degeneracy at $K = 0$, and hence there is a nodal line.

Let us briefly compare the above results to the corresponding uniform-mass case $M(x) = M$, where the band structure is given by

$$E = \pm E_n^{(u)}(K, k_y) = \pm\sqrt{M^2 + (K + 2\pi n/d)^2 + k_y^2}. \tag{3.28}$$

Importantly, no zero-energy modes related to the anisotropic Dirac cone (3.25) appear anymore in Eq. (3.28). Expanding around the Γ point, where finite-energy crossings occur again at $E = \pm E_{n\neq 0}^{(c)}$ with $E_n^{(c)}$ in Eq. (3.24), we find the positive-energy solutions

$$E_0^{(u)}(K, k_y) \simeq M + \frac{k_y^2 + K^2}{2M}, \tag{3.29}$$

$$E_{n\neq 0}^{(u)}(K, k_y) \simeq E_n^{(c)} + \frac{k_y^2}{2E_n^{(c)}} + \mathrm{sgn}(n)\, \tilde{v}_{x,n} K,$$

with $\tilde{v}_{x,n} = 2\pi|n|/(E_n^{(c)} d)$. The main difference between the alternating and the uniform mass profile is that the $n = 0$ zero-mode band in Eq. (3.25) has shifted to finite energies $E_0^{(u)}(K, k_y) \geqslant M$. On the other hand, the $n \neq 0$ dispersion relation (3.29) differs from Eq. (3.27) only with respect to the velocity along the x direction, $v_{x,n} \to \tilde{v}_{x,n}$.

Let us now turn to the Bloch eigenstates corresponding to the above band structure. Keeping (E, k_y) implicit, we begin by expressing $\psi(x)$ in terms of a spinor wave function $u_K(x)$ with the periodicity of the mass superlattice,

$$\psi(x) = e^{iKx} u_K(x), \quad u_K(x + d) = u_K(x). \tag{3.30}$$

In the unit cell $0 < x < d$, we obtain $u_K(x) = e^{-iKx}\psi(x)$ from $\psi(x)$ as specified in Eq. (3.3). We then need to determine the K-dependent coefficients (a_1, b_1) and (a_2, b_2) in Eq. (3.3). To that end, we recall that (a_2, b_2) follows from (a_1, b_1) by the continuity condition (3.4) imposed at $x = d/2$. Using Eq. (3.13), we can express[2] b_1 in terms of a_1,

$$b_1(K) = \frac{e^{iKd} - \Omega_{11}}{\Omega_{12}} a_1, \tag{3.31}$$

with the matrix elements of Ω in Eq. (A6). Finally, a_1 is fixed by the normalization condition

$$\int_0^d dx\, |u_K(x)|^2 = 1. \tag{3.32}$$

[2]For $K = 0$, the matrix element Ω_{12} vanishes for the spectral branches $\pm E_0(0, k_y) = k_y$. Then Eq. (3.31) does not apply and we have instead $a_1 = 0$ with b_1 determined by normalization.

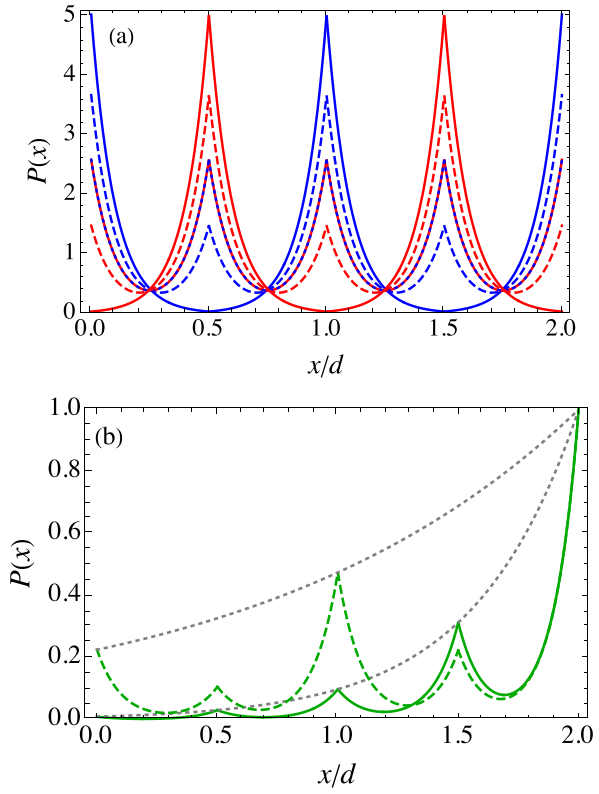

FIG. 3. Probability density $P(x)$ vs x for selected eigenstates of the periodic mass problem. (a) $P(x)$ for Bloch states with band index $n = 0$, taking $Md = 5$ and $Ed = 0.7$. Solid blue, dashed blue, blue-red, dashed red, and solid red curves are for $k_y d = 0.7, 0.3, 0, -0.3, -0.7$, respectively. (b) $P(x)$ normalized to its value at $x = 2d$, for type-II evanescent states with $Md = 5$ and $Ed = 1$. Solid (dashed) green curves are for $k_y d = 0$ ($k_y d = 0.3$), while the dotted gray lines show the corresponding graphs of $e^{\mathcal{K}x}$.

We thereby obtain the Bloch eigenstate $\Psi_{K,k_y,n,\pm}(x, y) = e^{i(Kx+k_y y)} u_{K,k_y,n,\pm}(x)$ for the energy $E = \pm E_n(K, k_y)$. We illustrate the corresponding probability densities in Fig. 3(a). For $k_y d = 0.7$ (solid blue curve), the state is mainly localized near the mass kinks at $x = jd$ with integer j. For $k_y d = -0.7$ (solid red curve), on the other hand, the state is localized near the antikinks at $x = (j + 1/2)d$. As $|k_y d|$ decreases, one approaches the $d/2$-periodic probability density found for $k_y = 0$, where the eigenstate is an equal-weight superposition of counterpropagating chiral Jackiw-Rebbi modes.

For $E^2 < k_y^2 + M^2$ (where κ is real), we now observe that the particle current density (2.7) along the x direction is uniform and given by

$$j_x = \frac{-4\kappa \sin(Kd)}{(M+E)\Omega_{12}} |a_1|^2, \tag{3.33}$$

with a_1 determined by Eq. (3.32). Note that j_x is odd in K. We note that for the scattering problem in Sec. V A, instead of Eq. (3.32) it will be more convenient to adopt a normalization where the wave function carries unit current. This is achieved by setting

$$|a_1|^2 = \left| \frac{(M+E)\Omega_{12}}{-4\kappa \sin(Kd)} \right|, \tag{3.34}$$

which determines a_1, with $|a_1(-K)|^2 = |a_1(K)|^2$, up to an irrelevant phase.

C. Effective low-energy theory

For $Md \gg 1$, the essential low-energy physics of the staggered Dirac mass superlattice problem is captured by projecting the full Hamiltonian (2.1) onto the subspace spanned by the 1D chiral zero modes centered at the (anti)kink positions $x_j = jd/2$ (integer j) of the periodic mass term (3.1). The resulting effective low-energy theory is also useful for studying interacting variants of the model. We show below that this projection reproduces the exact spectrum to exponential accuracy in the low-energy regime, $|E| < M$.

In the unit cell $|x| < \ell$ obtained after shifting $x \to x - \frac{\ell}{2}$, we start from the mass profile

$$M(x) = \begin{cases} (1+\gamma)M, & |x| < \frac{\ell}{2}, \\ -(1-\gamma)M, & \frac{\ell}{2} < |x| < \ell, \end{cases} \tag{3.35}$$

where $M > 0$. The full mass profile follows by periodicity, $M(x + jd) = M(x)$, and is inversion symmetric, $M(x) = M(-x)$. We here allow for a dimensionless asymmetry parameter γ, resulting in different mass amplitudes in regions of positive and negative mass. Note that Eq. (3.1) follows (up to the above shift) from Eq. (3.35) for $\gamma = 0$, where we also have $M(x + \ell) = -M(x)$. The latter property is lost for $\gamma \neq 0$. For $|\gamma| > 1$, the mass term always has the same sign and chiral zero modes are absent. Below we focus on the more interesting case $|\gamma| < 1$.

The kink and antikink positions in $M(x)$ define a 1D bipartite lattice in the x direction, where sublattice A (kinks) comprises the sites at $x_{Aj} = jd - \frac{\ell}{2}$ and sublattice B (antikinks) refers to $x_{Bj} = jd + \frac{\ell}{2}$. We now introduce the mass profile $\mathcal{M}_{\rm K}(x - x_A)$ for a single kink centered at position x_A, and similarly $\bar{\mathcal{M}}_{\rm K}(x - x_B)$ for an antikink centered at x_B, where

$$\mathcal{M}_{\rm K}(x) = M\mathrm{sgn}(x) + \gamma M, \quad \bar{\mathcal{M}}_{\rm K}(x) = \mathcal{M}_{\rm K}(-x). \tag{3.36}$$

Zero-energy fermion modes bound to a kink or an antikink at $x = 0$ satisfy

$$\begin{aligned} [-i\sigma_x \partial_x + \mathcal{M}_K(x)\sigma_z]\phi_+(x) &= 0, \\ [-i\sigma_x \partial_x + \bar{\mathcal{M}}_K(x)\sigma_z]\phi_-(x) &= 0, \end{aligned} \tag{3.37}$$

where the orthonormalized states $\phi_\pm(x)$ are eigenstates of σ_y and satisfy $\phi_-(x) = \sigma_z \phi_+(-x)$. Defining $\tilde{M} = (1 - \gamma^2)M$, we find

$$\phi_\pm(x) = \sqrt{\frac{\tilde{M}}{2}}\, e^{-F(\pm x)} \begin{pmatrix} 1 \\ \pm i \end{pmatrix}, \quad F(x) = (|x| + \gamma x)M. \tag{3.38}$$

For constructing the low-energy theory for $Md \gg 1$, we expand the electron field operator in terms of the zero modes (3.38) for kink and antikinks centered at x_{Aj} and x_{Bj},

respectively,

$$\hat{\Psi}(x,y) = \sum_j [\phi_+(x - x_{Aj})\,\hat{\psi}_{Aj}(y) + \phi_-(x - x_{Bj})\,\hat{\psi}_{Bj}(y)] \tag{3.39}$$

with 1D chiral fermion field operators $\hat{\psi}_{\alpha j}(y)$ for each sublattice $\alpha = A, B$ and each unit cell $j \in \mathbb{Z}$ of the 1D bipartite lattice. With fermion operators $c_{\alpha j k_y}$, we have $\hat{\psi}_{\alpha j}(y) = \frac{1}{\sqrt{W}} \sum_{k_y} e^{ik_y y} c_{\alpha j k_y}$, using periodic boundary conditions, $\hat{\psi}_{\alpha j}(y + W) = \hat{\psi}_{\alpha j}(y)$, such that $k_y = \frac{2\pi m}{W}$ for integer m and linear system size W.

Projecting the full Hamiltonian H, see Eq. (2.1) with $V(x) = 0$ and $M(x)$ in Eq. (3.35), onto the low-energy basis (3.39), we obtain the effective low-energy Hamiltonian,

$$\begin{aligned} H_{\text{eff}} &= \int dx dy\, \hat{\Psi}^\dagger(x,y) H \hat{\Psi}(x,y) \\ &= \sum_{\alpha\alpha', jj', k_y} c^\dagger_{\alpha j k_y} \mathcal{H}^{\alpha\alpha'}_{jj'}(k_y)\, c_{\alpha' j' k_y}, \end{aligned} \tag{3.40}$$

with the sublattice-diagonal matrix elements

$$\begin{aligned} \mathcal{H}^{AA}_{jj'}(k_y) &= k_y \tilde{M} \int dx\, e^{-F(x - x_{Aj}) - F(x - x_{Aj'})}, \\ \mathcal{H}^{BB}_{jj'}(k_y) &= -k_y \tilde{M} \int dx\, e^{-F(-x + x_{Bj}) - F(-x + x_{Bj'})}. \end{aligned} \tag{3.41}$$

Similarly, the off-diagonal components take the form

$$\begin{aligned} \mathcal{H}^{AB}_{jj'}(k_y) = \mathcal{H}^{BA}_{j'j}(k_y) &= \int dx\, e^{-F(x - x_{Aj}) - F(-x + x_{Bj'})} \\ &\times \tilde{M}[M(x) - \bar{\mathcal{M}}_{\text{K}}(x - x_{Bj'})]. \end{aligned} \tag{3.42}$$

All matrix elements depend on the site indices j and j' only through their separation $(j - j')d$ and decay exponentially with this distance. In particular, Eq. (3.41) yields

$$\mathcal{H}^{AA}_{jj'}(k_y) = -\mathcal{H}^{BB}_{jj'}(k_y) = k_y f_{|j-j'|}, \tag{3.43}$$

where the dimensionless numbers ($l = 0, 1, 2, \ldots$)

$$f_l = \left(\cosh(\gamma l M d) + \frac{\sinh(\gamma l M d)}{\gamma}\right) e^{-lMd} \tag{3.44}$$

encode the overlap between zero-energy modes at distance ld belonging to the same sublattice. Note that $f_0 = 1$. The off-diagonal matrix elements (3.42) do not depend on k_y and can similarly be expressed as

$$\mathcal{H}^{AB}_{jj'}(k_y) = M g_{j-j'}, \tag{3.45}$$

where the dimensionless numbers g_m, with $m \in \mathbb{Z}$ and $M(x)$ in Eq. (3.35), are given by

$$\begin{aligned} g_m &= \tilde{M} d\, e^{\gamma(m - \frac{1}{2})Md} \int ds\, e^{-(|s| + |s - m + \frac{1}{2}|)Md} \\ &\times \left(\frac{M(s + \frac{1}{4})}{M} + \text{sgn}(s) - \gamma\right). \end{aligned} \tag{3.46}$$

Note that for $\gamma = 0$, we have $g_m = -g_{1-m}$. For $Md \gg 1$, the numbers f_l and g_m decrease exponentially fast when increasing l and $|m|$, respectively. The low-energy theory is dominated by terms with $f_{l=0} = 1$ and $g_{m=0,1}$, corresponding

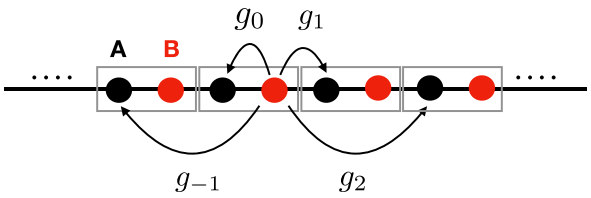

FIG. 4. Illustration of the numbers g_m in Eq. (3.46), which encode the overlap between counterpropagating chiral zero modes. The sites A and B correspond to the 1D bipartite lattice of kink and antikink positions, where rectangles indicate a unit cell.

to overlaps between at most adjacent sites of the 1D bipartite lattice, as illustrated in Fig. 4. In particular, the couplings g_{-1} and g_2 describe next-nearest-neighbor overlap integrals which are exponentially small compared to the nearest-neighbor couplings $g_{0,1}$, and can be omitted. For $m = 0, 1$, the integral in Eq. (3.46) can be evaluated to exponential accuracy,

$$g_0 \approx -(1 - \gamma^2) e^{-(1+\gamma)\frac{Md}{2}}, \quad g_1 \approx (1 - \gamma^2) e^{-(1-\gamma)\frac{Md}{2}}. \tag{3.47}$$

Since the matrix elements $\mathcal{H}^{\alpha\alpha'}_{jj'}(k_y)$ only depend on the separation $(j - j')d$, the low-energy Hamiltonian (3.40) is diagonal in momentum space. Using the above chiral 1D fermion operators $c_{\alpha j k_y}$, we define a momentum-space spinor field $C_{K k_y}$ according to

$$\begin{pmatrix} c_{Aj k_y} \\ c_{Bj k_y} \end{pmatrix} = \int_{-\pi/d}^{\pi/d} \frac{dK}{2\pi} e^{ijKd} C_{K k_y}, \quad C_{K k_y} = \begin{pmatrix} C_{AK k_y} \\ C_{BK k_y} \end{pmatrix}. \tag{3.48}$$

For $W \to \infty$, we then obtain

$$H_{\text{eff}} = \int \frac{dK dk_y}{(2\pi)^2} C^\dagger_{K k_y} \tilde{\mathcal{H}}(K, k_y) C_{K k_y}, \tag{3.49}$$

where the single-particle effective Hamiltonian,

$$\tilde{\mathcal{H}}(K, k_y) = \begin{pmatrix} \tilde{f}(K) k_y & \tilde{g}(K) M \\ \tilde{g}^*(K) M & -\tilde{f}(K) k_y \end{pmatrix}, \tag{3.50}$$

is expressed in terms of the Fourier series

$$\begin{aligned} \tilde{f}(K) &= f_0 + 2 \sum_{l=1}^{\infty} f_l \cos(lKd) \approx 1, \\ \tilde{g}(K) &= \sum_m g_m e^{-imKd} \approx g_0 + g_1 e^{-iKd}. \end{aligned} \tag{3.51}$$

The approximate results in Eq. (3.51) are obtained by keeping only the leading coefficients $f_{l=0} = 1$ and $g_{m=0,1}$, and hold to exponential accuracy for $Md \gg 1$. By diagonalizing $\tilde{\mathcal{H}}(K, k_y)$ with the approximations in Eq. (3.51), we obtain the eigenenergies

$$E(K, k_y) = \pm \sqrt{k_y^2 + M^2 \left[g_0^2 + g_1^2 + 2 g_0 g_1 \cos(Kd)\right]}. \tag{3.52}$$

This expression accurately reproduces the $n = 0$ band obtained from the exact spectral equation (3.15).

Close to the Γ point ($Kd \ll 1$), Eq. (3.50) reduces to

$$\tilde{\mathcal{H}}(K, k_y) = M g_1 K d\, \tau_y + k_y \tau_z - \left(\Delta + \tfrac{1}{2} M g_1 (Kd)^2\right) \tau_x, \tag{3.53}$$

with the gap $\Delta = -(g_0 + g_1)M > 0$ and Pauli matrices τ_a in sublattice space for the 1D bipartite lattice. Equation (3.52) then simplifies to the dispersion relation of anisotropic massive Dirac fermions,

$$E(K, k_y) = \pm\sqrt{\tilde{v}_x^2 K^2 + v_F^2 k_y^2 + \Delta^2}, \tag{3.54}$$

with

$$\Delta = 2\tilde{M}\, e^{-Md/2} \sinh(\gamma Md/2), \quad \frac{\tilde{v}_x}{v_F} = \tilde{M} d\, e^{-Md/2}. \tag{3.55}$$

For $\gamma = 0$, we have $\Delta = 0$ and Eq. (3.54) reproduces Eq. (3.25) since $v_{x,0} = \tilde{v}_x$ for $Md \gg 1$; see Eq. (3.26). However, for $\gamma \neq 0$, the anisotropic Dirac cone is gapped and has the Chern number $C = -\frac{1}{2}\,\mathrm{sgn}(\Delta)$ [28,30,48–50].

We mention in passing that in terms of fermionic sublattice spinor fields, $\hat{\psi}_j(y) = \binom{\hat{\psi}_{Aj}(y)}{\hat{\psi}_{Bj}(y)}$, the low-energy Hamiltonian (3.49) can also be written as

$$H_{\text{eff}} = \sum_j \int dy \{\hat{\psi}_j^\dagger [-i\partial_y \tau_z + M g_0 \tau_x]\, \hat{\psi}_j + M g_1 [\hat{\psi}_j^\dagger \tau_+ \hat{\psi}_{j+1} + \text{H.c.}]\}, \tag{3.56}$$

with the approximations in Eq. (3.47) and using $\tau_+ = \frac{1}{2}(\tau_x + i\tau_y)$. Such a representation can be useful in order to include, for instance, Coulomb interaction effects.

The above projection scheme can be adapted to any periodic mass profile $M(x)$ alternating between positive and negative values. For a continuous mass profile, the zeros of $M(x)$ define the sites of the 1D bipartite lattice, and close to these zeros, a single (anti)kink in Eq. (3.36) can be approximated by a linear function $\mathcal{M}_K(x) = Mx/d$ [$\bar{\mathcal{M}}_K(x) = -Mx/d$]. In that case, the normalized zero-energy wave functions in Eq. (3.38) are replaced by

$$\phi_\pm(x) = (4\pi M/d)^{-1/4}\, e^{-\frac{M}{2d}x^2} \begin{pmatrix} 1 \\ \pm i \end{pmatrix}. \tag{3.57}$$

The effective low-energy Hamiltonian is then still given by Eq. (3.50), with $\tilde{f}(K)$ and $\tilde{g}(K)$ now calculated with $\phi_\pm$ in Eq. (3.57). We conclude that the projection approach offers a powerful route toward studying the low-energy theory of Dirac fermions in a mass superlattice.

IV. BOUNDARY MODES

We now turn to evanescent wave solutions which are characterized by a complex-valued quasimomentum K and can arise in the presence of boundaries or nonuniform potentials. Throughout this section, we focus on boundary-induced evanescent states in a constant potential and set $V(x) = 0$. In addition, we consider the low-energy regime (3.18), where κ in Eq. (2.6) is real-valued and $(Md)^2 + \xi > 0$ in Eq. (3.17). The length scale κ^{-1} governs the decay (or growth) of the wave function along the x direction in a region of constant mass. For the piecewise constant mass term (3.1), the length κ^{-1} thus represents a microscopic scale, which is only relevant on scales below the period d and which becomes shorter with increasing $|k_y|$. As discussed below, the mass superlattice generates another characteristic length scale, $\mathcal{K}^{-1}$, which governs the decrease (or increase) of evanescent waves on scales larger than the superlattice period d and which, for small $|k_y|$, grows with increasing $|k_y|$. In Sec. IV A, we summarize general properties of evanescent states, followed by the explicit calculation of boundary modes for a semi-infinite geometry in Sec. IV B.

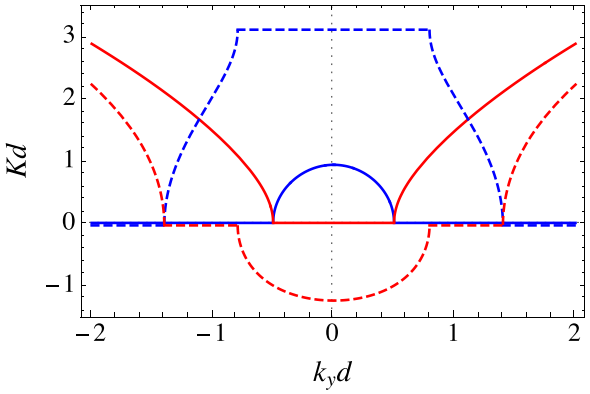

FIG. 5. Quasimomentum K in Eq. (4.1) vs k_y for $Md = 4$, taking the + sign in Eq. (4.1). Red (blue) curves show the imaginary (real) part of K. The solid curves are for $Ed = 0.5$ and the dashed curves for $Ed = 1.4$.

A. Evanescent states

The spectral condition (3.15) is formally solved by

$$Kd = \pm \arccos f(\xi), \tag{4.1}$$

with the function $f(\xi)$ in Eq. (3.17). Bloch wave solutions with real K only exist for $|f(\xi)| \leqslant 1$. For $f(\xi) > 1$, corresponding to $\xi > 0$ and thus to $|E| < |k_y|$, one instead finds a purely imaginary solution, $K = \pm i\mathcal{K}$ for the respective sign in Eq. (4.1), with the convention $\mathcal{K} > 0$. For $0 < \xi \ll 1$, we estimate

$$\mathcal{K}d \simeq \frac{\sinh(Md/2)}{Md/2}\sqrt{\xi}, \tag{4.2}$$

in agreement with Eqs. (3.25) and (3.26). The resulting type-I boundary modes, see Eq. (3.10), originate from states near the superlattice BZ center and are directly connected to the anisotropic Dirac cone dispersion (3.25). This case is illustrated for $Ed = 0.5$ (solid curves) in Fig. 5. For the wave function (3.3) of type-I states, using Eqs. (3.13) and (A6), we obtain

$$\frac{b_1(K = \pm i\mathcal{K})}{a_1} = \frac{e^{\mp \mathcal{K}d} - \Omega_{11}}{\Omega_{12}}, \tag{4.3}$$

resulting in a decay (increase) of $\psi_K(x)$ with increasing x for $K = i\mathcal{K}$ ($K = -i\mathcal{K}$). We note that the particle current along the x direction vanishes, $j_x = 0$, because b_1/a_1 is real.

Next we turn to the case $Ed = 1.4$ (dashed curves in Fig. 5), where the real part of K again vanishes for $|E| < |k_y|$, corresponding to type-I states. However, for small $|k_y|$ and $Md > 2$, a region with $f(\xi) < -1$ corresponding to $\xi < \xi_c < 0$ exists, cf. Fig. 2(a), where Eq. (4.1) yields a pair of type-II

states with $K = \mp i\mathcal{K} \pm \pi/d$, see Eq. (3.11). For $\xi \lesssim \xi_c$, we find

$$\mathcal{K}d \simeq \sqrt{f'(\xi_c)\,(\xi_c - \xi)}. \tag{4.4}$$

From Eq. (4.4) and Fig. 5, we observe that the decay length $\mathcal{K}^{-1}$ can exceed the lattice spacing d of the mass superlattice. The wave function of type-II states also follows from Eq. (3.3) but with

$$\frac{b_1(K = \mp i\mathcal{K} \pm \pi/d)}{a_1} = \frac{-e^{\pm \mathcal{K}d} - \Omega_{11}}{\Omega_{12}}, \tag{4.5}$$

again resulting in $j_x = 0$. The corresponding spatial probability density is illustrated in Fig. 3(b), where an overall decay on the emergent (long) length scale $\mathcal{K}^{-1}$ is clearly visible. At the same time, the microscopic length $\ell = d/2$ due to the mass superlattice causes a periodic modulation of the spatial decay.

The emergence of type-II states can also be seen from the results of Sec. III C. Near the boundary of the superlattice BZ, by writing $K = \frac{\pi}{d} + q$ with $|q|d \ll 1$, the low-energy dispersion relation (3.52) takes the form

$$E\left(\frac{\pi}{d} + q, k_y\right) \approx \pm\sqrt{-\tilde{v}_x^2 q^2 + k_y^2 + E_c^2}, \tag{4.6}$$

with $\tilde{v}_x$ in Eq. (3.55) and $E_c = 2\tilde{M}e^{-\frac{Md}{2}}\cosh(\frac{\gamma Md}{2})$. Equation (4.6) reveals a saddle point at the BZ boundary, which is responsible for the Lifshitz transition discussed in Sec. II A. For $|E| < E_c$, Bloch states with real q exist for any (small) value of k_y. However, for $|E| > E_c$, type-II states with imaginary q emerge for $k_y^2 < E^2 - E_c^2$.

B. Boundary modes for semi-infinite geometry

It is instructive to study a specific example admitting evanescent wave solutions. We here consider the Dirac mass superlattice problem on the half-plane $x < x_0$, with the boundary line $x = x_0$ located in a positive-mass region, say, $0 < x_0 < \frac{d}{2}$. We impose a boundary condition at $x = x_0$ and $y \in \mathbb{R}$,

$$\mathcal{B}(\alpha)\,\Psi(x_0, y) = \pm\Psi(x_0, y), \tag{4.7}$$

which ensures that the component of the current density normal to the boundary vanishes [51,52]. The matrix $\mathcal{B}$ depends on a phenomenological boundary angle α,

$$\mathcal{B}(\alpha) = \sigma_y \cos\alpha + \sigma_z \sin\alpha. \tag{4.8}$$

For definiteness, we choose the eigenvalue $+1$ in Eq. (4.7) in what follows. (The solution for eigenvalue -1 follows by replacing $\alpha \to \alpha + \pi$.) The corresponding eigenstate of $\mathcal{B}(\alpha)$ is given by

$$|\alpha\rangle = \begin{pmatrix} \cos\left(\frac{\alpha}{2} - \frac{\pi}{4}\right) \\ -i\sin\left(\frac{\alpha}{2} - \frac{\pi}{4}\right) \end{pmatrix}. \tag{4.9}$$

We now consider parameter regions with $|f(\xi)| > 1$, where Bloch waves are absent and K in Eq. (4.1) is complex-valued.

For the semi-infinite problem, normalizable states can be obtained only from one of the two solutions in Eq. (4.1). Denoting this solution by $K = K_0$ and recalling our convention $\mathcal{K} > 0$, we have $K_0 = -i\mathcal{K}$ for type-I states with $\xi > 0$. Similarly, we have $K_0 = -i\mathcal{K} + \pi/d$ for type-II states with $\xi < \xi_c < 0$. For $x \to -\infty$, the solution $\psi_{K_0}(x)$ decreases exponentially and therefore describes a normalizable state. The other solution $\psi_{-K_0}(x)$ grows exponentially for $x \to -\infty$ and hence is not admissible.

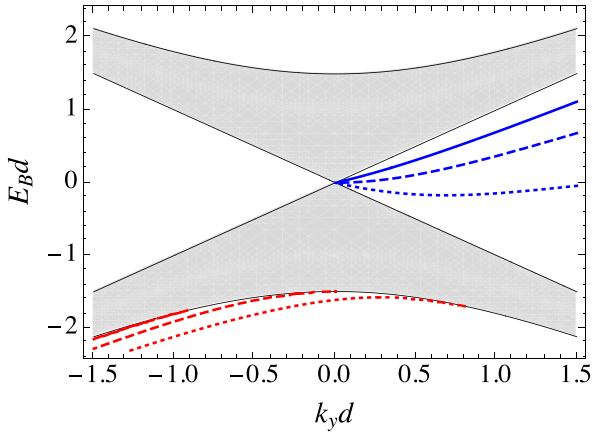

FIG. 6. Dispersion relation $E_B(k_y)$ of type-I (blue) and type-II (red) boundary modes in a semi-infinite geometry with $x < x_0$. We assume $x_0 = d/4$ and $Md = 3.1$, where results obtained by numerically solving Eq. (4.10) are shown for the boundary angles $\alpha = \pi/3, \pi/2$, and $2\pi/3$, using solid, dashed, and dotted lines, respectively. The shaded region corresponds to Bloch states.

The boundary condition (4.7) implies that the boundary spinor $\psi_{K_0}(x_0)$ must be proportional to the state $|\alpha\rangle$ in Eq. (4.9). Using Eq. (3.13), we thereby arrive at the spectral condition

$$(\Omega - e^{iK_0 d}\mathbb{1})W_M^{-1}(x_0)|\alpha\rangle = 0, \tag{4.10}$$

which determines the dispersion relation of the boundary modes $E = E_B(k_y)$. We illustrate typical results in Fig. 6 for different values of the boundary angle. For $Md > 2$, we observe both type-I boundary modes with $|E_B(k_y)| < |k_y|$ (blue curves) and type-II boundary modes (red curves). In both cases, the precise shape of the dispersion $E_B(k_y)$ sensitively depends on the angle α and on the boundary location x_0 (not shown). Moreover, the dispersion is not symmetric in k_y, which implies that the boundary modes can carry unidirectional currents. We therefore expect them to be observable in transport experiments. In addition, they could be detected in STM experiments.

V. POTENTIAL STEP AND INTERFACE MODES

In this section, we return to the extended problem (without boundaries) for the Dirac Hamiltonian (2.1) with the periodic mass term in Eq. (3.1). We now include an electrostatic potential step of moderate step size $2V_s$ at position $x = x_s$,

$$V(x) = V_s\,\mathrm{sgn}(x - x_s), \quad 0 < 2V_s < M. \tag{5.1}$$

The potential (5.1) defines an np junction. For definiteness, we assume $0 < x_s < \frac{d}{2}$ such that the step is located in a region of positive mass.

Here we focus on the most interesting low-energy regime with real-valued κ parameters in Eq. (2.6). Recalling that a

uniform potential can be accounted for by shifting the energy E, on the left side $x < x_s$, $\kappa = \kappa_L$ follows from Eq. (2.6) with $E \to E + V_s$. Similarly, $\kappa = \kappa_R$ for $x > x_s$ is obtained by replacing $E \to E - V_s$. [Below we will also use $\xi_{L,R}$ which follows from Eq. (3.16) with the same substitutions.] In order to have both κ_L and κ_R real for all values of k_y, we require

$$|E| < M - V_s. \tag{5.2}$$

Apart from evanescent states bound to the potential step, we then have to take into account only the zero-mode band with $n = 0$ corresponding to the emergent anisotropic Dirac cone near the Γ point.

In Sec. V A, we consider scattering states and calculate the corresponding transmission probability for the potential step (5.1). The linear two-terminal conductance G is discussed in Sec. V B, where we consider transport across the junction with lead electrodes attached to the system at $x \to \pm\infty$. Interestingly, we find a pronounced dependence of G on the step position x_s. In Sec. V C, we then determine the dispersion relation of interface modes, which are spatially localized near the potential step in the x direction but propagate along the y direction.

A. Scattering states and transmission probability

We here consider scattering states with energy

$$|E| < V_s. \tag{5.3}$$

Since the emergent Dirac cones on the two sides of the junction are shifted by the potential in opposite directions, in this energy window one finds a particle-like state on the left side and a hole-like state on the right side of the np junction. The associated group velocity is then parallel (antiparallel) to the momentum K on the left (right) side. We note that for $0 < 2V_s < M$, Eq. (5.3) automatically implies Eq. (5.2). For given E and k_y, we have a pair of 1D Fermi momenta $\pm K_L$ on the left side, and similarly $\pm K_R$ on the right side. The values of $K_L > 0$ and $K_R > 0$ follow from the spectral equation (3.15). In particular, using the auxiliary function $\Phi(E, K, k_y)$ in Eq. (3.20), $K_{L,R}$ are the solutions of

$$\Phi(E + V_s, K_L, k_y) = 0, \quad \Phi(E - V_s, K_R, k_y) = 0. \tag{5.4}$$

We then use Eqs. (3.3) and (3.31) to determine the scattering state by matching the wave function on the left side of the junction to the wave function on the right side. Appending energy arguments as indices on the matrix $W_M(x)$ in Eq. (2.5), the full wave function for $0 < x < \frac{d}{2}$ is written as

$$\begin{aligned}\psi(x < x_s) &= W_{E+V_s,M}(x)\left[\begin{pmatrix}a_1\\ b_1\end{pmatrix}_{K_L} + r\begin{pmatrix}a_1\\ b_1\end{pmatrix}_{-K_L}\right],\\ \psi(x > x_s) &= t\, W_{E-V_s,M}(x)\begin{pmatrix}a_1\\ b_1\end{pmatrix}_{-K_R},\end{aligned} \tag{5.5}$$

with complex-valued reflection (r) and transmission (t) amplitudes. We normalize the incident, reflected, and transmitted wave functions such that they carry unit current; see Eq. (3.34). Notice that the wave function for $x > x_s$ describes a hole propagating to the right and therefore involves the 1D Fermi momentum $-K_R$.

The transmission probability $\mathcal{T}$ is given by

$$\mathcal{T}(E, k_y) = |t|^2 = \left|\frac{a_1(K_L)}{a_1(K_R)}\right|^2 |t'|^2, \tag{5.6}$$

where the amplitude t' follows by setting all coefficients $a_1(\pm K_{L,R}) = 1$ in Eq. (5.5). Continuity of $\psi(x)$ at $x = x_s$ then results in two coupled linear equations for r and t',

$$\begin{aligned}&W_{E+V_s,M}(x_s)\left[\begin{pmatrix}1\\ b_1\end{pmatrix}_{K_L} + r\begin{pmatrix}1\\ b_1\end{pmatrix}_{-K_L}\right]\\ &\quad = t'\, W_{E-V_s,M}(x_s)\begin{pmatrix}1\\ b_1\end{pmatrix}_{-K_R},\end{aligned} \tag{5.7}$$

where, using $a_1 = 1$, Eq. (3.31) gives

$$b_1(\pm K_L) = \frac{e^{\pm iK_L d} - \Omega_{11}(E + V_s)}{\Omega_{12}(E + V_s)}, \tag{5.8}$$

and analogously for $b_1(\pm K_R)$. Note that the energy argument of the Ω matrix elements (A6) has been made explicit. With the auxiliary quantities

$$\begin{pmatrix}A(K)\\ B(K)\end{pmatrix} = W^{-1}_{E+V_s,M}(x_s)\, W_{E-V_s,M}(x_s)\begin{pmatrix}1\\ b_1(K)\end{pmatrix}, \tag{5.9}$$

where we suppress the dependence on x_s, reflection and transmission amplitudes can be expressed as

$$\begin{aligned}r &= -\frac{B(-K_R) - b_1(K_L)A(-K_R)}{B(-K_R) - b_1(-K_L)A(-K_R)},\\ t' &= \frac{b_1(K_L) - b_1(-K_L)}{B(-K_R) - b_1(-K_L)A(-K_R)}.\end{aligned} \tag{5.10}$$

We thus obtain the reflection probability $\mathcal{R} = |r|^2$ and the transmission probability $\mathcal{T}$ from Eq. (5.6). Of course, current conservation yields $\mathcal{T} = 1 - \mathcal{R}$.

We illustrate typical results for the transmission probability in Fig. 7. Depending on the parameters, Bloch states, and thus a finite transmission, can only be realized in a window of k_y values. For fixed step position, we indeed observe a strong dependence on k_y, with the symmetry $\mathcal{T}(E = 0, -k_y) = \mathcal{T}(E = 0, k_y)$, cf. Fig. 7(a), where we also illustrate the effect of changing the parameter Md. In particular, we see that at fixed energy, for the case of larger mass in the main panel of Fig. 7(a), there is a window around $k_y = 0$ where the transmission vanishes. This window shrinks as the mass decreases, and eventually closes, as shown in the inset. Notice that the window's edges do not depend on the position of the step. For fixed (E, k_y), Fig. 7(b) reveals a pronounced dependence of $\mathcal{T}$ on the step position x_s, with the symmetry $\mathcal{T}(\frac{d}{2} - x_s, k_y) = \mathcal{T}(x_s, -k_y)$. This effect is linked to the strong x dependence of the wave functions. Indeed, as discussed in Sec. III C, the low-energy states are built from chiral zero modes which are localized along the x direction near $x = jd/2$ (integer j). Depending on the sign of k_y, we find high transmission probability if x_s is near one of these positions, where the probability density has maxima; see Fig. 3(a). In the next section, we study how this behavior affects the electrical conductance.

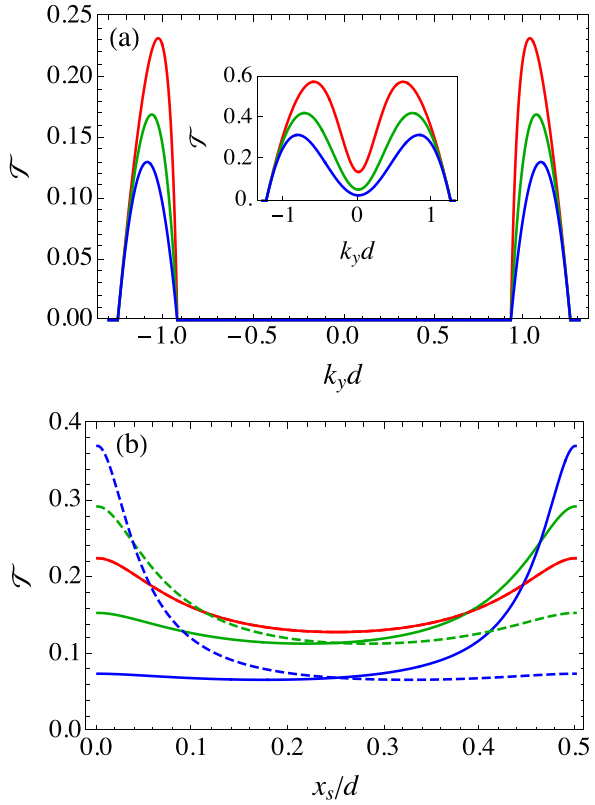

FIG. 7. Transmission probability $\mathcal{T}$ for the Dirac mass superlattice in the presence of the potential step (5.1) with $V_s d = 1.25$. (a) $\mathcal{T}$ vs k_y for $E = 0$, $Md = 5$, and $x_s/d = 0.05, 0.1, 0.25$ (red, green, blue curves). Inset: Same parameters as in the main panel but for $Md = 3.7$. (b) $\mathcal{T}$ vs step position x_s for $Md = 5$ with $k_y d = 1.1$ (solid lines) and $k_y d = -1.1$ (dashed lines), using $Ed = 0, 0.05, 0.1$ (red, green, blue curves).

B. Conductance

Within a noninteracting theory, the transmission probability $\mathcal{T}(E, k_y)$ directly determines the linear two-terminal conductance G via the standard Landauer-Büttiker formula [53]. At zero temperature, identifying E with the Fermi energy E_F, the conductance for a strip of large width W along the y direction, with source and drain electrodes adiabatically connected at $x \to \pm\infty$, is given by

$$G = \frac{N_v e^2 W}{(2\pi)^2 \hbar} \int dk_y \, \mathcal{T}(E_F, k_y), \tag{5.11}$$

where N_v is a degeneracy factor. For instance, in a graphene monolayer, we have $N_v = 4$ because of spin and valley degeneracies. Note that at given energy, only states with k_y such that $|f(\xi_{L,R})| < 1$ have finite transmission probability and contribute to the conductance.

We illustrate the dependence of G on the potential step position x_s and on the step size V_s in Fig. 8. We observe that G strongly depends on x_s and, in the interval $0 < x_s < d/2$, exhibits a broad minimum at $x_s = d/4$ with the symmetry $G(\frac{d}{2} - x_s) = G(x_s)$. The conductance will then be a periodic

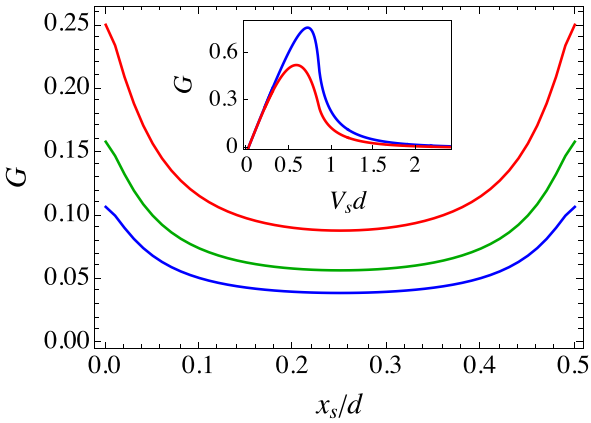

FIG. 8. Conductance G for the Dirac mass superlattice with $Md = 5$ at Fermi energy $E_F = 0$ in the presence of the potential step (5.1). We show G in units of $\frac{N_v e^2 W}{(2\pi)^2 \hbar d}$ for a strip of width W and degeneracy index N_v. Main panel: G vs step position x_s for several values of the potential step size, $V_s d = 1.1, 1.25, 1.4$, shown by red, green, and blue curves, respectively. Inset: G vs V_s for $x_s = 0.05d$ (blue) and $x_s = 0.25d$ (red curve).

function of x_s with period $d/2$. Such conductance oscillations are most pronounced for $Md \gg 1$ and small values of the Fermi energy, where the relevant electronic states originate from the chiral zero modes localized near the mass (anti)kinks at $x = jd/2$. The x_s dependence of G becomes weaker for smaller values of M (results not shown). A pronounced spatial dependence of G on the step position is therefore a hallmark of the existence of zero modes which are well localized along the x direction.

As a function of step size V_s, we observe that the conductance shows a broad peak; cf. inset of Fig. 8. This behavior can be rationalized by noting that in this example we consider $E_F = 0$, where the density of states associated with the Dirac cone, and hence also the conductance, vanishes for $V_s \to 0$. Moreover, upon increasing V_s, the phase space for transmission (the window of k_y where the transmission amplitude is finite) first increases, but eventually shrinks and, as a consequence, the conductance decreases toward zero.

C. Interface states

We finally study states localized near the interface at $x = x_s$. These states are formed by a combination of either type-I or type-II evanescent waves on opposite sides of the step, matched at $x = x_s$. In particular, solutions with type-II modes on both sides ("type II-II" interface modes) require $f(\xi_L) < -1$ and $f(\xi_R) < -1$, and have quasimomenta

$$K_L = -i\mathcal{K}_L + \frac{\pi}{d}, \quad K_R = +i\mathcal{K}_R - \frac{\pi}{d}, \tag{5.12}$$

with $\mathcal{K}_{L,R} > 0$ given by Eq. (4.4) with the replacement $E \to E \pm V_s$. The state $\psi_{K_L}(x)$ (for $x < x_s$) then shows an exponential decay for $x \to -\infty$ and, similarly, $\psi_{K_R}(x)$ (for $x > x_s$) decays for $x \to \infty$. For type I-II interface states, composed of type-I and type-II modes on opposite sides, we find that, for $E > 0$, the type-II state is on the left and type-I on the right

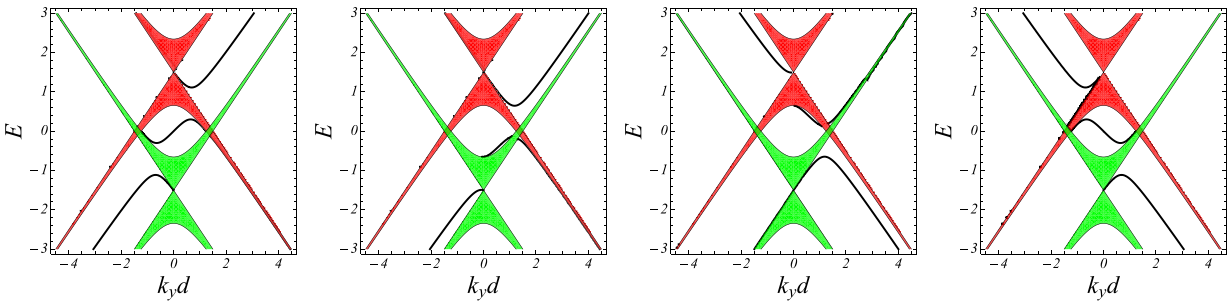

FIG. 9. Dispersion relation of interface states bound to a potential step with $V_s d = 1.5$ and several step positions x_s for $Md = 5$, with E in units of $\hbar v_F/d$. The green (red) bands correspond to Bloch states at $x < x_s$ ($x > x_s$). The solid black curves refer to interface modes. The interface modes in the central inner region are of type II-II, while all others are of type I-II. From left to right panel: $x_s = 0$, $x_s = 0.1d$, $x_s = 0.4d$, and $x_s = 0.5d$.

side, with

$$K_L = -i\mathcal{K}_L + \frac{\pi}{d}, \quad K_R = +i\mathcal{K}_R, \tag{5.13}$$

while for $E < 0$, the opposite happens, with

$$K_L = -i\mathcal{K}_L, \quad K_R = +i\mathcal{K}_R - \frac{\pi}{d}. \tag{5.14}$$

The wave function matching condition at $x = x_s$ now implies

$$W_{E+V_s,M}(x_s)\begin{pmatrix} a_1 \\ b_1 \end{pmatrix}_{K_L} = t'\, W_{E-V_s,M}(x_s)\begin{pmatrix} a_1 \\ b_1 \end{pmatrix}_{K_R}, \tag{5.15}$$

with $b_1(K)$ in Eq. (5.8). Using the auxiliary quantities in Eq. (5.9), we arrive at the equation

$$(\Omega(E + V_s) - e^{iK_L d}\mathbb{1})\begin{pmatrix} A(K_R) \\ B(K_R) \end{pmatrix} = 0, \tag{5.16}$$

which implicitly defines the dispersion relation $E = E_I(k_y)$ of the interface modes. As for the boundary case (4.10), the two equations in Eq. (5.16) are nonlinear conditions for k_y and E which have to be solved simultaneously. Depending on the parameter values, our numerical analysis shows that such solutions indeed exist. Typical results for the dispersion relation $E_I(k_y)$ are shown in Fig. 9. We find interface modes of type I-II or type II-II, where the latter modes can only exist for $Md > 2$. For the parameters in Fig. 9, there are no type I-I interface modes. In fact, the absence of type I-I modes is a generic feature which can be rationalized by observing that their dispersion should originate from one of the two crossing points ($k_y = 0, E = \pm V_s$), but at the same time it should satisfy the conditions $k_y^2 > (E_I \pm V_s)^2$. Clearly, both requirements are incompatible.

In analogy to the boundary modes in Sec. IV, we expect such interface modes to affect transport properties. In addition, they should be observable by STM or tunneling spectroscopy.

VI. CONCLUSIONS

Our analysis of 2D Dirac fermions in a piecewise constant mass superlattice, where the mass term periodically changes sign, shows a remarkable richness. We have shown that the low-energy part of the spectrum is spanned by the chiral zero modes tied to the zero-mass lines of the superlattice. Apart from the resulting anisotropic Dirac cone dispersion, we also predict nontrivial boundary modes as well as interface modes near potential steps. Those modes exist in two different types. Type-I modes require a momentum $|k_y|$ parallel to the zero-mass lines which is larger than the energy $|E|$. Instead, type-II modes emerge at small $|k_y|$ but exist only for $Md > 2$, where M is the amplitude of the mass term and d the superlattice period. Both types of evanescent states could affect transport properties and should be observable by STM techniques.

Although our results have been derived for a particular exactly solvable model, we have also shown that in the regime $Md \gg 1$, the low-energy physics is directly connected to the chiral zero modes localized at the zero-mass lines, and therefore is generic to all Dirac mass superlattices where the mass alternates between positive and negative values, including periodic arrays of topological junctions between Chern insulators with different Chern numbers.

The low-energy theory put forward in this work points to several interesting extensions. First, the inclusion of an orbital magnetic field along the z direction allows one to study the interplay of Landau level formation and quantum Hall physics with the phenomena discussed above. Second, since we have a model of coupled 1D chiral fermions, bosonization methods [54] can be used to construct solvable nonperturbative theories of this 2D system in the presence of electron-electron interactions.

Zero-line modes similar to those discussed in our work have also been reported in recent experiments performed on magnetic topological insulators [55] which realize interfaces between quantum anomalous Hall insulators [23] with different Chern numbers. We expect that our results will also be relevant in this platform. Theoretical predictions for layer-dependent zero-line modes in antiferromagnetic topological insulator multilayer structures based on $MnBi_2Te_4$ [56] suggest that our theory can also be applied in that context. An important caveat when comparing our results to experiments concerns the idealized steplike mass term considered here. While this simplification allowed us to obtain exact analytical solutions, for smooth mass kinks, additional states localized at the kinks can emerge at elevated energies, so-called Volkov-Pankratov states [37,39,40]. However, such states are nonchiral and are expected to cause distinct transport and

spectroscopical features compared to the chiral states discussed in our work.

To conclude, we hope that the results put forward here will inspire future experimental and theoretical work along these lines.

ACKNOWLEDGMENTS

We thank Dario Bercioux and Alex Zazunov for valuable discussions. An extended stay of A. Miserocchi at HHU Düsseldorf has been funded by the Erasmus+ for Traineeships program and by the University of Padova. We acknowledge funding by the Deutsche Forschungsgemeinschaft (DFG; German Research Foundation), Projekt nummer 277101999–TRR 183 (Project No. B04), Normalverfahren Projektnummer EG 96-13/1, and under Germany's Excellence Strategy–Cluster of Excellence Matter and Light for Quantum Computing (ML4Q) EXC 2004/1–390534769.

APPENDIX: MATRIX PROPERTIES

We here summarize useful algebraic relations involving the matrix $W_M(x)$ in Eq. (2.5). We first note that its inverse is given by

$$W_M^{-1}(x) = \frac{1}{2\kappa}\begin{pmatrix} (k_y+\kappa)e^{-\kappa x} & i(M+E)e^{-\kappa x} \\ -(k_y-\kappa)e^{\kappa x} & -i(M+E)e^{\kappa x}\end{pmatrix} \tag{A1}$$

with κ in Eq. (2.6). Second, we observe that the determinant of $W_M(x)$ is x-independent, $\det W_M(x) = \frac{2i\kappa}{M+E}$. Third, Eqs. (2.5) and (A1) imply the relation

$$W_{-M}^{-1}(x)\, W_M(x) = \frac{1}{\kappa(E+M)}\begin{pmatrix} E\kappa + Mk_y & e^{-2\kappa x}(\kappa+k_y)M \\ e^{2\kappa x}(\kappa-k_y)M & E\kappa - Mk_y\end{pmatrix}. \tag{A2}$$

Fourth, for real κ corresponding to $E^2 < k_y^2 + M^2$, we find

$$W_M^\dagger(x)\, W_M(x) = \begin{pmatrix} e^{2\kappa x}\left[1+\left(\frac{k_y-\kappa}{E+M}\right)^2\right] & \frac{2E}{E+M} \\ \frac{2E}{E+M} & e^{-2\kappa x}\left[1+\left(\frac{k_y+\kappa}{E+M}\right)^2\right]\end{pmatrix}, \tag{A3}$$

$$W_M^\dagger(x)\,\sigma_x\, W_M(x) = -\frac{2\kappa}{E+M}\sigma_y, \quad W_M^\dagger(x)\,\sigma_y\, W_M(x) = \frac{2}{E+M}\begin{pmatrix} e^{2\kappa x}(k_y-\kappa) & k_y \\ k_y & e^{-2\kappa x}(k_y+\kappa)\end{pmatrix}.$$

For $\kappa = ik$ with real $k > 0$, we instead find

$$W_M^\dagger(x)\, W_M(x) = \begin{pmatrix} \frac{2E}{E+M} & e^{-2ikx}\left[1-\left(\frac{-k+ik_y}{E+M}\right)^2\right] \\ e^{2ikx}\left[1-\left(\frac{k+ik_y}{E+M}\right)^2\right] & \frac{2E}{E+M}\end{pmatrix}, \tag{A4}$$

$$W_M^\dagger(x)\,\sigma_x\, W_M(x) = \frac{2k}{E+M}\sigma_z, \quad W_M^\dagger(x)\,\sigma_y\, W_M(x) = \frac{2}{E+M}\begin{pmatrix} k_y & e^{-2ikx}(k_y+ik), \\ e^{2ikx}(k_y-ik) & k_y\end{pmatrix}.$$

Next, the matrix Ω_B in Eq. (2.13) for the mass-barrier problem in Sec. II C is given by

$$\Omega_B = \frac{1}{\kappa^2(E^2-M^2)}\begin{pmatrix} (E^2-M^2)(k_y^2-E^2+M^2e^{-2\kappa\ell}) & -2M(\kappa+k_y)(E\kappa+k_yM)\sinh(\kappa\ell) \\ 2M(\kappa-k_y)(E\kappa-k_yM)\sinh(\kappa\ell) & (E^2-M^2)(k_y^2-E^2+M^2e^{2\ell\kappa})\end{pmatrix}. \tag{A5}$$

Similarly, the modified transfer matrix Ω in Eq. (3.7) for the periodic mass profile (3.1) reads

$$\Omega = \frac{1}{\kappa^2(E^2-M^2)}\begin{pmatrix} (E^2-M^2)[M^2+(k_y^2-E^2)e^{\kappa d}] & M(1-e^{-\kappa d})(\kappa+k_y)(E\kappa-Mk_y) \\ M(1-e^{\kappa d})(\kappa-k_y)(E\kappa+Mk_y) & (E^2-M^2)[M^2+(k_y^2-E^2)e^{-\kappa d}]\end{pmatrix}. \tag{A6}$$

For $E^2 < k_y^2 + M^2$ such that κ is real, the matrix elements of Ω are also real. For completeness, we also specify the elements of the symmetric transfer matrix T:

$$\begin{aligned} T_{11} &= \frac{M^2+(k_y^2-E^2)\cosh(\kappa d)}{\kappa^2} + \frac{ME[\cosh(\kappa d)-1]+k_y\kappa\sinh(\kappa d)}{\kappa^2}, \\ T_{12} = T_{21} &= i\,\frac{E\kappa\sinh(\kappa d)+Mk_y[\cosh(\kappa d)-1]}{\kappa^2}, \\ T_{22} &= \frac{M^2+(k_y^2-E^2)\cosh(\kappa d)}{\kappa^2} - \frac{ME[\cosh(\kappa d)-1]+k_y\kappa\sinh(\kappa d)}{\kappa^2}. \end{aligned} \tag{A7}$$

[1] C.-H. Park, L. Yang, Y.-W. Son, M. L. Cohen, and S. G. Louie, Nat. Phys. **4**, 213 (2008).
[2] C.-H. Park, Y.-W. Son, L. Yang, M. L. Cohen, and S. G. Louie, Nano Lett. **8**, 2920 (2008).
[3] A. Isacsson, L. M. Jonsson, J. M. Kinaret, and M. Jonson, Phys. Rev. B **77**, 035423 (2008).
[4] M. Barbier, P. Vasilopoulos, and F. M. Peeters, Philos. Trans. R. Soc. A **368**, 5499 (2010).

[5] L. A. Ponomarenko, R. V. Gorbachev, G. L. Yu, D. C. Elias, R. Jalil, A. A. Patel, A. Mishchenko, A. S. Mayorov, C. R. Woods, J. R. Wallbank, M. Mucha-Kruczynski, B. A. Piot, M. Potemski, I. V. Grigorieva, K. S. Novoselov, F. Guinea, V. I. Fal'ko, and A. K. Geim, Nature (London) **497**, 594 (2013).

[6] C. Forsythe, X. Zhou, K. Watanabe, T. Taniguchi, A. Pasupathy, P. Moon, M. Koshino, P. Kim, and C. R. Dean, Nat. Nanotechnol. **13**, 566 (2018).

[7] Y. Li, S. Dietrich, C. Forsythe, T. Taniguchi, K. Watanabe, P. Moon, and C. R. Dean, Nat. Nanotechnol. **16**, 525 (2021).

[8] Z. Li, T. Cao, M. Wu, and S. G. Louie, Nano Lett. **17**, 2280 (2017).

[9] P. J. Ledwith, E. Khalaf, and A. Vishwanath, Ann. Phys. **435**, 168646 (2021).

[10] T. Ideue and Y. Iwasa, Annu. Rev. Condens. Matter Phys. **12**, 201 (2021).

[11] J. Cano, S. Fang, J. H. Pixley, and J. H. Wilson, Phys. Rev. B **103**, 155157 (2021).

[12] E. Y. Andrei and A. H. MacDonald, Nat. Mater. **19**, 1265 (2020).

[13] L. Dell'Anna and A. De Martino, Phys. Rev. B **79**, 045420 (2009).

[14] L. Z. Tan, C.-H. Park, and S. G. Louie, Phys. Rev. B **81**, 195426 (2010).

[15] L. Dell'Anna and A. De Martino, Phys. Rev. B **83**, 155449 (2011).

[16] L. Lenz and D. Bercioux, Europhys. Lett. **96**, 27006 (2011).

[17] A. H. Castro Neto, F. Guinea, N. M. R. Peres, K. S. Novoselov, and A. K. Geim, Rev. Mod. Phys. **81**, 109 (2009).

[18] M. Z. Hasan and C. L. Kane, Rev. Mod. Phys. **82**, 3045 (2010).

[19] S.-Q. Shen, *Topological Insulators: Dirac Equation in Condensed Matter*, 2nd ed. (Springer, 2017).

[20] R. Jackiw and C. Rebbi, Phys. Rev. D **13**, 3398 (1976).

[21] R. Jackiw and J. Schrieffer, Nucl. Phys. B **190**, 253 (1981).

[22] G. W. Semenoff, V. Semenoff, and F. Zhou, Phys. Rev. Lett. **101**, 087204 (2008).

[23] C.-Z. Chang, C.-X. Liu, and A. H. MacDonald, Rev. Mod. Phys. **95**, 011002 (2023).

[24] K. Yasuda, M. Mogi, R. Yoshimi, A. Tsukazaki, K. S. Takahashi, M. Kawasaki, F. Kagawa, and Y. Tokura, Science **358**, 1311 (2017).

[25] I. T. Rosen, E. J. Fox, X. Kou, L. Pan, K. L. Wang, and D. Goldhaber-Gordon, npj Quantum Mater. **2**, 69 (2017).

[26] I. Martin, Y. M. Blanter, and A. F. Morpurgo, Phys. Rev. Lett. **100**, 036804 (2008).

[27] Z. Qiao, J. Jung, C. Lin, Y. Ren, A. H. MacDonald, and Q. Niu, Phys. Rev. Lett. **112**, 206601 (2014).

[28] W. Yao, S. A. Yang, and Q. Niu, Phys. Rev. Lett. **102**, 096801 (2009).

[29] X. Bi, J. Jung, and Z. Qiao, Phys. Rev. B **92**, 235421 (2015).

[30] Z. Wang, S. Cheng, X. Liu, and H. Jiang, Nanotechnology **32**, 402001 (2021).

[31] L. Yin, H. Jiang, J. Qiao, and L. He, Nat. Commun. **7**, 11760 (2016).

[32] P. San-Jose and E. Prada, Phys. Rev. B **88**, 121408(R) (2013).

[33] Y. Ran, Y. Zhang, and A. Vishwanath, Nat. Phys. **5**, 298 (2009).

[34] J. C. Y. Teo and C. L. Kane, Phys. Rev. B **82**, 115120 (2010).

[35] Y.-F. Zhou, Z. Hou, and Q.-F. Sun, Phys. Rev. B **98**, 165433 (2018).

[36] C. Xiao, J. Tang, P. Zhao, Q. Tong, and W. Yao, Phys. Rev. B **102**, 125409 (2020).

[37] M. Zarenia, O. Leenaerts, B. Partoens, and F. M. Peeters, Phys. Rev. B **86**, 085451 (2012).

[38] G. M. Maksimova, E. S. Azarova, A. V. Telezhnikov, and V. A. Burdov, Phys. Rev. B **86**, 205422 (2012).

[39] S. Tchoumakov, V. Jouffrey, A. Inhofer, E. Bocquillon, B. Plaçais, D. Carpentier, and M. O. Goerbig, Phys. Rev. B **96**, 201302(R) (2017).

[40] T. L. van den Berg, A. De Martino, M. R. Calvo, and D. Bercioux, Phys. Rev. Res. **2**, 023373 (2020).

[41] J. Briones-Torres, J. Madrigal-Melchor, J. Martínez-Orozco, and I. Rodríguez-Vargas, Superlattices Microstruct. **73**, 98 (2014).

[42] A. Vishwanath and D. Carpentier, Phys. Rev. Lett. **86**, 676 (2001).

[43] C. L. Kane, R. Mukhopadhyay, and T. C. Lubensky, Phys. Rev. Lett. **88**, 036401 (2002).

[44] Y. Han, S. You, and Z. Qiao, Phys. Rev. B **105**, 155301 (2022).

[45] I. M. Lifshitz, Sov. Phys. JETP **11**, 1130 (1960).

[46] A. M. Eldib, H. F. Hassan, and M. A. Mohamed, J. Phys. C: Solid State Phys. **20**, 3011 (1987).

[47] T. B. Smith and A. Principi, J. Phys.: Condens. Matter **32**, 055502 (2020).

[48] J. Alicea, Rep. Prog. Phys. **75**, 076501 (2012).

[49] S. M. Girvin and K. Yang, *Modern Condensed Matter Physics* (Cambridge University Press, 2019).

[50] D. Xiao, M.-C. Chang, and Q. Niu, Rev. Mod. Phys. **82**, 1959 (2010).

[51] E. Witten, Riv. Nuovo Cimento **39**, 313 (2016).

[52] F. Buccheri, A. De Martino, R. G. Pereira, P. W. Brouwer, and R. Egger, Phys. Rev. B **105**, 085410 (2022).

[53] S. Datta, *Electronic Transport in Mesoscopic Systems* (Cambridge University Press, 1995).

[54] A. O. Gogolin, A. A. Nersesyan, and A. M. Tsvelik, *Bosonization and Strongly Correlated Systems* (Cambridge University Press, 1998).

[55] Y. F. Zhao, R. Zhang, J. Cai, D. Zhuo, L. J. Zhou, Z. J. Yan, M. H. W. Chan, X. Xu, and C. Z. Chang, Nat. Commun. **14**, 770 (2023).

[56] W. Liang, T. Hou, J. Zeng, Z. Liu, Y. Han, and Z. Qiao, Phys. Rev. B **107**, 075303 (2023).